Exposing the Injection Machinery Dynamics of Bacteriophage T4 through Multi-Scale Modeling

By

Ameneh Maghsoodi

A dissertation submitted in partial fulfillment
of the requirements for the degree of
Doctor of Philosophy
(Mechanical Engineering)
in the University of Michigan
2019

Doctoral Committee:

Professor Noel C. Perkins, Chair
Professor Charles L. Brooks III
Associate Professor Petr G. Leiman, University of Texas Medical Branch
Professor Kon-Well Wang

Ameneh Maghsoodi

maghsudi@umich.edu

ORCID iD: 0000-0002-8250-8734

Dedication

To my parents and my spouse,
for their unconditional love and support.

Acknowledgements

I have been extremely fortunate to be able to study at the University of Michigan. I would like to express my heartfelt gratitude to all the people who provided me with support, guidance, and encouragement.

First and foremost, I would like to express my sincere gratitude to my advisor Prof. Noel Perkins for his highly motivating research guidance. I thank you for being encouraging and inspiring during our meetings, and providing me the opportunity to explore different subjects during my Ph.D. Thank you for making me feel welcome all these years. This research would not have been possible without your continuing support and encouragement.

I would also like to thank my doctoral committee, Prof. Kon-Well Wang, Prof. Charles L. Brooks III, and Prof. Petr G. Leiman, for their insightful comments and advice which made this dissertation possible, and for their continued support to my study and career. I am also thankful to Prof. Allen Liu who served as the committee member of my pre-candidacy doctoral exam and continuously supported me in academic career.

I would like to thank Prof. Ioan Andricioaei at the University of California-Irvine, and his Ph.D. student, Anupam Chatterjee, for collaborations and providing MD simulations data in Chapters 3 and 5.

I am also grateful to my friends in Perkins Research Group, particularly, Rachel Vitali and Michael Potter, for being encouraging during these years. I am also thankful to all my friends in Ann Arbor for being supportive. Without them, I would not have been able to enjoy my life here in Ann Arbor throughout many winters and summers.

I am forever thankful to my amazing family for their unconditional love and support, and instilling in me a passion for learning and pursuing my goals. I would like to thank my husband, Amin, for his love, encouragement, and positive thoughts.

Finally, I am grateful for the financial support I received from the University of Michigan Department of Mechanical Engineering that supported me with one semester Department Fellowship and one semester Graduate Student Instructorship. I also gratefully acknowledge the continuous financial support from NSF grant No. CMMI-1404747.

Table of Contents

List of Tables

List of Figures

List of Appendices

Abstract

Bacteriophage T4 is one of the most well studied contractile-tailed viruses from the family *Myoviridae* which infects the bacterium *Escherichia coli* using an intriguing contractile tail assembly. The phage T4 is composed of three major structures: 1) a large capsid containing the viral genome (DNA), 2) a contractile tail structure that generates the driving force to pierce the host membrane and transfer DNA from the capsid into the host, and 3) a baseplate equipped with fibers that recognize and bind to the host. The contractile tail consists of a needle-like tail tube surrounded by an elastic sheath. During injection, the sheath undergoes a large conformational transition from a high-energy (extended) state to a low-energy (contracted) state, thereby releasing the energy needed for the tail tube to penetrate the host. Bacteriophages are employed as an alternative to antibiotics to treat infectious diseases and, importantly, those now growing resistant to antibiotics. In addition, because phages T4 are highly efficient genome delivery machines, understanding their function has major implications for future bio-nanotechnology devices. Thus, there is ample motivation for extending engineering methods to reveal the basic science underlying phage function.

Despite extensive progress in resolving the structure of T4, the dynamics of the

injection machinery remains largely unknown. This dissertation contributes the first system-level model describing the nonlinear dynamics of the phage T4 injection machinery interacting with a host cell. We employ a three-dimensional continuum dynamic model (based on Kirchhoff rod theory) to simulate the nonlinear dynamics of the six protein strands that constitute the sheath coupled to a model for the remainder of the virus interacting with host cell. The resulting continuum model for the contractile sheath employs elastic constants determined *a priori* from molecular dynamics simulations.

The resulting system-level model captures virus-cell interactions as well as competing energetic mechanisms that release and dissipate energy during the injection process. The sources of energy dissipation include the hydrodynamic dissipation on the capsid and sheath from the surrounding environment, the internal dissipation of the sheath strands, the dissipation from the host cell membrane interacting with the tip of the tail tube, and the hydrodynamic interaction between the sheath and the tail tube. The new findings and major conclusions drawn from this system model are as follows.

The model estimates that the injection process is driven by approximately 14500 kT of elastic energy stored in the extended sheath which is consistent with the reported enthalpic change reported in the experimental literature. The model also reveals that the dynamical pathway of the injection progresses as a "contraction wave" that propagates along the sheath, a finding consistent with published micrographs observed in experiments. The model further estimates that cell rupture arises when the tip of the tail tube exerts a force of ~330 pN and at a membrane indentation of ~60 Å. Finally, the model enables broad exploration of the four energy dissipation mechanisms and reveals the mechanisms and parameters that control the time scale of the injection process.

Chapter 1

Introduction

1.1 Background on bacteriophages

Bacteriophages, or "phages" for short, are viruses that inject their genome in a bacterial host during infection in order to replicate their DNA within the host. A large variety of phages exist, with each adapted to infect only a single or limited number of bacterial cells [1]. The vast majority (96%) of phages possess a large icosahedral protein capsid that contains its genome and a tail structure that is used to deliver the genome during infection [2]. As illustrated in Figure 1.1, the tailed phages subdivide into three families that are distinguished by their tail structure. The three families include the family *Myoviridae* (e.g., T4, φ92, φKZ) which possess elaborate tails that mechanically contract during infection; the family *Siphoviridae* (e.g., λ, HK97, SPP1, p2, TP901-1) which have long, flexible non-contractile tails; and the family *Podoviridae* (e.g., φ29, T7, P22) which have short non-contractile tails. Of the tailed phages analyzed to date using electron microscopy, 61% are from the family *Siphoviridae*, 25% from the family *Myoviridae*, and 14% from the family *Podoviridae* [3].

To infect a host cell, bacteriophages attach to specific receptors on the surface of bacteria,

including lipopolysaccharides, teichoic acids, proteins, or even flagella. Myovirus bacteriophages use their contractile injection machinery to mechanically pierce the cell membrane and transfer their genetic material into the cell. By contrast, Podoviruses lack an elongated contractile tail and instead employ small tooth-like tail fibers to enzymatically carve an entrance site in the cell membrane for inserting their genome. For more details on the comparison of the tailed bacteriophages, refer to [3].

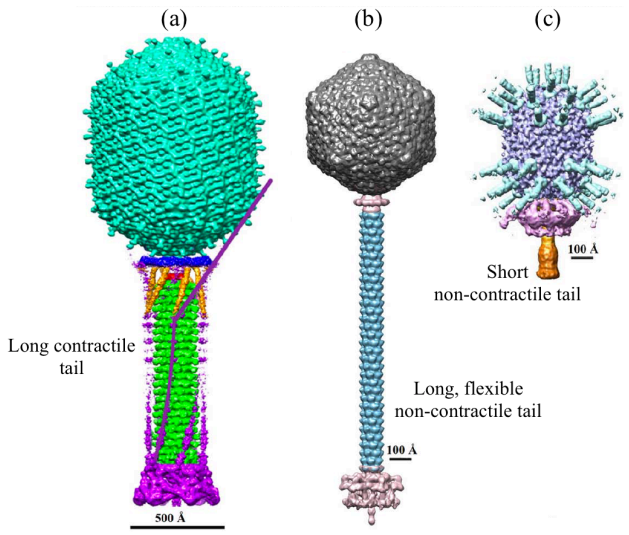

Figure 1.1: Structure of the (a) *Myoviridae* phages (example T4) which possess long, contractile tails, (b) *Siphiviridae* phages (example TP901-1) which possess long, non-contractile, flexible tails, and (c) *Podoviridae* phages (example φ29) which possess short non-contractile tail [3].

1.2 Motivation for bacteriophage research

Early research on bacteriophages was done by d'Herelle [4] who was inspired to use phages to treat a boy suffering from disenteria. Later d'Herelle and scientists from Georgia (former USSR)

created an institute to study the properties of bacteriophages as antibacterial agents for treating bacterial infectious diseases including those afflicting soldiers in the Red Army [5]. However, following the discovery of antibiotics such as penicillin, bacteriophage therapies were abandoned for general use in the West. This trend likely resulted from both a lack of basic understanding of phage biology (leading to clinical failures) and the wide marketing of antibiotics that were easy to make, store and prescribe.

Research on phage therapies continued mainly in Russia and Georgia and perhaps not disseminated broadly to the international community. The advent of antibiotics in the mid-20th century, along with better overall understanding of disease and sanitation, led to major improvements in both the quality of life and life expectancy [6]. However, the wide adoption of common antibiotics has also accelerated bacterial resistance to these drugs, leading to an escalating cycle of antibiotic drug discovery followed by adaptation and resistance to new drugs by new bacterial strains. This challenge has led to renewed interest in phage therapy.

Recent studies point to several promising advantages of phage therapy over antibiotic therapy. For example, bacteriophages remain effective against multidrug-resistant pathogenic bacteria and can respond rapidly to phage-resistant mutants. While bacteria can develop resistance to phages, it is comparatively easier (and cheaper) to develop new phage variants than new antibiotic variants. For example, new phage variants can be developed in a few weeks versus the years typically needed to develop new antibiotics [2]. In addition, as reported in [7], phage therapies induce fewer side effects, such as allergic reactions and secondary infections, which can be prevalent with antibiotic treatments. Importantly, the antibiotic resistance of bacteria does not affect the infectious activities of phages. As a compelling recent example of phage therapy, scientists and physicians at the University of California San Diego School of Medicine saved the

first patient in the United States with an overwhelming, multidrug-resistant bacterial infection using phage therapy in April 2017. In addition, because contractile-tailed phages such as T4 are highly efficient genetic delivery machines, understanding their function also has major implications for future nanotechnology devices. Indeed, emerging bio-nanotechnologies exploit phage machinery for the detection and control of pathogens, for peptide display, in addition to the aforementioned benefits of phage therapy [8–10]. Thus, there remains strong motivation for understanding the basic science of bacteriophages.

The above discussions provide significant motivation for understanding the biology of bacteriophages. In particular, understanding phage structure and how that structure affects phage-cell interaction is at the root of better understanding phage infection and the treatments and/or technologies that follow. To this end, the major goal of this dissertation research is to advance our understanding of the mechanics of the phage injection machinery and its interaction with the host cell. For this purpose, we use phage T4 as our primary example as it represents one of the most complex bacteriophages from the family *Myoviridae.* We provide an overview what is known about the structure of phage T4 next.

1.3 Bacteriophage T4

1.3.1 Bacteriophage T4 structure and life cycle

Bacteriophage T4 from family Myoviridae is one of the most complex tailed viruses which infects E. coil (Escherichia coli) by injecting its DNA genome into the host cell using a highly efficient contractile injection machinery. E. coli is a gram-negative, rod-shaped bacterium (see Figure 1.2)

that is commonly found in the lower intestine of warm-blooded organisms. As illustrated in Figure 1.3, phage T4 possesses a 1195Å long and 860Å wide prolate capsid (head) [11] containing the 172 kilo-base (172 kb) genomic DNA [11]; Figure 1.3(a). The capsid is composed of more than 3000 polypeptide chains of at least 12 types of protein [12]. The molecular weight (MW) of the head and the genomic DNA are 194 MD (1Da=1.66053e-24 gram) and 112 MDa, respectively [13]. The long and contractile tail assembly extending from the head is approximately 1200Å long and with diameter 250Å [14].

During infection, the contractile tail penetrates the host cell to deliver the viral genome. The capsid connects to the tail assembly through the neck which is continuous with a cylindrical tail tube that is 940Å long and with a 96Å external diameter and a 43Å internal diameter [15]. Surrounding the tail tube is a spring-like sheath structure which stores elastic energy to power the injection process [14]. The sheath, which is 925Å long and 240Å in diameter [16], is composed of six helical protein strands that work in unison like six helical springs; refer to Figure 1.3(b). The sheath is formed from 138 subunits of gene product 18 (gp18) protein synthesized by the virus that are further coupled into 23 hexameric rings [17] visible in Figure 1.3(b)-(c). In the extended state, each ring is formed by six subunits 40.6 Å thick and rotated by 17.2° in a right-handed manner relative to the ring below [16]. The upper end of the sheath attaches to the neck and the lower end attaches to a baseplate that is 270Å high and 520Å in diameter [15] and composed of at least 14 proteins [14]. Six long and six short tail fibers extend from the baseplate and are responsible for recognizing and attaching the phage to the host. Further details of the structure of T4 can be found in [12,14,17].

As illustrated in Figure 1.4, phage T4 infects *E. coli* through a five-step lytic cycle. In this cycle, phage T4 first recognizes and binds the host cell using its long and short fibers (Figure

1.4(a)), and then, injects its genome into the host using the aforementioned contractile injection machinery (Figure 1.4(b)). Next, the injected genome undergoes transcription, replication, and assembly (Figure 1.4(c-d)) within the host yielding the next generation bacteriophages. In doing so, 50-200 new phages are formed followed by bacterial cell lysis and death (Figure 1.4(e)). The new phages are released into the extracellular space to infect the other cells.

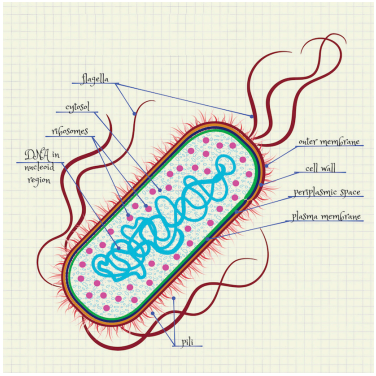

Figure 1.2: Schematic of *E. coli* structure adopted from https://sp.depositphotos.com/vector-images/flagelo.html.

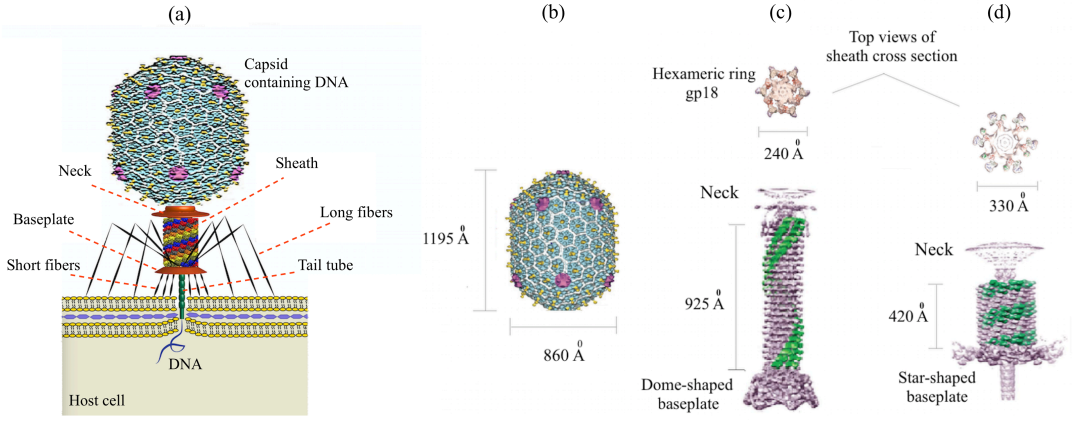

Figure 1.3: (a) Major structural components of bacteriophage T4. Images (b–d) show cryo-EM-resolved components of T4 including: (b) the multiprotein icosahedral capsid (adapted with permission from [11], Copyright (2004) National Academy of Sciences, Washington, DC), (c) neck/tail assembly/baseplate in pre-contraction (extended) conformation, and (d) neck/tail assembly/baseplate in post-contraction (contracted) conformation (adapted with permission from [18]).

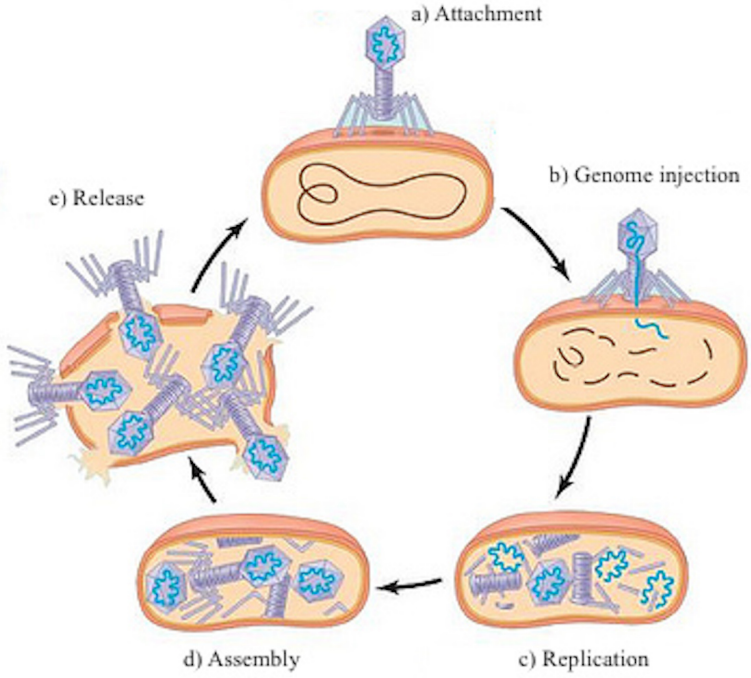

Figure 1.4: A schematic of the lytic life cycle of bacteriophage T4 adopted from https://socratic.org/questions/what-are-the-differences-between-a-lytic-infection-and-a-lysogenic-infection.

1.3.2 Bacteriophage T4 injection machinery

To begin the injection process, the receptor binding proteins at the tip of the long tail fibers (LTFs) recognize the cell and interact reversibly with the lipopolysaccharide molecules of the cell surface [19]; see Figure 1.5(a-b). Each LTF consists of a 700Å-long distal end (gp36 and gp37) and a 700Å-long proximal portion (gp34) connecting to the baseplate [17]. Binding the LTFs to the cell surface stimulates phage T4 to move toward the cell surface (Figure 1.5(b)). In doing so, the dome-shaped structure of baseplate approaches to about 100-200Å from the cell surface [20].

Then, the baseplate undergoes a large conformational change from a high-energy dome-shaped structure to a low-energy star-shaped structure [21]. In doing so, the 340Å-long short tail fibers (STFs) [22], gp12, rotate downward about 90 degrees [17] and anchor the cell surface irreversibly (Figure 1.5(c)). This conformational change of the baseplate triggers the contraction of the sheath upon releasing the tip of the tail tube [23]; see Figure 1.5(c-e)).

During contraction, the sheath (gp18) undergoes a large, nonlinear conformational change from a high-energy extended state (Figure 1.5(c)), that is 925Å long and 240Å in diameter, to a low-energy contracted state (Figure 1.5(e)), that is 420Å long and 330Å in diameter [16]. The conformational change derives from the relative rotation and translation of the gp18 subunits. The sheath is composed of six interacting helical strands, each of which possesses 23 gp18 subunits. The helical strands connect to the neck at the upper end and to the baseplate at the lower end. As previously mentioned, the strands also couple laterally in forming 23 hexameric rings. Following sheath contraction, the rise and twist between adjacent rings of the gp18 subunits change from 40.6 to 16.4Å and from 17.2 to 32.9 degrees, respectively [17]. Accordingly, the 920Å-long and 90Å-diameter rigid tail tube (gp19) [17] and 1195Å-long and 860Å-diameter capsid [11] simultaneously rotate counterclockwise (by 345.4 degrees) about and translate downward (by 505Å) along the tail tube axis. This dynamic translation and rotation ultimately enables the tip of the tail tube to pierce the host cell membrane. The helical parameters of the tube are close to those of the sheath in the extended (pre-contraction) conformation. In particular, the gp19 rings of the tail tube form a helical structure with six-fold symmetry having rise of 42Å and twist of 17.9 degrees [24]. The rapid rotation and translation of the tail assembly during sheath contraction provides the required energy for the tip of the tail tube to penetrate the cell membrane. The needle-like tip of the tail tube, called the central spike complex, consists of proteins gp27-gp5-gp5.4,

where gp5 is cleaved to form gp5* and gp5C during phage assembly [24]. The spike structure connects to the tail tube by two annuli of gp54 and gp48. Gp5.4 forming the apex domain of the spike complex is not well understood yet for phage T4. However, the structure of the apex domain for other contractile phages like P2 and ϕ92 reveal sharp and stable structures [24] which function as a rigid needle to mechanically pierce the outer cell membrane [20].

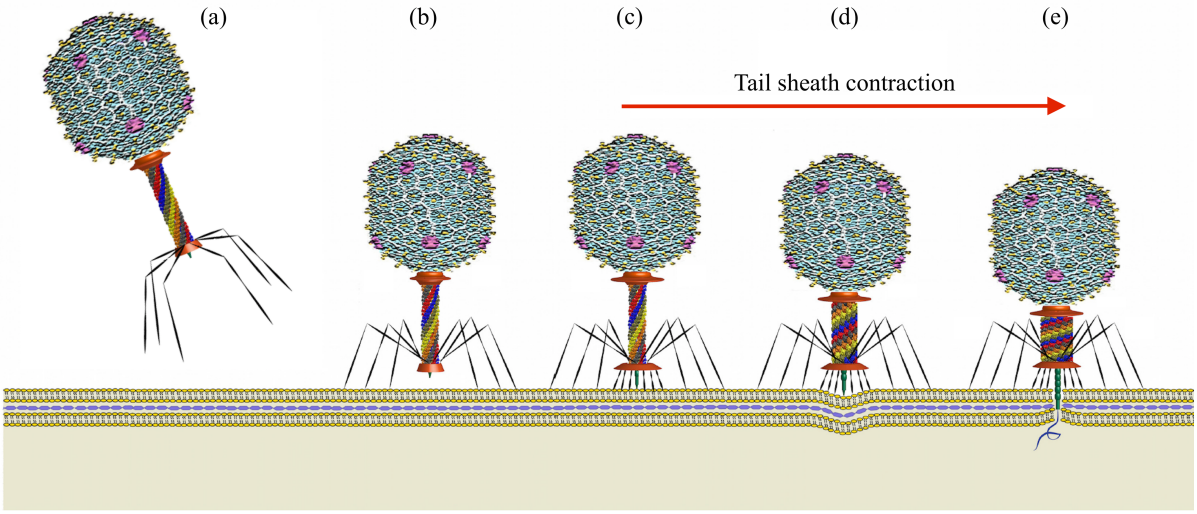

Figure 1.5: A schematic of the bacterial infection process. Phage T4 recognizes the host cell (a) and binds to the cell membrane (b) using the long tail fibers. The baseplate undergoes a large conformational change from a dome-shaped to a star-shaped structure and the short fibers attach to the cell irreversibly, (c) which initiates sheath contraction from the extended state to the contracted state (d). During sheath contraction, the rigid tail tube pierces the cell host outer membrane and initiates translocation of DNA into the host (e).

From cryo-EM data [20], it can be hypothesized that DNA is finally channeled into the cell in three major steps. First, the needle tip of the spike structure (gp5.4) mechanically pierces the soft layers of outer membrane (lipoprotein and lipopolysaccharide) [20]. Next, the tube penetrates through the periplasmic space and the lysozomic activity of gp5* degrades the stiffer layer of the cell wall (peptidoglycan). Finally, the cytoplasmic membrane bulges locally outward (by 160Å) (Figure 1.5(e)) to fuse with the tail tube and to complete the conduit for translocating DNA into the cytoplasm [23]. During penetration, the tip of the tail tube (gp5C, gp5*, and gp5.4), which is about 160Å long, dissociates from the remainder of the tube [23].

1.4 Prior experiments and models of the phage T4 injection machinery

A large number of studies have contributed to our knowledge of bacteriophage T4 structure including the components of the injection mechanism; see for example [15–17] and the other studies reviewed above. Despite this wealth of data available on the *structure* of T4 using cryo-electron microscopy (cryo-EM) and x-ray crystallography, we lack a fundamental understanding of how this intricate machinery works including the dynamics, energetics, and time scale of the injection process. Our lack of knowledge is partly attributed to the paucity of experiments that aim to measure the dynamics and/or energetics of the injection process.

One experiment [25] probed the enthalpic change of the phage T4 contraction process using microcalorimetric methods. In this study, contraction was induced *in vitro* by both heat and urea [25]. Subsequently, Moody [26,27] predicted a possible "contraction wave" pathway for sheath contraction from observation of electron micrographs of partially contracted sheaths in vitro [26,27]. He proposed that the sheath contraction mechanism is likely *displacive* [28] with

contraction initiating at the baseplate and propagating towards the neck. Later, Caspar [29] devised a large mechanical model to visualize the sheath contraction mechanism predicted by Moody. Caspar's mechanical model employed temporary links between all subunits of the sheath and the tail tube that were released sequentially starting from the baseplate to the neck. A recent and related experimental study of bacteriophage A511 by Guerrero-Ferreira et al [30] confirms the wave propagation mechanism of sheath contraction. Bacteriophage A511 is a virus that infects *Listeria monocytogenes* and *L. ivanovii*. The contractile injection machinery of A511 is very similar to that of phage T4 [30]. The experiment, conducted under near-native conditions, confirms that sheath contraction starts from the baseplate and propagates toward the neck, similar to what is believed to occur for phage T4 [30].

In addition, Falk and James [31] used elasticity theory to describe an approximate (coarse-grained) free energy surface for the extended to contracted conformational change of the T4 sheath. Unfortunately, that (static) theory fails to account for any dynamics of the process as well as interactions with the remaining subdomains of the virus and the host cell.

In principle, the dynamics of sheath contraction could be simulated with atomic detail using molecular dynamics (MD) simulations [32], and results could be used to understand the inner workings of all of the structural components described above. However, the atomic structure of phage T4 represents an extremely large system, one that incorporates multiple millions of atoms (e.g., approximately one million atoms would be required just for the T4 sheath alone, plus the surrounding water, tail tube, and base-plate [33]). In addition, the time scales currently achievable by molecular dynamics simulations for such large systems fall short (by approximately six orders of magnitude) of the expected millisecond or longer time scales needed for transitioning dynamically from the extended to the contracted state. Thus, it is presently impossible to simulate

the entire T4 injection machinery in atomistic resolution and over biologically relevant (e.g., millisecond) timescales using today's computing power. An attractive alternative is to leverage coarse-grained continuum models of the actively changing protein structures, and specifically the elastic sheath. In particular, a nonlinear continuum model of the sheath, formed by six interacting elastic rods, should be capable of resolving the large conformational changes of the sheath that powers the entire injection process and over biologically-relevant timescales. This dissertation advances that approach considerably in developing a system-level model describing the nonlinear dynamics of the phage T4 injection machinery coupled to the remainder of the virus and its interaction with the host cell.

1.5 Continuum rod model

Modeling the sheath as six interacting elastic rods draws from the field of structural dynamics, where a "rod" is a thin structure that may undergo bending, torsional, extensional, or shear deformations, depending upon the loading conditions. Both equilibrium (static) and dynamic rod models are commonly used to represent the mechanics of biological filaments and single molecules including cilia, flagella, and DNA; see for example [34–37]. In this dissertation we employ a dynamic rod model to simulate each of the six strands of the sheath connected to the remaining structures of T4 and interacting with the host cell. During the injection process, the sheath strands undergo large conformational changes inducing large rotations and displacements of gp18 subunits. To model this large conformational change, we employ the *nonlinear dynamic* rod model developed from Kirchhoff rod theory. We assume that each strand (rod) undergoes geometrically large deformations which remaining unshearable and inextensible. Prior numerical formulations of this theory [34–37] successfully predict the highly nonlinear looped, supercoiled and buckled conformations of DNA.

1.6 Research objective

The objective of this research is to contribute a theoretical model to expose the energetics and dynamics of contractile injection systems (e.g., bacteriophages from the family *Myoviridae*). Using phage T4 as a motivating example, this dissertation contributes a novel (course-grain) continuum model for the T4 sheath whose elastic parameters are estimated from an atomistic (MD) model of a small fragment of the sheath assembly. The resulting multi-scale model captures the nonlinear dynamics of the T4 injection machinery and its coupling to the remainder of the virus and its interaction with the host cell. This multi-scale approach may be readily extended to other contractile tail injection machines such as those arising in phage ϕ812 and R2-pyocin as additional examples. We employ this model to explore the energetics and dynamics of the injection process including the large conformational changes of the energy-storing sheath, the time scale of the injection process, and the force/thrust required to rupture the host cell membrane. The resulting theoretical model may have future implications for advancing both medicine and nanotechnology considering the aforementioned opportunities for phage therapy and for harnessing viral machines for nano-scale gating, sensing, translocation, and peptide display.

1.7 Research scope

To simulate the dynamics of the injection process, we first decompose the phage T4 - cell system into three major constituent structures. These include: 1) the elastic T4 sheath that powers the injection machine, 2) the predominantly rigid domains (capsid, tail tube, etc.), and 3) the flexible host cell. Significant challenges exist in modeling the elastic sheath as it undergoes a large (nonlinear) conformational change from the extended to contracted states. We address that

challenge by using a two-stage modeling approach. In stage 1, we employ the results of a molecular dynamic (MD) simulation to estimate the elastic properties of the sheath strands using atomistic modeling of a small fraction of the sheath. In stage 2, we employ a (coarse-grained) nonlinear continuum model of the sheath composed of six interacting helical protein strands. The resulting sheath model is then coupled to a model of the remaining (rigid) components of the mature virus which is then coupled to a model of the host cell. The fully assembled system-level model is ultimately used to simulate the dynamics of the entire injection process.

The aforementioned stage 1 atomistic modeling was carried out by our collaborators in the Andricioaei group at the University of California at Irvine. We use the elastic constants estimated from that effort in the continuum model of the sheath. In addition to revealing the dynamics and energetics of phage T4, the same method could be applied to other contractile tail injection machines; for instance, those employed by phage ϕ812 and R2-pyocin. The scope of this effort is broken down into five chapters briefly summarized next.

1.7.1 Approximation of the phage T4 sheath by a single helical protein strand

In Chapter 2, we propose a dynamic model for the helical protein strands that constitute the backbone of the elastic sheath. A single helical chain or strand is represented by a nonlinear elastic rod (Kirchhoff rod theory) which stores and then releases elastic energy to drive the injection process. The resulting model captures the transient response of this simple approximation of the flexible sheath coupled to a rigid body model of the capsid and tail tube at one end and to the baseplate at the opposite end. Hydrodynamic forces on the capsid model the effect of the surrounding aqueous environment. This chapter contributes a foundational one-strand model of

the sheath that we systematically extend into a complete six-strand model of the entire sheath structure in Chapter 3.

1.7.2 Model of the phage T4 sheath as six interacting helical protein strands

In Chapter 3, we extend the dynamic model of the single-stranded sheath of Chapter 2 to create a sheath model comprised of the six interacting helical protein strands. In doing so, the shell-like structure of sheath is modeled by six interacting helical rods that capture both inter- and intra-strand interactions. The resulting sheath model is coupled to a rigid (and relatively massive) body representing the capsid/DNA/neck/tube assembly at the upper end and to the baseplate at the lower end. The elastic stiffness constants of the interacting sheath strands are obtained from molecular dynamic simulation (of one-fifth of sheath) provided by our collaborators in the Andricioaei lab at the University of California at Irvine. The high-energy extended sheath (before infection) and the low-energy contracted sheath (after infection) define, respectively, the initial state and the final state of injection machinery in our model. At this modeling stage, the hydrodynamic drag on capsid and sheath from surrounding water are considered as the sole source of energy dissipation, as we presently ignore the cell-tail tube interaction and sheath-tube interaction. Importantly, results from this chapter predict the total energy stored in the extended sheath which efficiently drives the injection machinery.

1.7.3 Modeling energy dissipation for the phage T4 injection machinery

In order to predict the time scale of the injection dynamics, one must also understand and quantify

the major sources of energy dissipation. There are numerous potential mechanisms of energy dissipation for the phage T4 injection machinery that include: 1) hydrodynamic drag on the capsid and sheath from the surrounding water (as also discussed in Chapter 3), 2) the interaction forces of the tip of the tail tube with the host cell membrane (both before and after rupturing the membrane), 3) the internal (material) dissipation of the sheath strands due to their large conformational change during sheath contraction, and 4) the interaction forces between the contractile sheath and the (rigid) tail tube during sheath contraction. Chapter 3 provides a model for mechanism #1 above, and this chapter proposes models for the remaining mechanisms (#2-#4). For mechanism #2, we present a viscoelastic model for the cell membrane before cell rupture and a hydrodynamic drag model after tube penetration into the cell. For mechanism #3, we develop a new theory to describe the internal dissipation of general biofilaments (such as the helical sheath strands) during coupled shear-bending deformations (induced during the injection process). Finally, for mechanism #4, we consider the viscous forces present in the fluid-filled, nano-scale gap between the sheath and the tail tube. The resulting models of these dissipation mechanisms are subsequently incorporated in a complete, system-level model of the phage T4 injection process in the next chapter.

1.7.4 Complete system-level dynamic model of phage T4 interacting with host cell

In Chapter 5, we combine the models developed in Chapters 2-4 to create a comprehensive model of the entire phage T4 interacting with a host cell. A major component remains the elastic sheath described by six interacting helical protein strands using elastic stiffness constants estimated from MD simulation. The sheath attaches to a rigid (and relatively massive) body representing the

capsid/DNA/neck/tube assembly at the upper end and the stationary baseplate at the lower end. The sources of energy dissipation identified in Chapter 4 are added to the model including: 1) hydrodynamic drag on capsid and sheath from the surrounding water, 2) the cell-tail tube interaction before and during cell membrane rupture, 3) internal dissipation of the sheath strands during sheath contraction, and 4) sheath-tube hydrodynamic interaction. Numerical solution of the governing coupled dynamical equations describes the dynamics of the entire injection process and provides, for the first time, estimates of the energetics, pathway, and time scale of the injection process, as well as the required force/thrust for cell membrane rupture.

1.7.5 Summary, major contributions, and future work

In Chapter 6, we first, summarize the contribution and major findings of our dynamic model for phage T4 injection machinery interacting with the host cell. Then, we lay out the foundation for future research based on dynamic model of phage T4. The dynamic model proposed for the phage T4 injection machinery can be extended to simulate the dynamics of other similar contractile injection systems, for instance, R2-pyocin and phage ϕ812. R2-pyocin.

Chapter 2

Approximation of the phage T4 sheath by a single protein strand

This chapter is adopted from the publication:

Maghsoodi, A., Chatterjee, A., Andricioaei, I., and Perkins, N. C. (2016). A first model of the dynamics of the bacteriophage T4 injection machinery. Journal of Computational and Nonlinear Dynamics, 11(4), 041026.

This chapter contributes an approximate model of the contractile injection machinery that is driven by elastic energy stored in a structure known as the sheath. The sheath is composed of helical strands of protein that suddenly collapse from a high energy, extended conformation prior to infection to a relaxed, contracted conformation during infection. To simulate the dynamics of the injection machinery, we propose a model for the helical protein chains that constitute the backbone of the elastic sheath. A single helical chain or strand is represented by an elastic rod which stores and then releases the energy to drive the injection process. The helical elastic strand is coupled to a model of the capsid and tail tube at one end and to the baseplate at the opposite end. Doing so contributes an essential component model of the sheath that build upon in the remainder of this dissertation. In Section 1, the dynamical rod model is formulated with initial and boundary

conditions relevant to the bacteriophage T4 injection machinery. In Section 2, we first validate our numerical formulation by comparing the computed natural frequencies of a single helical strand to known results for a (nanoscale) helical spring. The resulting procedure is then employed to simulate the rapid injection process as revealed by the transient dynamics and energetics of the coupled strand–capsid–tail tube system. Section 3 provides conclusions and comments. This chapter draws largely from our published paper [38].

2.1 Methods

As suggested in Figure 2.1, a helical strand of gp18 can be modeled as an elastic rod as a coarse-grain approximation which sacrifices atomic detail in favor of describing the overall three-dimensional bending and twisting of the strand centroidal axis. The single helical strand connects to the capsid/neck/tail tube assembly at the upper end and to the baseplate at the lower end (See Figure 2.1(a)). We represent the capsid/neck/tail tube assembly as a single rigid body in the shape of a cylinder that mimics the large capsid volume. During injection, this cylinder undergoes rapid translation along and rotation about the tail tube axis driven by the large reaction force/moment from the helical strand and subjected to hydrodynamic drag. We begin below by summarizing the dynamic rod model of the helical strand.

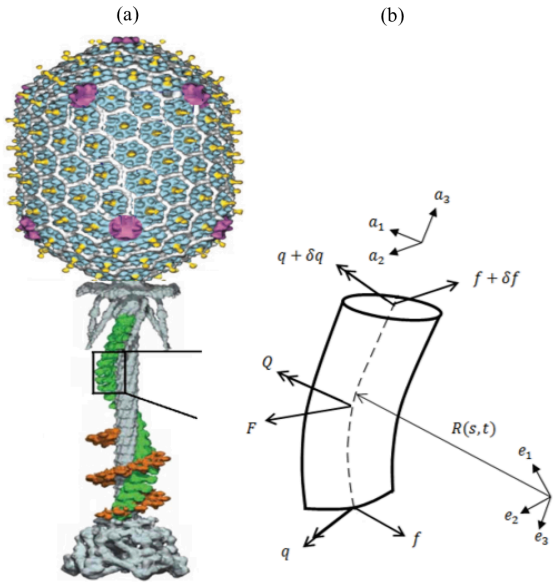

Figure 2.1: (a) A helical strand of gene product 18 (gp18) in extended (green) and contracted (orange) conformations. Image adapted with permission from Refs. [16] and [11]. (b) Infinitesimal element of a Kirchhoff rod as a nonlinear rod model of the helical strand of gp18.

2.1.1 Dynamic rod model of a helical strand

Referring to Figure 2.1(b), consider a segment of a helical strand as the infinitesimal element of a Kirchhoff rod with equivalent averaged elastic properties. The shape of the rod is parameterized by the three-dimensional centerline curve $\boldsymbol{R}(s,t)$ and the body-fixed frame at each cross-section $\{a_i\}$ where s denotes the contour-length coordinate measured from the baseplate (bottom) end and t denotes time. The balance laws of linear and angular momentum for a Kirchhoff rod element resolved in the body-fixed frame are [35]

$$\frac{\partial \boldsymbol{f}}{\partial s} + \boldsymbol{\kappa} \times \boldsymbol{f} = m_s \left(\frac{\partial \boldsymbol{v}}{\partial t} + \boldsymbol{\omega} \times \boldsymbol{v} \right) - \boldsymbol{F}_{body} \, , \tag{2.1}$$

$$\frac{\partial \boldsymbol{q}}{\partial s} + \boldsymbol{\kappa} \times \boldsymbol{q} = \boldsymbol{I_s} \, \frac{\partial \boldsymbol{\omega}}{\partial t} + \boldsymbol{\omega} \times \boldsymbol{I_s} \, \boldsymbol{\omega} + \boldsymbol{f} \times \boldsymbol{a_3} - \boldsymbol{Q}_{body} \, , \tag{2.2}$$

where $\boldsymbol{\kappa}(s,t)$ is the curvature/twist vector defined as the rotation of the body-fixed frame $\{a_i\}$ per unit contour length relative to the inertial frame $\{e_i\}$, $\boldsymbol{\omega}(s,t)$ is the angular velocity of the cross-section defined as the rotation of the body-fixed frame $\{a_i\}$ per unit time relative to the inertial frame $\{e_i\}$, $\boldsymbol{v}(s,t)$ is the velocity of the strand cross-section centroid, $m_s(s)$ is the mass of the strand per unit contour length, and $\boldsymbol{I}_s$(s) denotes the diagonal 3×3 tensor of principal mass moments of inertia per unit contour length. The quantities $\boldsymbol{f}(s,t)$ and $\boldsymbol{q}(s,t)$ are the internal force vector and internal moment vector, respectively. Finally, $\boldsymbol{F}_{body}(s,t)$ and $\boldsymbol{Q}_{body}(s,t)$ denote the sum of all distributed external body forces and moments per unit contour length, respectively, and $\boldsymbol{a_3}$ is the unit tangent vector. (Note: $\boldsymbol{F}_{body}$ and $\boldsymbol{Q}_{body}$ may also be functions of the kinematic variables $\boldsymbol{\kappa}(s,t)$, $\boldsymbol{\omega}(s,t)$ and $\boldsymbol{v}(s,t)$). In equations ((2.1) and (2.2), the quantities $\boldsymbol{\kappa}(s,t)$, $\boldsymbol{\omega}(s,t)$, $\boldsymbol{v}(s,t)$ and $\boldsymbol{f}(s,t)$ define four unknown field variables which also satisfy two additional field equations

$$\frac{\partial \boldsymbol{v}}{\partial s} + \boldsymbol{\kappa} \times \boldsymbol{v} = \boldsymbol{\omega} \times \boldsymbol{a_3} \, , \tag{2.3}$$

$$\frac{\partial \boldsymbol{\omega}}{\partial s} + \boldsymbol{\kappa} \times \boldsymbol{\omega} = \frac{\partial \boldsymbol{\kappa}}{\partial t} \, . \tag{2.4}$$

Equation (2.3) enforces assumed inextensibility and unshearability constraints for the strand while equation (2.4) is a compatibility constraint that guarantees the smoothness of $\boldsymbol{\omega}$ and $\boldsymbol{\kappa}$. In equation (2.2), the internal moment $\boldsymbol{q}(s,t)$ is related to the curvature/twist vector through an assumed linear elastic constitutive law

$$\boldsymbol{q}(s,t) = \boldsymbol{B}\big(\boldsymbol{\kappa}(s,t) - \boldsymbol{\kappa_0}(s)\big)\,, \tag{2.5}$$

where $\boldsymbol{\kappa_0}(s)$ is the known intrinsic curvature/twist vector of the helical strand in a stress-free state and $\boldsymbol{B}$ is a diagonal 3×3 stiffness tensor composed of the bending and torsional stiffness coefficients of the equivalent rod. The four vector equations (2.1)-(2.4) containing the four vector unknowns $\{\boldsymbol{v}, \boldsymbol{\omega}, \boldsymbol{\kappa}, \boldsymbol{f}\}$ result in a 12th order system of nonlinear partial differential equations which are solved numerically following non-dimensionalization.

To this end, we introduce the non-dimensional space and time variables

$$\bar{s} = \frac{s}{L}\,, \quad \bar{t} = \frac{t}{P_0}\,, \qquad \text{where} \quad P_0 = \sqrt{\frac{m_s L^4}{EJ}} \tag{2.6}$$

where L is total contour length of the strand, E is Young's modulus, and J is the area moment of inertia for bending of the assumed circular rod cross-section. Substituting (2.6) into (2.1)-(2.4) results in the following non-dimensional equations

$$\frac{\partial \bar{\boldsymbol{f}}}{\partial \bar{s}} + \bar{\boldsymbol{\kappa}} \times \bar{\boldsymbol{f}} = \frac{\partial \bar{\boldsymbol{v}}}{\partial \bar{t}} + \bar{\boldsymbol{\omega}} \times \bar{\boldsymbol{v}} - \bar{\boldsymbol{F}}_{body}\,, \tag{2.7}$$

$$\frac{\partial \bar{\boldsymbol{q}}}{\partial \bar{s}} + \bar{\boldsymbol{\kappa}} \times \bar{\boldsymbol{q}} = \bar{\boldsymbol{I}}_{\boldsymbol{s}} \frac{\partial \bar{\boldsymbol{\omega}}}{\partial \bar{t}} + \bar{\boldsymbol{\omega}} \times \bar{\boldsymbol{I}}_{\boldsymbol{s}} \bar{\boldsymbol{\omega}} + \bar{\boldsymbol{f}} \times \boldsymbol{a_3} - \bar{\boldsymbol{Q}}_{body}\,, \tag{2.8}$$

$$\frac{\partial \bar{\boldsymbol{v}}}{\partial \bar{s}} + \bar{\boldsymbol{\kappa}} \times \bar{\boldsymbol{v}} = \bar{\boldsymbol{\omega}} \times \boldsymbol{a_3} \,, \tag{2.9}$$

$$\frac{\partial \bar{\boldsymbol{\omega}}}{\partial \bar{s}} + \bar{\boldsymbol{\kappa}} \times \bar{\boldsymbol{\omega}} = \frac{\partial \bar{\boldsymbol{\kappa}}}{\partial \bar{t}} \,, \tag{2.10}$$

where all quantities with an overbar are non-dimensional as defined in Appendix A.

Equations (2.7)-(2.10) can be written in the compact operator form

$$\bar{\boldsymbol{M}}(\bar{\boldsymbol{Y}}, \bar{s}, \bar{t}) \, \frac{\partial \bar{\boldsymbol{Y}}}{\partial \bar{t}} + \bar{\boldsymbol{K}}(\bar{\boldsymbol{Y}}, \bar{s}, \bar{t}) \frac{\partial \bar{\boldsymbol{Y}}}{\partial \bar{s}} + \bar{\boldsymbol{F}}(\bar{\boldsymbol{Y}}, \bar{s}, \bar{t}) = 0 \,, \tag{2.11}$$

where $\bar{\boldsymbol{Y}}(\bar{s}, \bar{t}) = \{\bar{\boldsymbol{v}}, \bar{\boldsymbol{\omega}}, \bar{\boldsymbol{\kappa}}, \bar{\boldsymbol{f}}\}$ and

$$\bar{\boldsymbol{M}} = \begin{bmatrix} \boldsymbol{\Theta} & \boldsymbol{\Theta} & \boldsymbol{\Theta} & \boldsymbol{\Theta} \\ \boldsymbol{\Theta} & \boldsymbol{\Theta} & \mathbb{I} & \boldsymbol{\Theta} \\ \boldsymbol{\Theta} & \bar{\boldsymbol{I}}_{\boldsymbol{s}} & \boldsymbol{\Theta} & \boldsymbol{\Theta} \\ \mathbb{I} & \boldsymbol{\Theta} & \boldsymbol{\Theta} & \boldsymbol{\Theta} \end{bmatrix}, \quad \bar{\boldsymbol{K}} = -\begin{bmatrix} \mathbb{I} & \boldsymbol{\Theta} & \boldsymbol{\Theta} & \boldsymbol{\Theta} \\ \boldsymbol{\Theta} & \mathbb{I} & \boldsymbol{\Theta} & \boldsymbol{\Theta} \\ \boldsymbol{\Theta} & \boldsymbol{\Theta} & \bar{\boldsymbol{B}} & \boldsymbol{\Theta} \\ \boldsymbol{\Theta} & \boldsymbol{\Theta} & \boldsymbol{\Theta} & \mathbb{I} \end{bmatrix},$$

$$\bar{\boldsymbol{F}} = \begin{Bmatrix} \bar{\boldsymbol{\omega}} \times \boldsymbol{a_3} - \bar{\boldsymbol{\kappa}} \times \bar{\boldsymbol{v}} \\ -\bar{\boldsymbol{\kappa}} \times \bar{\boldsymbol{\omega}} \\ -\left(\frac{\partial \bar{\boldsymbol{B}}}{\partial \bar{s}} \bar{\boldsymbol{\kappa}} - \frac{\partial (\bar{\boldsymbol{B}} \bar{\boldsymbol{\kappa}}_{\boldsymbol{0}})}{\partial \bar{s}}\right) + \bar{\boldsymbol{\omega}} \times \bar{\boldsymbol{I}}_{\boldsymbol{s}} \bar{\boldsymbol{\omega}} + \bar{\boldsymbol{f}} \times \boldsymbol{a_3} - \bar{\boldsymbol{\kappa}} \times \bar{\boldsymbol{B}}(\bar{\boldsymbol{\kappa}} - \bar{\boldsymbol{\kappa}}_{\boldsymbol{0}}) - \bar{\boldsymbol{Q}}_{body} \\ \bar{\boldsymbol{\omega}} \times \bar{\boldsymbol{v}} - \bar{\boldsymbol{\kappa}} \times \bar{\boldsymbol{f}} - \bar{\boldsymbol{F}}_{body} \end{Bmatrix}.$$

Here, $\boldsymbol{\Theta}$ and $\mathbb{I}$ are the 3×3 zero and identity matrices, respectively. For future reference, the total (non-dimensional) elastic energy $\overline{U}$, and kinetic energy $\overline{K}$, for the strand are

$$\overline{U}(t) = \int_0^1 \left[\frac{1}{2} \, (\bar{\boldsymbol{\kappa}} - \bar{\boldsymbol{\kappa}}_{\boldsymbol{0}})^T \bar{\boldsymbol{B}} (\bar{\boldsymbol{\kappa}} - \bar{\boldsymbol{\kappa}}_{\boldsymbol{0}})\right] \mathrm{d}\bar{s} \,, \tag{2.12}$$

$$\overline{K}(t) = \int_0^1 \left[\frac{1}{2}\,\bar{\boldsymbol{\omega}}^T\,\bar{\boldsymbol{I}}_{\boldsymbol{s}}\,\bar{\boldsymbol{\omega}} + \frac{1}{2}\,\bar{\boldsymbol{v}}^T\,\bar{m}_s\,\bar{\boldsymbol{v}}\right] \mathrm{d}\bar{s}. \tag{2.13}$$

The theory is completed upon specifying the following initial and boundary conditions for the T4 injection process.

2.1.2 Initial and boundary conditions

Equation (2.11) is a 12th order system of partial differential equations in space and time which is solved for the field variables $\overline{\boldsymbol{Y}}(\bar{s},\bar{t}) = \{\bar{\boldsymbol{v}}, \bar{\boldsymbol{\omega}}, \bar{\boldsymbol{\kappa}}, \bar{\boldsymbol{f}}\}$ under specified initial and boundary conditions (six at each boundary). For the T4 injection process, it is natural to first define the boundary conditions in the inertial frame and subsequently transform the boundary conditions to those in the body fixed frame consistent with (2.11). As shown in Figure 2.2, this first model of the T4 injection process includes the (nonlinear) rod representation of a single protein strand attached at its upper end to a large rigid cylinder representing the capsid/neck/tail tube assembly at the point of attachment denoted by A. The cylinder has two degrees of freedom defined by the translation along and the rotation about the tail tube (e_3) axis. During contraction, both the velocity $\bar{v}_{e3}$ along and the angular velocity $\bar{\omega}_{e3}$ about the tail tube axis are unknowns while no rotation occurs about the e_1 and e_2 directions.

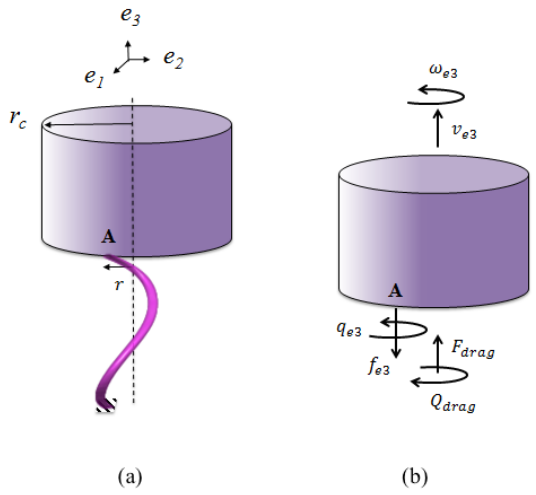

Figure 2.2: (a) A first model of the phage injection machinery as represented by a single helical protein strand that drives the motion of the attached capsid/neck/tail tube assembly. (b) Free body diagram of capsid/neck/tail tube assembly during contraction.

Therefore, the boundary conditions at the upper end ($\bar{s} = 1$) of the strand are

$$\bar{\omega}_{e1}(1,\bar{t}) = 0 \ , \ \bar{\omega}_{e2}(1,\bar{t}) = 0 \ , \tag{2.14.a}$$

$$\bar{v}_{e1}(1,\bar{t}) = -\bar{r}_{e2}\,\bar{\omega}_{e3} \ , \bar{v}_{e2}(1,\bar{t}) = \bar{r}_{e1}\,\bar{\omega}_{e3} \ , \tag{2.14.b}$$

$$\bar{\boldsymbol{f}}^{\boldsymbol{A}}_{\boldsymbol{e3}} + \bar{\boldsymbol{F}}_{\boldsymbol{drag}} = \bar{m}_c \frac{\partial\, \bar{\boldsymbol{v}}_{\boldsymbol{e3}}}{\partial \bar{t}}, \tag{2.14.c}$$

$$\bar{\boldsymbol{q}}^{\boldsymbol{A}}_{\boldsymbol{e3}} + \left(\bar{\boldsymbol{r}} \times \bar{\boldsymbol{f}}^{\boldsymbol{A}}\right)_{\boldsymbol{e3}} + \bar{\boldsymbol{Q}}_{\boldsymbol{drag}} = \bar{I}_c \frac{\partial \bar{\boldsymbol{\omega}}_{\boldsymbol{e3}}}{\partial \bar{t}},$$

where $\bar{v}_{e1}$ and $\bar{v}_{e2}$ (2.14.a) are the components of velocity of point A in the plane $e_1 - e_2$ induced by rotation about the cylinder axis, and similarly, $\bar{r}_{e1}$ and $\bar{r}_{e2}$ denote the components of the

normalized position vector $\bar{\boldsymbol{r}}$ from the cylindrical axis to point A. Equations (2.14.a) are the linear and angular momentum balance laws for the cylinder along e_3 which are influenced by the hydrodynamic drag force and moment created by the surrounding physiological buffer defined by

$$\bar{\boldsymbol{F}}_{\boldsymbol{drag}} = -\bar{C}_t \bar{\boldsymbol{v}}_{\boldsymbol{e3}} \ , \tag{2.15}$$

$$\bar{\boldsymbol{Q}}_{\boldsymbol{drag}} = -\bar{C}_r \bar{\boldsymbol{\omega}}_{\boldsymbol{e3}} \ ,$$

Here, $\bar{C}_t$ and $\bar{C}_r$ are normalized force and moment drag coefficients, respectively. $\bar{I}_c$ and $\bar{m}_c = \frac{m_c}{m_s L}$ denote the normalized mass moment of inertia and mass of the cylinder representing that of the capsid/neck/tail tube assembly. Finally, the quantities $\bar{f}_{e3}^{A}$ and $\bar{q}_{e3}^{A}$ are the normalized reaction force and moment of the strand, respectively, at point A along the e_3 direction. At the lower end ($\bar{s} = 0$), the strand is attached to the stationary baseplate. Thus, there is no rotation or translation at this boundary as described by

$$\bar{\omega}_{ei}(0,\bar{t}) = 0 \ , \qquad \bar{v}_{ei}(0,\bar{t}) = 0 \ , \ i = 1,2,3. \tag{2.16}$$

During the injection process, the sheath undergoes a large conformational change from the extended to the contracted conformation. To simulate the extended sheath as the initial condition of the injection machinery, we solve the equations (2.7)-(2.10) with zero time-variant parameters such as translational and angular velocities to calculate the initial internal force and moment of the strand in the extended state. Note that the curvature/twist vector is known from cryo-EM in both extended and contracted states.

The nonlinear system of equations (2.11) is not integrable in closed form and this necessitates

employing a numerical solution at each time step. We use a finite difference formulation based on the generalized-α method for discretizing in both space and time domains following the procedure already summarized in [39]. Starting with an initial condition $\overline{\boldsymbol{Y}}(\bar{s}, 0)$ for the contracted state, the discretized equations are integrated over space at each successive time step. The boundary conditions are satisfied using a classical shooting method for boundary-value problems. The references [39] detail this numerical procedure.

2.2 Results and discussion

2.2.1 Validation: Limiting case of spring vibration

Before employing the above formulation for evaluating the injection machinery of T4, we validate the formulation by employing the model to replicate a known result. To this end, the system of equations (2.11) is used to compute the fundamental natural frequency of a nano-scale helical spring composed of protein. The approximate fundamental natural frequency f_0(Hz) for a clamped-free spring from linear theory [40] is

$$f_0 = \frac{d}{4\pi N D^2}\sqrt{\frac{G}{2\rho}}\ , \tag{2.17}$$

where d is the diameter of a thin rod forming N turns of a helical spring having diameter D, shear modulus G and density ρ. As an illustrative example, consider a spring composed of the protein actin that has $G = 0.766$ GPa and $\rho = 1380$ kg/m^3 [41]. We consider a nanoscale spring having $d = 10$ Å, $D = 300$ Å and $N = 3$. Evaluating equation (2.17), the fundamental frequency of

vibration of this example spring is 15.53 MHz. Next, we examine the free vibration of the same spring using the numerical formulation outlined above. For this example, the mass and dimensions of the attached cylinder are set to zero as are the hydrodynamic drag force and moment. We select the (normalized) time and space steps of $\overline{\Delta t} = 0.005$ and $\overline{\Delta s} = 0.01$, respectively, which yield converged results for this and all other examples in this chapter.

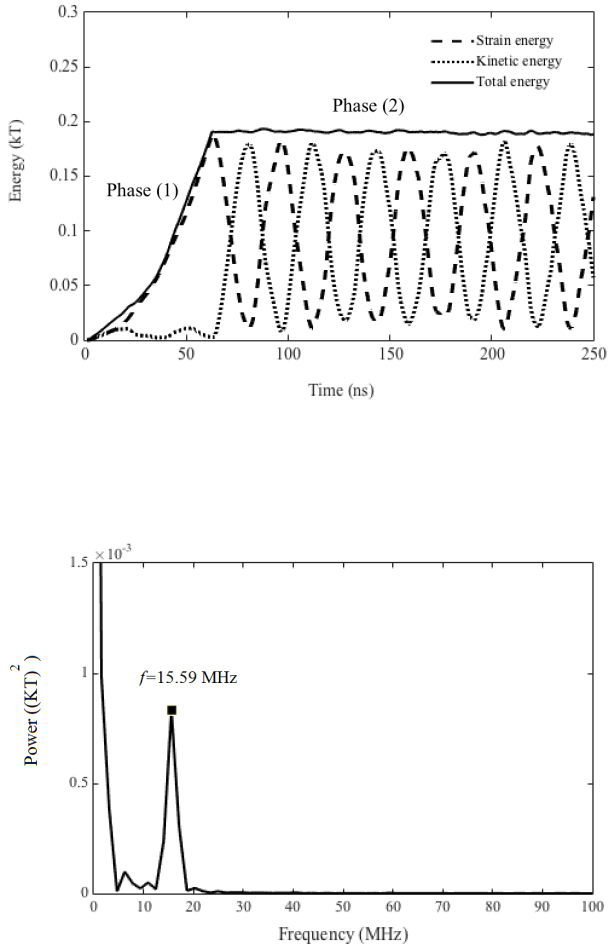

Figure 2.3: (a) Strain, kinetic, and total mechanical energies of a nanoscale protein spring. Phase 1: Stretching phase with prescribed velocity of free end. Phase 2: Free vibration phase following the release of the free end. Energy is reported in the units of kT, where k is the Boltzmann constant and T is the temperature (Kelvin), and time is reported in the units of nanoseconds. (b) Power spectrum of the strain energy of the nanoscale protein spring. Illustrated peak locates natural frequency of fundamental vibration mode.

We begin with stretching the spring by applying a constant vertical velocity $\bar{v}_{e3} = 0.5$ to the free end for the first 50 time steps which constitutes Phase 1 of our simulation. The free end is then suddenly released allowing the spring to freely vibrate during Phase 2. Figure 2.3(a) illustrates the computed spring kinetic (2.12) and strain (2.13) energies calculated during Phase 1 and Phase 2. Since there is no damping in this example, the total mechanical energy shown in Figure 2.3(a) remains constant (to within numerical approximation). The power spectrum of the strain energy shown in Figure 2.3(b) reveals that the frequency with the largest power (ignoring aliasing error) is 15.59 MHz. This numerical result replicates that above from linear theory (2.17) to within 0.5%. The remaining (small) difference can be attributed to the nonlinearities present in the (nonlinear) rod formulation and by numerical approximations.

2.2.2 Simulating the contractile injection machinery

Having validated the above formulation, we now employ it to simulate the injection process of bacteriophage T4. While the elastic properties of the protein strand gp18 remain unknown, we can assume that they are similar in magnitude to those of other protein filaments such as actin whose properties are well characterized [41]. (Note: we later estimate the stiffness parameters for the gp18 strands in Chapter 3 from MD simulation). We also estimate values for the mass, mass moment of inertia and drag coefficients for the capsid/neck/tail tube assembly in arriving at a first simulation of the dynamics of the injection machinery. In particular, we use the following material and geometrical properties for the contracted (stress-free) conformation of the helical strand

$E = 2.3$ GPa, $G = 0.766$ GPa, $\rho = 1380$ kg/m^3, $d = 10$ Å, D $= 330$ Å, $N = 2.01, L = 2115.5$ Å.

and for the capsid/neck/tail tube assembly (rigid cylinder)

$p = 210$ Å, $m_s = 10^{-15}$ kg/m, $m_c = 2.3 \times 10^{-20}$kg, $r_c = 325$ Å,

where p is the helical strand pitch and r_c denotes the cylinder radius.

As described before, the contracted helical strand, which is assumed stress-free, has about two turns (N=2.01), while the extended helical strand, whose strain energy powers the injection process, has about one turn (N=1.05). The simulation begins with initial conditions for the strand at rest in the contracted conformation which also defines the intrinsic curvature/twist vector $\boldsymbol{\kappa_0}$ in equation (2.5) (a helix with 2.05 turns, diameter 330Å, and pitch 210Å). The normalized internal force and moment of strand in the initial (extended) state are $\bar{f}_{e3}^{A} = 170$ and $\bar{q}_{e3}^{A} = -14$, respectively, from Equations (2.7)-(2.10).

Inferring from cryo-EM images, the tail assembly must simultaneously twist counterclockwise (about one turn) and translate downward in achieving the contracted conformation and, due to the nanoscale hydrodynamics, this injection process is expected to be overdamped [41]. The simulation yields the trajectory and associated energetics of the helical strand and the capsid/neck/tail tube assembly. In particular, to compute the system kinetic energy, we add the kinetic energies of translation and rotation of the capsid/neck/tail tube assembly to that of the helical strand given by equation (2.13). The energetics of the entire injection process is illustrated in Figure 2.4 for the case of unrealistically small drag coefficients $\bar{C}_t = 160$ and $\bar{C}_r = 0.2$ which yield an underdamped response as evidenced by the decaying oscillations about the contracted conformation. Increasing the drag coefficients to $\bar{C}_t = 285$ and $\bar{C}_r = 1.8$ yields the expected overdamped response illustrated in Figure 2.5(a) where the extended conformation rapidly collapses to the contracted conformation. From Figure 2.5(a), the time scale of the injection

process is on the order of 700 ns. For comparison, the initial collapse of a highly buckled small portion of DNA in the virus $\varphi 29$ is estimated to be 30-45 ns as reported in [37] using an analogous model.

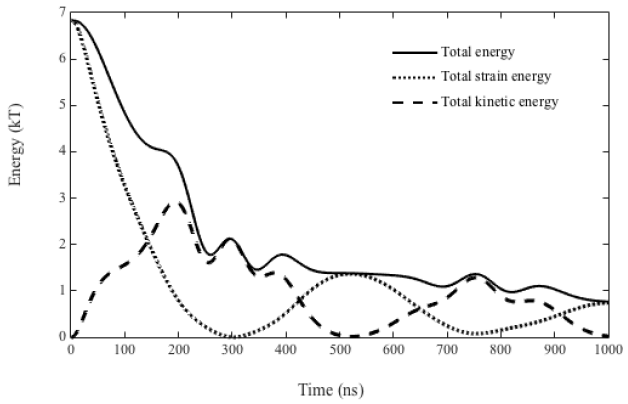

Figure 2.4: Energetics of rapid collapse from extended conformation to contracted conformation. Kinetic, strain, and total energy (kT) are plotted versus time (ns). Unrealistically small drag coefficients yield the underdamped response.

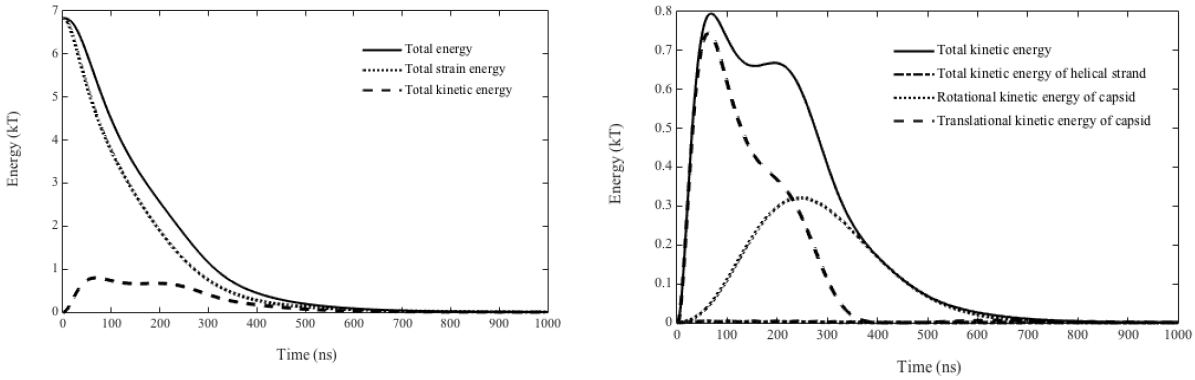

Figure 2.5: (a) Energetics of rapid collapse from extended conformation to contracted conformation. Increased drag coefficients yield the expected overdamped response. (b) Comparison of kinetic energies for helical strand and capsid/neck/tail tube assembly.

Importantly, the energy computations reveal that the strain energy of the extended conformation, about 7 kT, powers the rapid collapse of the sheath and the associated injection of the tail tube needed for infection. For comparison, this energy is significantly less than that (100 kT) required to buckle the small (90bp) portion of DNA as reported in [37]. However, the computed energy for a single helical strand is certainly a lower bound estimate to that stored in the complete six-stranded sheath. The time-varying kinetic energy of the helical strand and the capsid/neck/tail tube assembly is presented in Figure 2.5(b) and it represents approximately 10% of the total energy (Figure 2.5(a)), a small but non-negligible contribution. Note that the capsid is massive in comparison to the helical strand and therefore dominates the kinetic energy of the entire injection machinery. Figure 2.5(b) further exposes the relative contribution of the rotational and translational kinetic energies of the capsid/neck/tail tube assembly. The rotational kinetic energy lags that due to translation and has a maximum about half as large as that due to translation.

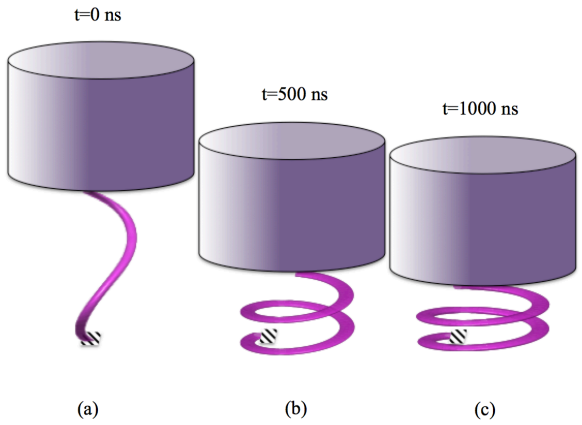

Figure 2.6: Snapshots of the helical strand during the rapid collapse in the injection process: (a) extended conformation, (b) intermediate conformation, and (c) contracted (stress-free) conformation.

2.3 Conclusions

This chapter contributes an approximate model of the injection machinery dynamics by coupling a nonlinear model of a single elastic helical protein strand to a rigid body model of the capsid/neck/tail tube assembly subject to hydrodynamic drag. The helical strand is modeled as a Kirchhoff rod that captures the large conformational change of the sheath from its extended state prior to injection to its contracted state following injection. The rod couples to the (relatively massive) capsid/neck/tail tube assembly at one boundary and the resulting nonlinear initial-boundary value problem is solved using finite differencing (generalized-α method in space and time). Numerical solutions reveal an expected rapid and overdamped collapse from the extended to the contracted state during injection. Simulations further reveal that this process occurs in approximately 700 ns, is powered by 7kT of elastic energy stored in the helical strand and induces the coupled translation and rotation of the tail tube needed to penetrate a host bacterium. Note however that the complete sheath is substantially stiffer as it consists of six interacting helical strands instead of the single helical strand included in this first model and thus the time scale reported here is quite approximate. Moreover, the present model ignores many of the dissipation mechanisms that are enumerated and separately modeled in Chapter 4. The dissipation mechanisms have a profound influence on the time scale of the injection process as discussed in Chapter 5. Nevertheless, this foundational model for a single strand underlies the extensions described in the follow-on chapters, including the extension in Chapter 3 that incorporates all six interacting strands that constitute the complete sheath.

Chapter 3

Model of the phage T4 sheath as six helical protein strands

This chapter is adopted from the publication:

Maghsoodi, A., Chatterjee, A., Andricioaei, I., and Perkins, N. C. (2017). Dynamic model exposes the energetics and dynamics of the injection machinery for bacteriophage T4. Biophysical journal, 113(1), 195-205.

While the atomic structure and protein composition of T4 has been studied extensively by cryo-EM (cryo-electron microscopy) and X-Ray crystallography (see, for example, [15–18]), there is little known about the dynamics of the sheath contraction driving the injection process. Arisaka et al. [25] estimated the enthalpy of sheath contraction to be approximately 3400 kcal/mol gp18 for urea-induced contraction and approximately 6000 kcal/mol gp18 for heat-induced contraction. Falk and James [31] employed elasticity theory to estimate the free energy of the sheath during contraction as well as a lower-bound estimate (103 pN) of the cell rupture force. Extending beyond these studies, this chapter contributes the first predictions of the dynamic behavior of the T4 injection machinery by extending from the rod model proposed in Chapter 2 for a single-strand injection machinery.

The approach begins with an atomistic (Molecular dynamic (MD)) model of a fraction of the sheath that is sufficient to estimate its elastic properties. Those properties are employed in a companion continuum model of the entire sheath that also couples to a model of the capsid and tail tube assembly. The six-stranded sheath is represented by six interacting helical strands modeled by Kirchhoff rod theory as described in Chapter 2 for a single helical strand. The resulting model of the entire T4 injection machine predicts the nonlinear and rapid dynamic conformational changes induced during the injection process. Doing so exposes the energetics, time scale, and pathway of these dynamical changes as well as the available force for piercing the cell membrane. In Section 1, we describe MD simulation to estimate the elastic stiffness of sheath strands and the continuum model (rod model) to simulate the six-stranded sheath. In Section 2, we employ the resulting procedure to simulate the phage T4 injection machinery and highlight important results regarding the energetics, dynamics and the approximate time scale of the injection process. We close in Section 3 with conclusions and comments. This chapter draws largely from our recent publication [42].

3.1 Methods

We open with a summary of our modeling approach to simulate the dynamics of the T4 injection machinery using a two-stage modeling process which begins with estimating the elastic properties of the sheath strands using atomistic modeling of a small fraction of the sheath.

3.1.1 Stage 1: Estimating the elastic properties of the sheath strands

The cylindrical-like tail sheath consists of six interacting helical strands each of which is composed of 23 gp18 subunits that wind around the cylindrical axis of the sheath. When viewed down the cylindrical axis, the gp18 subunits form 23 hexameric rings. In the extended state, each gp18 subunit interacts with four neighboring subunits: the adjacent two subunits within the strand (intra-strand interaction) and the adjacent two subunits within a ring (inter-strand interaction) [18]. Cryo-EM maps [18] reveal that, during sheath contraction, the inter-strand interactions break while the intra-strand interactions remain in retaining the structural integrity of the sheath. The subunits, which are essentially rigid, slide relative to each other during contraction and form new contacts with adjacent subunits. In the fully contracted state, there is a four-fold increase in the number of subunit contacts relative to the extended state, and the number and types of residues involved in all contacts are known; refer to [18] for more details. Despite this wealth of structural information, the elastic properties of the strands are not known, yet they play a central role in powering the dynamic contraction of the sheath. In this first modeling stage, we estimate the elastic bending and torsional stiffness constants for a single strand of the sheath while interacting with its neighboring strands from equilibrium MD simulations. These elastic constants are then incorporated in a continuum model of the entire sheath in the second modeling stage. The MD simulations were performed by our collaborators in the Andricioaei Laboratory (U. C. Irvine) and an overall summary of those simulations and the calculations based on them is provided next. Refer also to [42] for further details.

Prior to estimating the elastic stiffness of the sheath strands, the atomic structure of a single ring of six gp18 molecules is obtained for both the extended and contracted sheath conformations from the protein data bank (PDB ids 3FOH and 3FOI, respectively) [18]. The atomic structure of

five adjacent rings (see Figure 3.1) follows from using a transformation matrix for rotation and translation obtained from [17]. MD simulations with the NAMD package [43] using the CHARMM 36 all-atom force field [44] are then performed with the resultant structures as input. Langevin dynamics applied on the non-hydrogen atoms with a friction coefficient of 5 ps^{-1} is used to generate the trajectory, and a generalized Born implicit solvent continuum model as implemented in NAMD is used to represent the solvent [43]. The system is first slowly heated to an ambient temperature of 298 K, and then equilibrated without any constraints for 5 ns followed by a 20ns production run. In order to avoid any overall rotation or translation of the rings during the simulation, the centers of mass of the proteins of the bottom and top rings are constrained using a harmonic potential with a force constant of 10 kcal mol^{-1} $Å^{-2}$.

The twist and curvature of the subunits is equal to the geometrical torsion and curvature of the (instantaneous) helix passing through the mass centers of the subunits. To compute the twist and curvature of the subunits, a best-fit (least-squares) helix is constructed at each integration time step for each helical strand fragment to deduce its (fluctuating) geometric torsion and curvature. The curvature κ_c, and geometric torsion κ_t, are computed from the pitch and radius of the fitted helix during the 20 ns production run for each of the six strand fragments. The bending stiffness A, and the torsional stiffness C, for each strand are computed from equilibrium fluctuations from the trajectories following the equipartition theorem of classical statistical mechanics

$$\left(\frac{A}{k_B T}\right)^{-1} = \langle (\kappa_c - \langle \kappa_c \rangle)^{tr} (\kappa_c - \langle \kappa_c \rangle) \rangle_{thermal} \tag{3.1}$$

$$\left(\frac{C}{k_B T}\right)^{-1} = \langle (\kappa_t - \langle \kappa_t \rangle)^{tr} (\kappa_t - \langle \kappa_t \rangle) \rangle_{thermal} \tag{3.2}$$

where T is the ambient temperature (298 K), k_B is the Boltzmann constant, and $\langle \quad \rangle$ denotes averaging over time, and $(\quad)^{tr}$ stands for transpose.

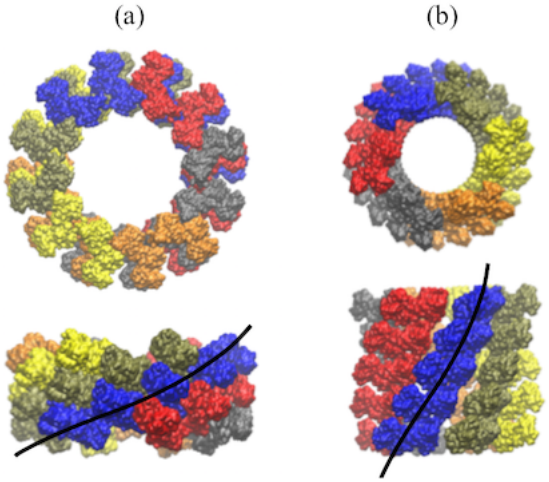

Figure 3.1: Shown here are the five rings of gp18 subunits that form a fraction of the sheath in the contracted (a) and extended (b) conformations. Distinct colors denote distinct helical strands. For reference, the black curve denotes the best-fit helix passing through the mass centers of the subunits in one (blue) strand. Image and results provided by Andricioaei Laboratory (U. C. Irvine).

3.1.2 Stage 2: Modeling the dynamics of the T4 injection machinery

In this second modeling stage, we embed the sheath elastic properties estimated from Stage 1 above in a continuum model of the sheath coupled to a rigid body model for the capsid/neck/tail tube to yield a dynamic model of the entire T4 injection machinery. To this end, we build from an approximate single-strand model of the sheath in Chapter 2 to create a complete shell-like representation of the entire sheath formed by the six interacting helical strands.

3.1.2.1 Modeling the sheath

The sheath consists of six interacting helical strands of gp18 subunits (see in Figure 3.2(a)) which connect to the capsid/neck/tail tube at one end and to the baseplate at another end. To simulate the contractile sheath, we extend the continuum (Kirchhoff rod) modeling approach proposed in Chapter 2 for single-strand sheath to build the shell-like structure of six-strand sheath. In our modeling approach, each helical strand is modeled as a homogeneous and isotropic elastic rod as suggested in Figure 3.2(b). The rationale for constructing a sheath model from six interacting helical rods (strands) follows directly from the experimental evidence that the intra-strand interactions persist throughout the contraction process. The assumptions of homogeneity and isotropy are also supported as further described in Appendix B.

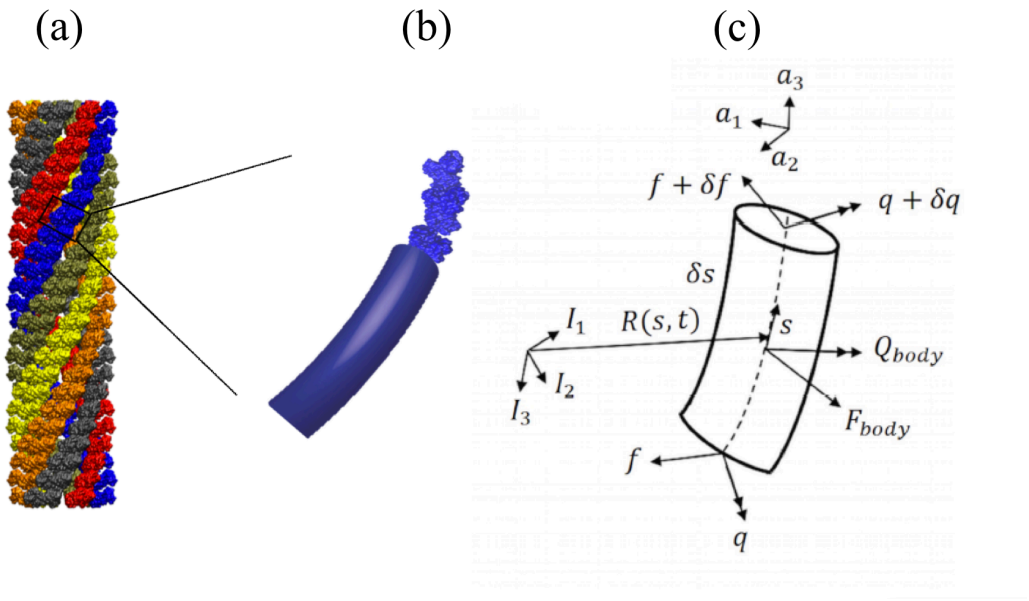

Figure 3.2: (a) The atomistic structure of the T4 sheath consisting six interacting helical strands of gp18 subunits. (b) Representation of each helical protein strand by an elastic rod having equivalent elastic properties. (c) An infinitesimal element of an elastic (Kirchhoff) rod as a continuum model of a helical strand of gp18.

Extending the dynamical equations for a single-strand sheath in Chapter 2 (see equations (2.7)-(2.10)), the governing dynamical equations of the ith strand ($i = 1,2,\dots,6$) in the body-fixed frame $\{a_j^i\}$ are

$$\left\{\frac{\partial \boldsymbol{f}}{\partial s} + \boldsymbol{\kappa} \times \boldsymbol{f} = m_s \left(\frac{\partial \boldsymbol{v}}{\partial t} + \boldsymbol{\omega} \times \boldsymbol{v}\right) - \boldsymbol{F}_{body}\right\}^i, \tag{3.3}$$

$$\left\{\frac{\partial \boldsymbol{q}}{\partial s} + \boldsymbol{\kappa} \times \boldsymbol{q} = \boldsymbol{I_s}\, \frac{\partial \boldsymbol{\omega}}{\partial t} + \boldsymbol{\omega} \times \boldsymbol{I_s}\, \boldsymbol{\omega} + \boldsymbol{f} \times \boldsymbol{a_3} - \boldsymbol{Q}_{body}\right\}^i, \tag{3.4}$$

$$\left\{\frac{\partial \boldsymbol{v}}{\partial s} + \boldsymbol{\kappa} \times \boldsymbol{v} = \boldsymbol{\omega} \times \boldsymbol{a_3}\right\}^i, \tag{3.5}$$

$$\left\{\frac{\partial \boldsymbol{\omega}}{\partial s} + \boldsymbol{\kappa} \times \boldsymbol{\omega} = \frac{\partial \boldsymbol{\kappa}}{\partial t}\right\}^i, \tag{3.6}$$

In equation (3.4), the internal moment $\boldsymbol{q}^i(s,t)$ is proportional to the curvature/twist vector through the assumption of a linear elastic constitutive law

$$\boldsymbol{q^i}(s,t) = \boldsymbol{B^i}(\boldsymbol{\kappa^i} - \boldsymbol{\kappa_0}^i), \tag{3.7}$$

where $\boldsymbol{\kappa_0}^i$ is the known intrinsic curvature/twist vector of the ith helical strand in the stress-free state of the sheath which is assumed to be the contracted conformation. Here, $\boldsymbol{B}^i(s,t)$ is a diagonal 3×3 stiffness tensor

$$\boldsymbol{B^i} = \begin{bmatrix} A & 0 & 0 \\ 0 & A & 0 \\ 0 & 0 & C \end{bmatrix}^{\boldsymbol{i}}. \tag{3.8}$$

for the *i*th strand composed of the bending and torsional stiffness constants estimated from the MD simulations in Stage 1 above. Recall that the MD simulations in Stage 1 consider five rings of the six interacting helical strands. As a result, the reported stiffness properties capture both intra-strand as well as inter-strands interactions. Finally, the vectors $\boldsymbol{F}^i_{body}$ and $\boldsymbol{Q}^i_{body}$ in Equations (3.3)-(3.4) denote the hydrodynamic drag force and moment per unit length on the *i*th sheath strand from the surrounding fluid environment. They are modeled using classical Stoke's regime drag [41]

$$\boldsymbol{F}^i_{body} = -\begin{bmatrix} c_{t1} & 0 & 0 \\ 0 & c_{t2} & 0 \\ 0 & 0 & c_{t3} \end{bmatrix} v^i, \quad \boldsymbol{Q}^i_{body} = -\begin{bmatrix} 0 & 0 & 0 \\ 0 & 0 & 0 \\ 0 & 0 & c_{r3} \end{bmatrix} \omega^i \tag{3.9}$$

where the drag coefficients are [41]

$$c_{t1} = \frac{4\pi\eta}{ln\left(\frac{L}{2R_s}\right) + 0.84}, \qquad c_{t2} = c_{t1}, \quad c_{t3} = \frac{2\pi\eta}{ln\left(\frac{L}{2R_s}\right) - 0.2}, \tag{3.10}$$

$$c_{r3} = 4\pi\eta {R_s}^2.$$

here, R_s=R_s(t) and $L = L(t)$ denote the radius and contour length of each strand (rod), respectively, and η is the viscosity of water. In total, equations (3.3)-(3.6) contain four vector unknowns $\{\boldsymbol{v}, \boldsymbol{\omega}, \boldsymbol{\kappa}, \boldsymbol{f}\}^i$ for each of the six interacting strands yielding a system of 24 nonlinear partial differential equations for solution of the 24 unknowns. This set of equations is discretized in both time and space using the generalized alpha-method that also employs a shooting method to solve the initial-boundary value problem; refer to [35,37] for details on the numerical solution procedure.

Before contraction, the sheath is locked in the extended conformation by noncovalent

interactions in a high-energy structure. While the energy stored by the capsid DNA is also large (DNA is packed to near crystalline density), it does not contribute to the forces that penetrate the host cell as the piercing stage (sheath contraction) precedes the DNA ejection phase for *Myoviridae* phages [45] including T4. Even headless (DNA-free) structures such as R2-pyocin and Type VI secretion system (T6SS) employ contracting sheaths to develop the forces for efficiently piercing the cell membrane. The cell membrane-piercing forces derive from the sudden release of the internal energy stored in the extended sheath during contraction. In our model, the internal sheath energy is represented by the strain energy of the six interacting strands

$$U(t) = \sum_{i=1}^{6} \int_{0}^{L} \frac{1}{2} \left(\boldsymbol{\kappa}^{\boldsymbol{i}} - \boldsymbol{\kappa_0}^{\boldsymbol{i}}\right)^{tr} \boldsymbol{B}^{\boldsymbol{i}} \left(\boldsymbol{\kappa}^{\boldsymbol{i}} - \boldsymbol{\kappa_0}^{\boldsymbol{i}}\right) \mathrm{d}s \tag{3.11}$$

Furthermore (and for future reference), the kinetic energy of the entire injection machine is

$$K(t) = \sum_{i=1}^{6} \int_{0}^{L} \frac{1}{2} \left({\boldsymbol{\omega}^{i}}^{tr} \boldsymbol{I}_s^i \ \boldsymbol{\omega}^{\boldsymbol{i}} + {\boldsymbol{v}^{i}}^{tr} m_s^i \ \boldsymbol{v}^{\boldsymbol{i}} \right) \mathrm{d}s + \frac{1}{2} m_c {v_c}^2 + \frac{1}{2} I_c {\omega_c}^2 \tag{3.12}$$

and it is composed of contributions from the six helical strands (sheath) as well as the rigid body translation and rotation of the capsid/neck/tail assembly modeled next. Therein, m_c and I_c are the mass and moment of inertia (about tail tube axis) of the capsid/neck/tail tube assembly, respectively, and v_c and ω_c are the translational velocity and angular velocity of the capsid/neck/tail tube assembly along and about the tail tube axis, respectively.

3.1.2.2 Modeling the capsid, neck, tail tube, and baseplate via sheath boundary conditions

The sheath strands attach to the baseplate at the lower end and to the capsid/neck/tail tube assembly at the upper end. Upon contraction, the neck and the baseplate expand radially [46], and the locally-bound gp18 subunits of the sheath translate outward along and rotate clockwise about the radial axis perpendicular to the tail tube axis [18]. Simultaneously, the capsid/neck/tail tube assembly rotates counterclockwise about and translates downward along the tail tube axis. These motions of the gp18 subunits that are bound locally to the baseplate and the neck establish the boundary conditions for the sheath helical strands. In particular, the lower boundary of a helical strand (bound to the baseplate) possesses two degrees-of-freedom; namely translation along and rotation about the radial axis. The boundary conditions at the lower end ($\mathrm{s} = 0$), relative to the cylindrical frame $\{e_j^i(s,t)\}$, are given by

$$v_{e1}^i(0,t) = v_r(t)\,, \qquad v_{e2}^i(0,t) = 0\,, \qquad v_{e3}^i(0,t) = 0, \tag{3.13}$$

$$q_{e1}^i(0,t) = 0, \;\; \omega_{e2}^i(0,t) = 0, \qquad \omega_{e3}^i(0,t) = 0\,, \qquad i = 1,2,..,6. \tag{3.14}$$

These conditions describe the facts that, at the lower end, 1) the radial velocity component is prescribed (by the time-varying radius of the neck per (3.19) defined further) while the velocity components in the two orthogonal direction vanish (3.13), and 2) the strand cross section is free to rotate about the radial direction but rotations about the two orthogonal directions vanish (3.14).

By contrast, the upper boundary of a helical strand (bound to the neck) possesses four degrees-of-freedom; namely, translation along and rotation about the radial axis and translation

along and rotation about the tail tube axis. The upper boundary conditions at $s = L(t)$, relative to the cylindrical frame $\{e_j^i(s,t)\}$, are

$$v_{e1}^i(L,t) = v_r(t)\ , \quad v_{e2}^i(L,t) = r_{e1}^i(L,t)\,\omega_{e3}^i(L,t)\ , \tag{3.15}$$

$$\omega_{e2}^i(L,t) = 0\ , \quad q_{e1}^i(L,t) = 0\ , \tag{3.16}$$

$$\sum_{i=1}^{6} f_{e3}^i(L,t) + F_{drag}(t) = m_c \frac{\partial v_c(t)}{\partial t},$$

$$\sum_{i=1}^{6} q_{e3}^i(L,t) + \sum_{i=1}^{6} \left[\boldsymbol{r}^i(L,t) \times \boldsymbol{f}^i(L,t)\right]_{e3} + Q_{drag}(t) = I_c \frac{\partial \omega_c(t)}{\partial t}. \tag{3.17}$$

These conditions describe the facts that, at the upper end, 1) the radial velocity component is prescribed (by the time-varying radius of the neck per (3.19) defined further) while the velocity component in the circumferential direction is determined by the rotation rate of the capsid/neck/tail tube assembly about the tail tube axis (3.15), and 2) the angular rate about the circumferential direction vanishes while the strand cross section is free to rotate about the radial direction (3.16). In addition, (3.17) are the balance laws of linear and angular momentum governing the rigid body motion of the attached capsid/neck/tail tube assembly which translates along the tail tube axis with velocity $v_c(t) = v_{e3}^i(L(t),t)$ and rotates about this axis with angular velocity $\omega_c(t) = \omega_{e3}^i(L(t),t)$. Figure 3.3 illustrates the cylindrical frames $\{e_j^i(s,t)\}$ at the upper and lower boundaries as well as the time-varying radius of the baseplate $r^i(0,t)$ and neck $r^i(L^i(t),t)$.

The motion of the capsid/neck/tail tube assembly (3.17) is substantially influenced by the hydrodynamic drag force and moment from the surrounding fluid environment as given by

$$F_{drag} = -C_t v_c \ , \quad C_t = \frac{2\,\pi\,\eta\,l}{\ln\left(\frac{l}{2R_c}\right)-0.2} \tag{3.18}$$

$$Q_{drag} = -C_r \omega_c \ , \quad C_r = 4\eta\pi l {R_c}^2$$

where, C_t and C_r are the force and moment drag coefficients, respectively. Here, l is the length and R_c is the radius of the (assumed) cylindrical capsid/neck/tail tube assembly which possesses mass m_c and moment of inertia I_c. Finally, the quantities $f^i_{e3}(L,t)$ and $q^i_{e3}(L,t)$ appearing in (3.17) are the reaction force and moment components of ith strand, respectively, at the neck along the e_3 direction.

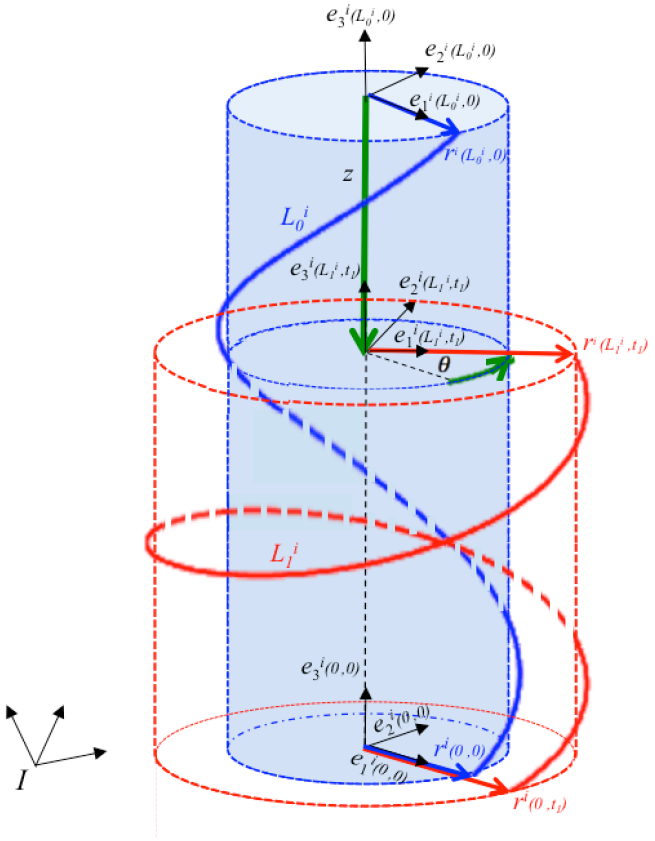

Figure 3.3: Schematic of a single strand in the extended conformation at $t = 0$ (blue helix) and in an intermediate state at $t = t_1$ (red helix). Frame $\{e_j^i(s,t)\}$ denotes a cylindrical frame having radial, circumferential and vertical unit directions (e_1, e_2, e_3) which may vary with contour length s and time t. At the lower boundary, the cylindrical frame remains constant and is denoted $\{e_j^i(0,0)\}$; at the upper boundary, the cylindrical frame varies with time and with time-varying contour length and is denoted $\{e_j^i(L^i(t),t)\}$. Also illustrated are the radius of the baseplate $r^i(0,t)$, the radius of the neck $r^i(L^i(t),t)$, and the strand contour length in the extended conformation L_0^i and in the intermediate state L_1^i. Finally, z and θ denote the translation and rotation of the capsid/neck/tail tube assembly along and about the tail tube axis (e_3), respectively.

3.1.2.3 Initial conditions and configuration-dependent helical strand properties

The simulation of the dynamic injection process begins with the sheath at rest in its extended state which serves as the initial conditions for the subsequent numerical integration. The dynamics of the injection is powered by the internal (strain) energy stored in the extended sheath which forms essentially six interacting nonlinear springs (helical strands) that drive the rigid capsid/neck/tail tube assembly downward along the tail tube axis while permitting it to rotate about that axis, per the boundary conditions at the upper end of the strands described above. During this process, the collar and baseplate also undergo known conformational changes that move the upper and lower boundaries of the helical strands radially outward. Similarly, the helical strands increase in length and the elastic constants increase as previously noted above. We model these dynamic/configuration-dependent changes in any helical strand property $P(t)$ in the simulation by employing the linear interpolation

$$P(t) = P_e + (P_c - P_e)\left(\frac{\theta(t)}{345.4^o}\right) \tag{3.19}$$

where $P(t)$ represents any time-varying strand parameter (i.e., radial position of upper and lower strand boundaries, strand radius, strand contour length, strand bending stiffness, strand torsional stiffness) and with P_e and P_c denoting the known values of the parameter in the extended and contracted conformations, respectively. Here $\theta(t)$ denotes the instantaneous rotation of the rigid capsid/neck/tail tube assembly which begins at zero in the extended state, $\theta_e = \theta(0) = 0$, and achieves its maximum value, $\theta_c = 345.4$ degrees, in the contracted state. Finally, note that the six-fold symmetry of the sheath structure renders all strand properties identical for the six rods.

3.2 Results and discussion

3.2.1 Elastic properties of the sheath strands

Here we report the elastic properties of the sheath provided by our collaborators in the Andricioaei group at the University of California at Irvine. The MD simulations described above yielded estimates of the averaged bending and torsional stiffness constants of the sheath strands in Table 3.1. Values are reported for both the extended and contracted sheath conformations together with published values for actin filaments for comparison. Recognizing the six-fold symmetry of the sheath structure, the elastic properties calculated for any one strand represents the average for all strands. Since the MD model captures the interactions of five rings of six interacting strands, the reported stiffness constants capture both the inter-strand and the intra-strand contributions to the overall sheath stiffness. The estimated bending and torsional stiffness constants of the sheath strands are on the order of those for actin filaments as reported in [47,48]. Note that the elastic bending and torsional stiffness constants in the contracted conformation are significantly greater than those for the extended conformation. That finding is consistent with the aforementioned cyro-EM data showing a four-fold increase in subunit contacts in the contracted conformation [18]. In Figure 3.4, the twist and curvature of the best-fit helices (averaged over all six helical strands) are plotted versus time for both the extended and contracted conformations. The amplitudes of the equilibrium fluctuations associated with the extended strands are significantly greater than those for the contracted strands, confirming that the latter are significantly stiffer. Atomistic RMSD (RMS Deviation) fluctuations from the initial structures, calculated for each of the individual six strands, show only small variations of about 2-4 Å from strand to strand; see further details in the

Appendix C. Therefore, the stiffness values (averaged over all strands) we employ in the dynamic continuum model remain very representative of the values for any strand.

Note, the ring monomer gp18 in the available structures is missing the vital inner C-terminal domain. Therefore, the stiffness constants reported in Table 3.1 are the first estimation of bending and torsional stiffness in the absence of inner domain C for gp18.

Table 3.1: Elastic bending and torsional stiffness constants of the sheath strands for phage T4 in both the extended and contracted conformations. Published values for actin filaments [47,48] shown for comparison. Results provided by Andricioaei Laboratory (U. C. Irvine).

Strand type	Bending stiffness ($10^{-27}\mathrm{N.m^2}$)	Torsional stiffness ($10^{-27}\mathrm{N.m^2}$)
Extended sheath, gp18	26	6.56
Contracted sheath, gp18	35.5	222
Actin filament	73.0±4.38 [48]	80.0±1.20 [47]

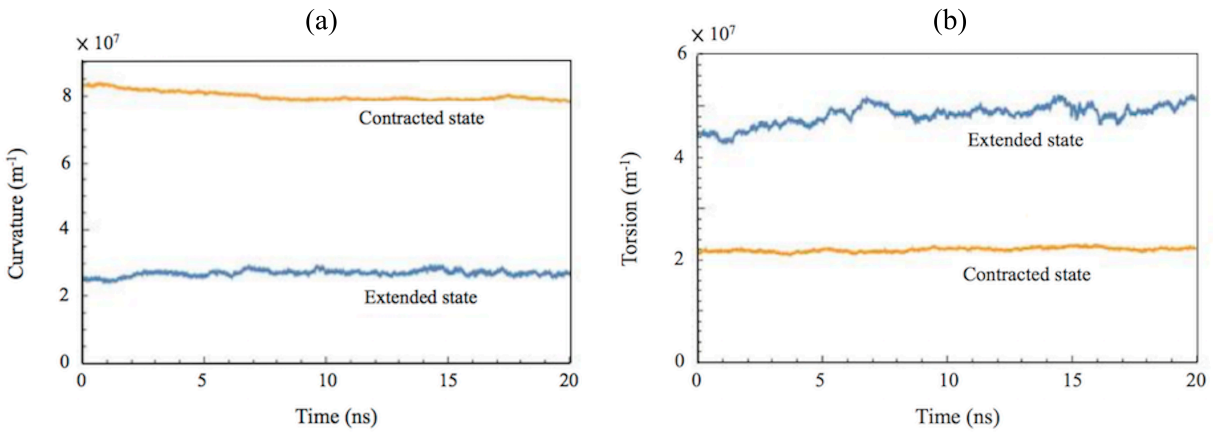

Figure 3.4: Shown here are fluctuations of (a) the average curvature and (b) the average twist for the extended and contracted states during the 20 ns simulation. Results provided by Andricioaei Laboratory (U. C. Irvine).

3.2.2 Time scale and pathway of sheath contraction

The bending and torsional stiffness constants from the MD simulations are used as input to the course-grain model of the sheath composed of six interacting helical strands where each strand is modeled as a homogenous, isotropic elastic rod but with time-varying (configuration-dependent) elastic constants defined by Equation (3.19). The resulting continuum model for the sheath captures the highly nonlinear and rapid dynamic transition from the extended conformation to the contracted conformation. The geometrical and material properties of sheath strands and capsid used in the simulation are provided in the Appendix D. Figure 3.5(a) illustrates computed snapshots of the entire T4 injection machinery at 1 μs time increments during the rapid contraction of the sheath during the simulated injection process. Figure 3.5(b) illustrates the associated rotation and translation of the capsid/neck/tail tube assembly as functions of time. This figure reveals that the injection process is estimated to occur on a time scale of several micro-seconds as mediated by the large drag dominated by the motion of the capsid. This estimated injection time is significantly

shorter than that of the subsequent ejection of the viral DNA from the capsid which is on the order of a minute (about 30s) [49]. Note that the current model ignores 1) the possible dynamic friction between the tail tube and the sheath, 2) any internal (material) damping of the sheath, and 3) any friction (drag) between the tail tube and the cell membrane during the injection process. These additional friction mechanisms, discussed in detail in the Chapter 4, dissipate energy and thus increase the time scale of the injection process relative to the results reported in this chapter.

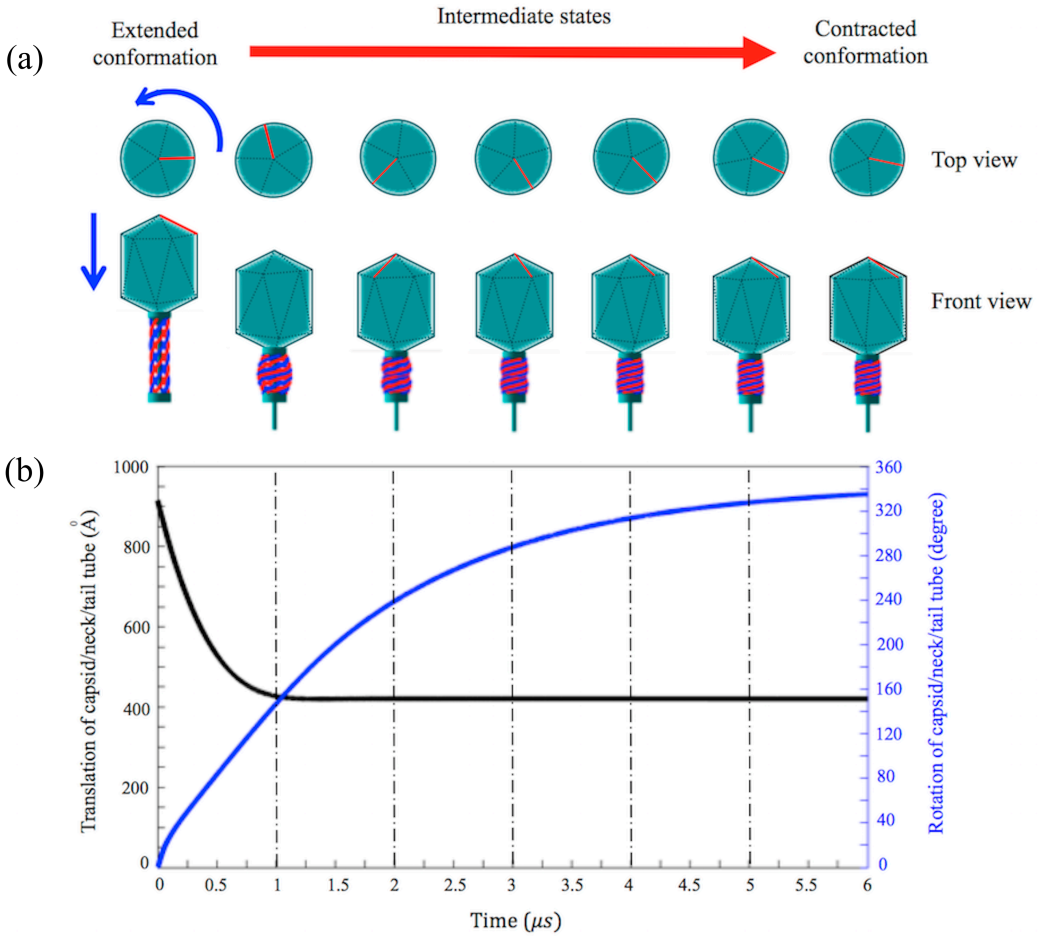

Figure 3.5: Complete sheath model of the T4 injection machinery predicts the dynamic pathway and an approximate time scale of the injection process. (a) Snapshots of T4 at $1\mu s$ intervals reveal the dynamics of sheath contraction and associated rotation. (b) Dynamic rotation (blue curve) and translation (black curve) of the capsid/neck/tail tube assembly.

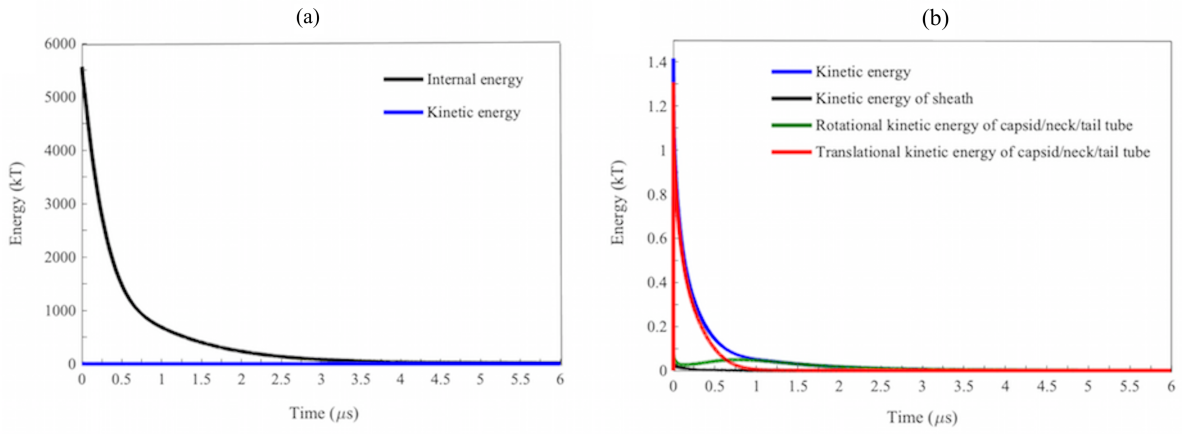

Figure 3.6: Complete sheath model of the T4 injection machinery predicts the energetics of the injection process. (a) Internal (strain) and kinetic energies during the injection process as the sheath rapidly collapses from the extended (high energy) conformation to the contracted (low energy) conformation. (b) Decomposition of kinetic energy into contributions from the sheath and the capsid/DNA/neck/tail tube assembly.

During injection, the capsid/neck/tail tube assembly rotates counterclockwise approximately one revolution and translates downward approximately 500 Å consistent with cryo-EM data for the extended and contracted conformations. The simulation also reveals that the sheath initially undergoes a rapid translation, lasting approximately 1 μs, which brings the end of the tail tube to the cell surface. Following this initial burst of translation is a secondary burst of rotation, lasting approximately 5 μs, during which the capsid/neck/tail tube assembly completes one revolution. While the interaction of the host membrane is not yet considered in this model, it is likely that this two-stage translation and rotation yields the significant force and torque needed to pierce the host membrane. During sheath contraction, all of the strands exhibit the same deformation as they are subject to the identical boundary conditions at the upper end (neck) and the lower end (baseplate).

Thus, the sheath also retains six-fold symmetry during this transition. We also note that the present model predicts that the sheath develops a slight bulge at the very start of the injection process. While no experimental evidence yet exists, we believe that this bulge is artificial and likely derives from the approximate treatment of the time-varying strand parameters discussed above. However, this effect remains rather small and it does not influence either the time scale or the pathway illustrated.

3.2.3 Energetics of sheath contraction

The dynamic model of the T4 injection machinery can estimate the energetics of the injection process by employing the expressions for the internal (Equation (3.11)) and kinetic (Equation (3.12)) energies. Figure 3.6(a) reports the estimated internal (strain) energy driving the rapid and irreversible injection process. Starting at $t = 0$, the injection process is driven by an estimated 5500 kT sheath internal energy which is on the order of the experimentally estimated free energy of sheath contraction reported in [25]. In particular, the enthalpy of contraction for phage T4 reported in [25] is about 5800 kT (3400 kcal/mol gp18) for urea-induced contraction and about 10,000 kT (6000 kcal/mol gp18) for heat-induced contraction. The current model ignores possible interactions between the sheath and the tail tube, and considering such sheath-tail tube interactions may further increase the energy of the extended state (as well as possibly introducing dynamic friction between the tail tube and the sheath during contraction). In addition, the maximum force available to rupture the cell membrane is readily computed from Equations (3.3)-(3.6) for the extended sheath. This maximum force estimated from this model is 860 pN which is consistent with the minimum force (lower bound estimate) of 103 pN provided in [31].

During contraction, the sheath and capsid are subject to nanoscale hydrodynamic drag forces and moments from the surrounding fluid environment. The drag force/moment pair on the sheath strands is incorporated in the balance laws for linear (Equation (3.3)) and angular (Equation (3.4)) momentum through the terms $\boldsymbol{F}^{i}_{body}$ and $\boldsymbol{Q}^{i}_{body}$ given by Equations (3.11)-(3.12). The drag force/moment pair on the capsid is captured through the equations of rigid body motion of the capsid/neck/tail tube assembly through the upper boundary conditions on the sheath; refer to Equations (3.17)-(3.18). Due to the overwhelmingly large drag at these length scales, the kinetic energy of the entire injection machinery remains very small relative to the internal energy as reported in Figure 3.6(a). Figure 3.6(b) provides a decomposition of the kinetic energy into contributions from the sheath, and the translational and rotational contributions from the capsid/neck/tail tube assembly. The kinetic energy of the capsid/neck/tail tube assembly dominates the kinetic energy of the sheath. This follows from the fact that the mass of the capsid (and genomic DNA)/neck/tail tube assembly (approximately 200 MDa) is approximately 20 times greater than that of the (six-stranded) sheath (approximately 10 MDa) as estimated from data reported in [11,17].

In Figure 3.6(b), note the comparable translational and rotational components of the kinetic energy of the capsid/neck/tail tube assembly. However, the translational kinetic energy achieves a maximum well within the first 1μs of the injection process whereas the maximum of the rotational kinetic energy is delayed. This delay is consistent with the aforementioned predictions of Figure 3.5 which show that the capsid/neck/tail tube assembly undergoes a significant and rapid translation followed by a significant and rapid rotation. This two-punch combination of translation followed by rotation may play a significant role in the efficient piercing of the host membrane by the tip of the tail tube. Consider the advantage of quickly rotating the tip of the tail tube *after* the

tip contacts the host membrane as an efficient mechanism to rupture the membrane.

3.3 Conclusions

This chapter introduces a dynamic model for phage T4 that incorporates the influence of all six interacting helical strands of the sheath. The model incorporates the nonlinear dynamics of the sheath from its extended conformation prior to injection to its contracted conformation following injection as well as the rigid body translation and rotation of the attached capsid/neck/tail tube domains. As the first step, we estimate the bending and torsional stiffness constants for the helical strands of gp18 that form the elastic sheath from equilibrium MD simulations. Next, we employ the stiffness constants in a continuum model of the elastic sheath composed of six interacting helical strands of gp18 by representing each strand as a homogenous, isotropic elastic rod with time-varying elastic constants. The rigid body motion of the attached capsid/neck/tail tube assembly is captured through a boundary condition for the helical strands and it models the assembly as it translates along and rotates about the tail tube axis.

The resulting dynamic model for the entire injection machinery is used to estimate the energetics, time scales and pathway of the T4 injection process as well as the maximum available force for cell rupture. Simulation results predict that the injection process is powered by approximately 5500 kT of internal (strain) energy stored in the extended conformation of the sheath, that injection of the tail tube into the host is completed in approximately 6 μs, and that the extended sheath provides a maximum force of 860 pN to pierce the host.

We note however several limitations in the dynamic model proposed in this chapter. First,

this model does not capture the wave propagation mechanism of sheath contraction observed in experiments [28,30] because we have assumed that the sheath strands possess *homogenous* elastic stiffness during contraction. Second, the MD-derived elastic constants reported in Table 3.1 follow from an incomplete model for the gp18 subunits where the inner domain is missing. This leads to elastic constants that are smaller than expected. Third, we have ignored the retarding influences from additional energy dissipation mechanisms within T4 as well as the interactions of T4 with the host cell. Accordingly, the results in this chapter provide rough estimates of the dynamics of the phage T4 injection machinery. We address each of these limitations in the subsequent chapters beginning with the additional sources of energy dissipation in Chapter 4.

Chapter 4

Modeling energy dissipation for the phage T4 injection machinery

The portion of this chapter concerning internal friction of the sheath strands is adopted from the publication:

Maghsoodi, A., and Perkins, N. (2018). Shear deformation dissipates energy in biofilaments. Scientific reports, 8(1), 11684.

The prior models of the phage T4 injection machinery (Chapters 2 and 3) ignore dissipation from all sources except for the hydrodynamic drag acting on the capsid and sheath. This chapter provides an overview and approximate models for all sources of dissipation that include: 1) the hydrodynamic drag on the capsid and sheath, 2) the tail tube-cell interaction both prior to and following the rupture of the host cell membrane, 3) the sheath-tube friction during sheath contraction, and 4) internal (material) dissipation of sheath strands during large conformational changes during contraction. This chapter summarizes approximate models for all four sources of dissipation in order to further understand their influences on the dynamics and energetics of the injection process in a system-level model as revealed in Chapter 5.

4.1 Hydrodynamic drag on capsid and sheath

During contraction, the sheath and capsid are subject to nanoscale hydrodynamic drag forces and moments from the surrounding fluid environment which are modeled using classical Stoke's regime drag through (3.9) for the sheath strands and (3.18) for the capsid as proposed in Chapter 3. For review, we recall these approximations here. The hydrodynamic drag force and moment from the surrounding fluid environment on capsid are given by [41]

$$F_{drag} = -C_t v_c \ , \quad C_t = \frac{2\,\pi\,\eta\,l}{\ln\left(\frac{l}{2R_c}\right)-0.2} \tag{4.1}$$

$$Q_{drag} = -C_r \omega_c \ , \quad C_r = 4\eta\pi l {R_c}^2$$

where, C_t and C_r are the force and moment drag coefficients, respectively. Here, η is the viscosity of bulk water, and l is the length and R_c is the radius of the (assumed) cylindrical capsid/neck/tail tube assembly. The drag force/moment pair on the capsid is incorporated in the upper boundary conditions of sheath strands given by (3.17).

The hydrodynamic drag force and moment per unit length on the *i*th sheath strand from the surrounding fluid environment are given by [41]

$$\boldsymbol{F}^i_{body} = -\begin{bmatrix} c_{t1} & 0 & 0 \\ 0 & c_{t2} & 0 \\ 0 & 0 & c_{t3} \end{bmatrix} v^i, \quad \boldsymbol{Q}^i_{body} = -\begin{bmatrix} 0 & 0 & 0 \\ 0 & 0 & 0 \\ 0 & 0 & c_{r3} \end{bmatrix} \omega^i \tag{4.2}$$

where the drag coefficients are

$$c_{t1} = \frac{4\pi\eta}{ln\left(\frac{L}{2R_s}\right) + 0.84}, \qquad c_{t2} = c_{t1}, \quad c_{t3} = \frac{2\pi\eta}{ln\left(\frac{L}{2R_s}\right) - 0.2}, \tag{4.3}$$

$$c_{r3} = 4\pi\eta {R_s}^2.$$

Here, R_s=R_s(t) and $L = L(t)$ denote the radius and contour length of each strand, respectively, and η is the viscosity of bulk water. The drag force/moment pair on the sheath strands is incorporated in the balance laws for linear (Equation (3.3)) and angular (Equation (3.4)) momentum through the terms $\boldsymbol{F}^i_{body}$ and $\boldsymbol{Q}^i_{body}$ given by (4.2).

4.2 Cell-tail tube dissipation and interactions

The gram-negative bacterial cell envelope is a complex structure consisting of three main domains; the outer membrane, the periplasmic space, and the inner membrane (also known as plasma membrane or cytoplasmic membrane); see Figure 4.1 [50]. During sheath contraction, the tail tube simultaneously rotates and translates downward to pierce and enter this envelope. Assuming the tip of the tail tube touches the outer membrane say at time t_1, the tip then applies a mechanical load to the outer membrane causing it to deform locally. When the tip of the tail tube ruptures the outer membrane say at time t_2, it then translates through the periplasmic space. During this entire process, the cell applies a two-stage reaction force and moment on the tip of the tube in the forms of: 1) a coupled indentation reaction force and moment before rupturing the outer membrane (for $t_1 < t < t_2$), and 2) a coupled hydrodynamic drag force and moment from the viscous layers of the periplasmic space until the end of sheath contraction, say from $t_2 < t < t_3$, where t_3 denotes the end of sheath contraction. Note that the tip of the tail tube does not penetrate the inner

membrane.

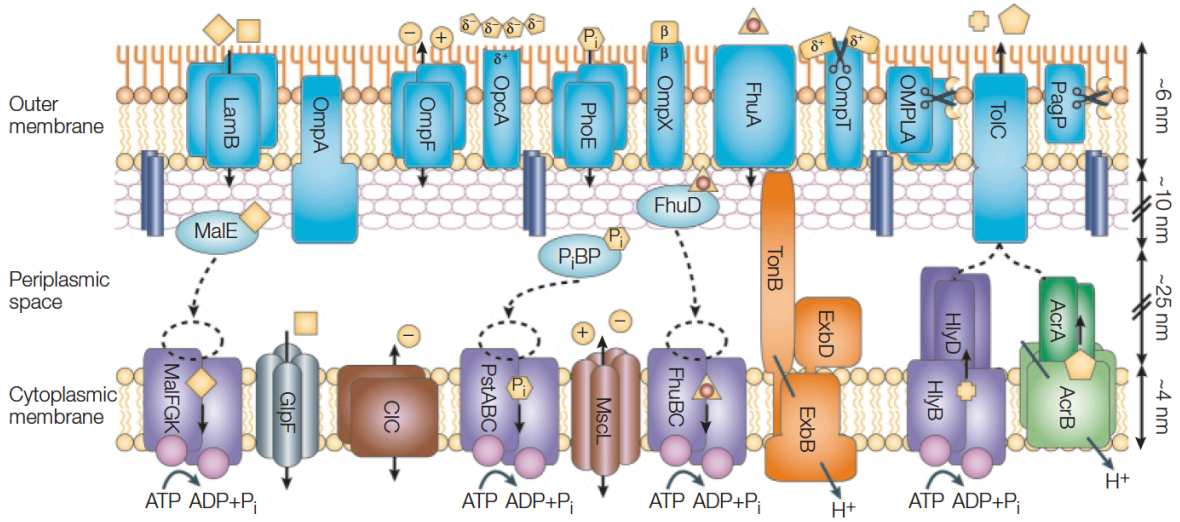

Figure 4.1: Schematic of gram-negative cell membrane consisting of three main domains; the outer membrane, the periplasmic space, and the cytoplasmic membrane [51].

We begin by proposing an approximate model describing the indentation of the outer membrane by the tip of the tail tube. It has been established that bacterial cell membranes possess viscoelastic material properties [52,53] during indentation. To simulate the viscoelastic behavior of the outer cell membrane, we adopt the dynamic viscoelastic model proposed in [52]. As illustrated in Figure 4.2, the model consists of an elastic spring with stiffness k_1 (governing instantaneous deformation) in series with the parallel spring and dashpot with stiffness k_2 and damping coefficient D_c, respectively, (governing the delayed deformation of the outer membrane). The coordinate $z(t)$ defines the indentation depth of the tip of the tail tube. In this model, force balances at points A and B (see Figure 4.2) yield

$$k_1 x_1(t) = F_{ind}(t), \quad \text{at point A} \tag{4.4}$$

$$k_2 x_2(t) + D_c\, \dot{x}_2(t) - F_{ind}(t) = 0, \quad \text{at point B} \tag{4.5}$$

where

$$x_1(t) + x_2(t) = z(t) \tag{4.6}$$

and $F_{ind}(t)$ is the indentation force from the tube on the outer membrane. Combining equations (4.4)-(4.6) yields

$$\frac{\mathrm{d}F_{ind}(t)}{\mathrm{d}t} + F_{ind}(t)\left(\frac{k_1 + k_2}{D_c}\right) - k_1 \frac{\mathrm{d}z(t)}{\mathrm{d}t} - \left(\frac{k_1 k_2}{D_c}\right)\mathrm{z(t)} = 0, \qquad t = [t_1, t_2] \tag{4.7}$$

Note that $\mathrm{z}(\mathrm{t}_1)$=0 when the tail tube touches the cell membrane. Since the tail tube is (assumed) rigidly connected to the capsid and thus the upper end of sheath strands, the indentation displacement $z(t)$ and velocity $\frac{\mathrm{d}z(t)}{\mathrm{d}t}$ in (4.7) are equal to displacement and linear velocity of the capsid along the tube axis. Numerical solution of (4.7) yields the indentation force F_{ind} which decelerates the sheath contraction during the time interval $t = [t_1, t_2]$. To incorporate this effect in the model of the injection machine, the force F_{ind} is added to (3.17) that defines the upper boundary condition for the sheath. While we also suspect there may be a reaction torque from the outer membrane on the tail tube, that we are ignoring this potential effect for lack of any present information concerning the torsional stiffness of the membrane (a component of the in-plane stiffness). Should future research reveal the torsional stiffness, its influence could be readily

incorporated into the model of the injection machine through the boundary condition (3.17) governing the rotation of the tail tube/capsid assembly about the tail tube axis.

After rupturing the outer membrane, the tip of the tail tube is immediately subject to the hydrodynamic drag from the periplasmic space for the time interval $t_2 < t < t_3$. To this end, the hydrodynamic drag and moment on the tail tube is modeled by Stoke's equation

$$\mathrm{F}_{drag} = -C_d(t)\, v(L,t), \quad Q_{drag} = -D_d(t)\, \omega(L,t), \quad t = [t_2, t_3]. \tag{4.8}$$

Note that $v(L,t)$ and $\omega(L,t)$ are the linear velocity and angular velocity of tube computed from the upper end of sheath strands (at $s = L$). The drag coefficients C_d and D_d are calculated from linear interpolation of these parameters between time t_2 and t_3, where

$$C_d(t_2) = D_d(t_2) \approx 0, \tag{4.9}$$

$$C_d(t_3) \approx \frac{2\pi\eta_c}{ln\left(\frac{L_t}{2R_t}\right) - 0.2}, \qquad D_d(t_3) \approx 4\pi {R_t}^2\, \eta_c$$

in which η_c is the average viscosity of outer membrane and periplasmic space, R_t is the radius of the tube inside the cell, L_t is the length of tube inside the cell after full contraction of sheath.

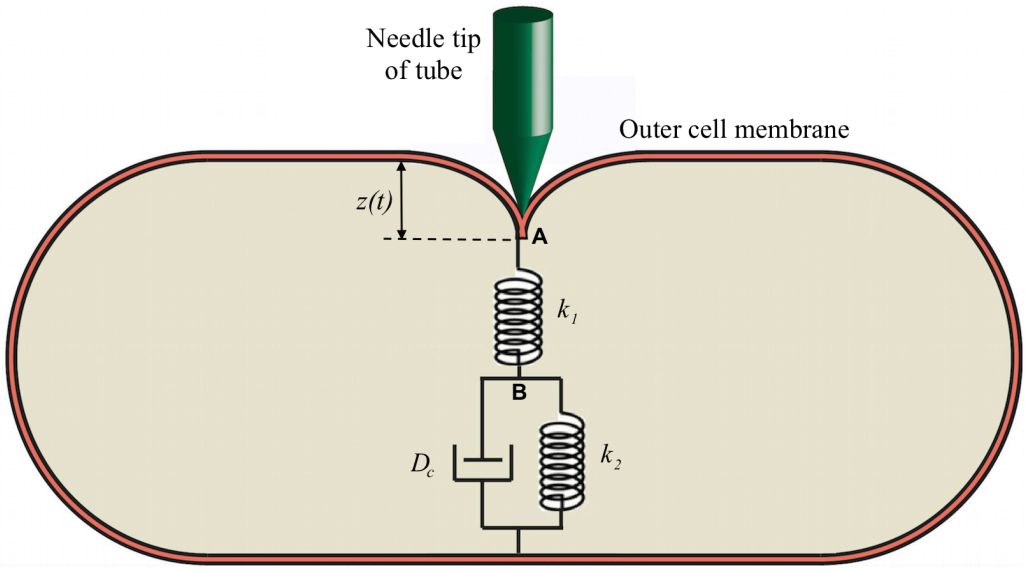

Figure 4.2: Schematic of tail tube-cell interaction before rupturing the out membrane of the cell. The viscoelastic behavior of the outer cell membrane is modeled by an elastic spring with stiffness k_1 for instantaneous deformation in series with the parallel spring and dashpot with stiffness k_2 and damping coefficient D_c, respectively, for delayed deformation of membrane [52].

4.3 Sheath-tail tube interaction

Despite the wealth of information on the atomic structure of the sheath and the tail tube, possible interactions between them remain largely unknown. Potential sheath-tube interactions may arise from electrostatic and non-bonded forces and viscosity in the nano-scale gap (interstitial water) between the tail tube and the surrounding sheath. Importantly, these interactions might retard the injection process thereby affecting the time-scale of this process.

To understand the sheath-tail tube interactions, we begin by reporting the surface Coulomb potential distribution and the Kyte-Doolittle hydrophobicity for the tail tube, the extended sheath, and the contracted sheath. The atomic structure of the lower two rings of the tail tube are extracted

from the cryo-EM structure of the entire T4 baseplate (pdb id 5IV5), and two additional rings are constructed using the published tail tube helical parameters [24]. The surfaces are generated using UCSF Chimera [54]. As illustrated in Figure 4.3, the inner surface of the extended sheath is largely positively charged at the edges (blue) where it forms complementary charged interactions with the mostly negatively charged (red) outer tail tube surface. However, apart from these edges, the inner sheath surface is equally neutrally, positively and negatively charged. In the contracted conformation, the inner sheath edge is negatively charged, implying that during contraction there is a redistribution of charges along the inner sheath surface. Importantly, these charge distributions along the inner sheath surface for the both extended and contracted conformations and along the outer tube surface are relatively uniform. This implies that the net electrostatic and non-bonded forces remain largely perpendicular to the tube axis and thus contribute insignificant work as the tube translocates through the sheath.

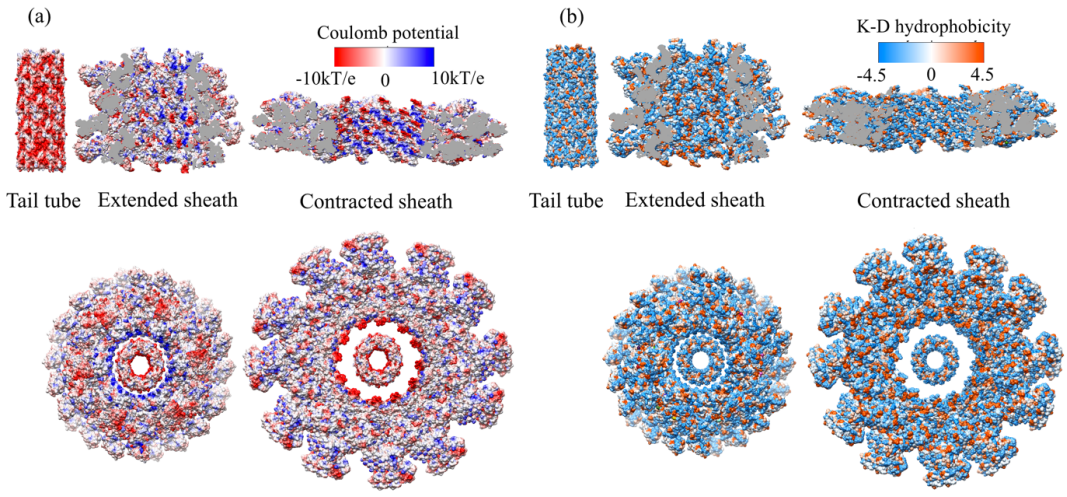

Figure 4.3: (a) Surface coulomb potential distribution of (clockwise) four rings of the outer surface of the tail tube, the inner surface of the extended sheath, and the inner surface of the contracted sheath. Beneath are top views of the tube within the extended sheath and within the contracted sheath. (b) Kyte-Doolittle hydrophobicity [55] of the same surfaces arranged in the same order as in (a). The outer surface of the tail tube and the inner surface of the sheath are largely hydrophilic (blue).

By contrast, a significant interaction may arise during translocation from the viscosity of the interstitial nano-scale gap. However, water confined to this nanoscale gap exhibits distinct viscosity characteristics compared to bulk water and these characteristics strongly depend on the gap thickness and the degree of surface hydrophilicity/hydrophobicity. Experimental studies [56,57], reveal that the greater the affinity between the water molecules and the surfaces forming the nano-scale gap, the greater the effective viscosity. For example, the viscosity of water confined to a 1.3 nm gap between an oxide-terminated tip of an IFM (interfacial force microscopy) and a silica surface is about 6 orders of magnitude greater than the viscosity of bulk water at room temperature (8.6×10^{-4}pa.s) [56]. As illustrated in Figure 4.3, the outer surface of the tail tube and the inner surface of the sheath are largely hydrophilic (blue), indicating that the nano-channel between the tube and sheath is essentially hydrophilic. Accordingly, the viscosity of this interstitial nano-scale gap is expected to be far greater than that of bulk water.

As illustrated in Figure 4.3, the gap between the sheath and the tail tube is nearly zero in the extended state and about 10 Å in the contracted state. To simulate the friction (hydrodynamic drag) between the contracted portion of the sheath and the tube, we employ a classic model of fluid motion between two parallel surfaces with linearly varying velocity profile due to shear both parallel and perpendicular to the (translating and rotating) tail tube; refer to Figure 4.4. Since the tail tube attaches to the upper end of the sheath strands, the tail tube rotates and translates with the same linear (v_t) and angular (ω_t) velocities of the upper end of the sheath, i.e., $v_t(t) = v(L,t)$ and $\omega_t(t)$=$\omega(L,t)$. The linear and angular velocities of the contracted portion of the sheath are almost zero. The resulting friction (viscous) forces and moments from the water molecules on the inner surface of the sheath and the outer surface of tube are given by

$$\mathrm{F}_{tube} = \eta_w \frac{v(L,t)}{d} A_t(\mathrm{t}), \tag{4.10}$$

$$\mathrm{Q}_{tube} = \eta_w \frac{r_t \omega(L,t)}{d} r_t \, A_t(\mathrm{t}) \tag{4.11}$$

where η_w is the effective water viscosity in the nano-scale gap d~10Å, A_t is the wetted area of the tube interacting with the contracted portion of the sheath, r_t is the outer radius of the tube. The frictional force F_{tube} and moment Q_{tube} in (4.10) and (4.11) are applied to the upper boundary condition of sheath strands.

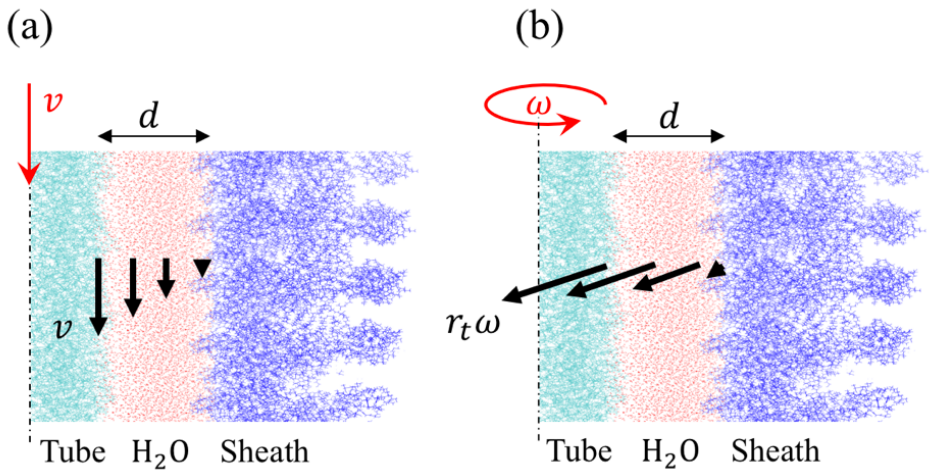

Figure 4.4: Components of the velocity profile of water within the nanoscale gap (d) between the sheath and the tail tube due to (a) translation v, and (b) rotation ω of the tail tube during injection.

4.4 Internal (material) dissipation of sheath strands

During sheath contraction, the strands undergo a nonlinear conformational change from the extended state to the contracted state. During this change, cryo-EM maps reveal that the gp18 subunits within each strand rotate and translate in forming new contacts but with essentially no significant change to their atomic structure. The resulting rearrangement (new contacts) at the subunit level likely introduce internal dissipation at the strand level. Many studies have shown that related biofilaments including microtubules, actin filaments, and chromosomal fragments exhibit internal dissipation associated with conformational changes or fluid flow through internal filament pores in addition to the external dissipation from hydrodynamic drag; see for example [58]. Thus, it stands to the reason that the sheath strands may also exhibit internal friction associated with the above rearrangement of the gp18 subunits during contraction in addition to the external friction from the surrounding fluid. A new theory for that internal friction is derived below by extending the work of [58] and others.

In what follows, we develop a novel model that incorporates the internal viscoelasticity of thermally fluctuating biofilaments due to both bending and shear deformations that arise, for example, during the nonlinear conformational change of the sheath strands. We validate this model using the reported experimental data for chromosomes and microtubules. Second, we employ the proposed energy dissipation model to calculate the internal dissipation of the sheath strands during contraction. We begin by reviewing the literature concerning the internal friction in the broader context of fluctuating biofilaments which is also described in our recent publication [59].

4.4.1 Internal (material) friction in thermally fluctuating biofilaments

Biofilaments including microtubules, DNA, and actin filaments are semiflexible micro-scale polymer structures that perform essential functions in living cells. Understanding the dynamical behavior and the material properties of biofilaments are central to understanding their structure-function relations. A variety of models describe the material stiffness and thermal fluctuations of biofilaments; see, for example, [58,60]. Primary among these is the worm-like chain (WLC) model [61,62] which represents a biofilament as a continuous isotropic rod undergoing dynamic bending while subject to thermal excitation and hydrodynamic drag; see, for example, [63–65]. Poirier and Marko [58] extend the WLC model to account for internal friction due to dynamic bending. Subsequent studies have employed that model to describe the internal dissipation of biofilaments in addition to external friction due to hydrodynamic drag; see, for example, [58,65–67]. However, the WLC model [62] and its extension for bending-induced internal friction [58] are based on classical Euler-Bernoulli theory for beam bending [68] which tacitly assumes that the cross sections of the filament remain planar and perpendicular to the (fluctuating) filament centerline; see Figure 4.5(a). These kinematic assumptions, which remain accurate only for long filaments and long wavelength (small wavenumber) fluctuations, limit the applicability of the WLC model.

However, understanding the dynamics of short biofilaments remains of great interest when one considers the many short-range interactions within the cell achieved through biofilaments as well as biophysical experiments on short biofilaments. For example, short (<10 μm long [69]) microtubules are actively recruited in intracellular transport and cellular mitosis while short (<5 μm long [70]) actin filaments, responsible for cell motility, dominate the distribution of actin. Key measures of biofilament length include the ratio of the filament length to diameter $L/2r$ and

the ratio of the wavelength of dynamic fluctuations to the filament radius λ/r. For short filaments ($L/2r < 10$) [68,71] or short wavelength fluctuations ($\lambda/r < 10$) [68], the effect of shear deformation becomes important relative to bending deformation. At these length scales, the filament exhibits direct shear deformation and the filament cross sections no longer remain perpendicular to the filament centerline (see Figure 4.5(b)) as assumed in the WLC model (see Figure 4.5(a)). This shear effect in biofilaments can be quite pronounced as exposed herein in the context of internal friction.

The effect of shear on the stiffness properties of short biofilaments has previously been observed in [72,73]. For example, Pampaloni et al. [73] measured the persistence length of thermally fluctuating microtubules having lengths from 2.6 to 47.5 μm. Both theory and experiment confirm that the persistence length of short microtubules (shorter than 21 μm) is length-dependent as a consequence of shear deformation. Thus, it stands to reason that shear deformation in thermally fluctuating biofilaments may also significantly affect *dissipation* properties as well. To address this hypothesis, we present a new model for thermally fluctuating biofilaments, based on Timoshenko beam theory, which considers shear deformation as an additional source of elastic deformation and energy dissipation. This model reveals important effects of dynamic shear (above those due to dynamic bending) on both internal and external dissipation mechanisms. Results demonstrate that shear deformation leads to qualitatively new energy dissipation behaviors including dissipation dynamics on two time scales associated with internal friction and on two length scales associated with external friction. These new theoretical predictions successfully describe the experimental trends observable in studies of fluctuating chromosomal fragments [58] and microtubules [67].

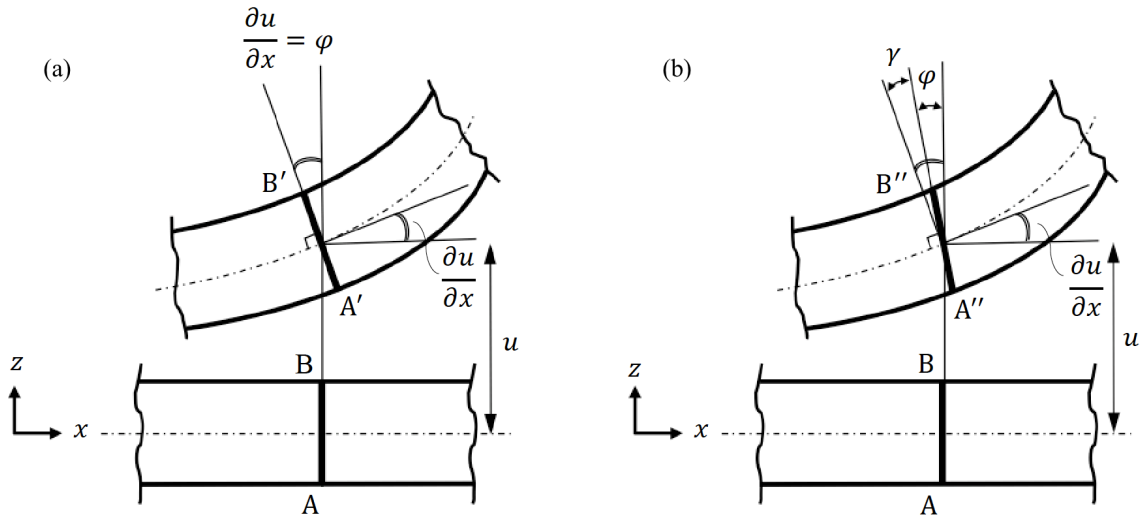

Figure 4.5: Schematic of rod cross section before deformation (bottom) and after deformation (top). The worm-like chain model employs Euler-Bernoulli theory in which the deformed cross section $A'B'$ remains perpendicular to the rod centerline (a). In Timoshenko theory, the deformed cross section $A''B''$ does not remain perpendicular to the rod centerline due to the additional rotation due to shear (b). In particular, φ and γ are the rotations due to bending deformation and shear deformation, respectively, and thus $\frac{\partial u}{\partial x} = \varphi + \gamma$ is the total rotation of the deformed cross section.

4.4.1.1 Methods

We propose a model of energy dissipation for thermally fluctuating biofilaments possessing short lengths ($L/2r < 10$) [68,71] or short wavelength fluctuations ($\lambda/r < 10$) [68] in which shear deformation is not negligible. To this end, we employ Timoshenko beam theory [68] which models the coupled bending-shear deformations of elastic rods. The governing Langevin formulation is

$$B\frac{\partial^2 \varphi}{\partial x^2} + \kappa S\left(\frac{\partial u}{\partial x} - \varphi\right) + \eta_b' I \frac{\partial^3 \varphi}{\partial x^2 \partial t} + \eta_s' A\left(\frac{\partial^2 u}{\partial x \partial t} - \frac{\partial \varphi}{\partial t}\right) = 0 \tag{4.12}$$

$$\kappa S\left(\frac{\partial \varphi}{\partial x}-\frac{\partial^2 u}{\partial x^2}\right)+\eta_s' A\left(\frac{\partial^2 \varphi}{\partial x \partial t}-\frac{\partial^3 u}{\partial x^2 \partial t}\right)+\eta \frac{\partial u}{\partial t}=n(x,t) \tag{4.13}$$

in which $u(x,t)$ denotes the fluctuating transverse displacement of the filament (in directions perpendicular to the filament centerline) due to random thermal excitation $n(x,t)$, x denotes the filament contour length coordinate, and t denotes time. The quantities φ and $\frac{\partial u}{\partial x}-\varphi$ are the components of the rotation of the filament cross section due to bending deformation and shear deformation, respectively. The filament bending stiffness $B = EI$ is composed of the filament's Young's modulus E and area moment of inertia I while the filament shear stiffness $S = GA$ is composed of the filament's shear modulus G and cross sectional area A. The quantity κ denotes the Timoshenko shear correction factor which, for a filament with circular cross section, is κ = 0.75 [68]. Here, η denotes the external hydrodynamic drag coefficient (Stoke's regime), and η_b' and η_s' are the internal dissipation coefficients due to bending and shear deformations, respectively. Consequently, the third and fourth terms in (4.12) and the second term in (4.13) model the internal dissipation due to shear (coefficient η_s') and bending (coefficient η_b'). Consistent with the Langevin formulation, the inertial terms that otherwise appear in Timoshenko theory [68] are neglected. A derivation of (4.12)-(4.13) is included in the Appendix E.

As in prior analyses (e.g., [58]), energy dissipation can be quantified by computing the autocorrelation function for the transverse displacement u for thermal fluctuations assuming ideal (white) thermal noise. To this end, the autocorrelation function $\mathcal{R}(T)$ for u follows from a Fourier transform of (4.12) and (4.13)

$$U_{q\omega} = \int \int u(x,t)\, \mathrm{e}^{i(qx-\omega t)}\, \mathrm{d}x\, \mathrm{d}t \tag{4.14}$$

$$\Phi_{q\omega} = \int \int \varphi(x,t)\, \mathrm{e}^{i(qx-\omega t)}\, \mathrm{d}x\, \mathrm{d}t \tag{4.15}$$

in which $U_{q\omega}$ and $\Phi_{q\omega}$ denote the (double) Fourier transforms of the transverse displacement u and the rotation φ, respectively. The quantities q and ω are the wavenumber and frequency of propagating waves, respectively. The resulting autocorrelation function (derived in the Appendix E) becomes

$$\mathcal{R}(T) = R_1\, \mathrm{e}^{\frac{-T}{\tau_1}} + R_2\, \mathrm{e}^{\frac{-T}{\tau_2}} \tag{4.16}$$

$$\tau_1 = \sqrt{\frac{2\mathrm{M}}{\mathrm{N}+\sqrt{\mathrm{N}^2-4\mathrm{MP}}}},\quad \tau_2 = \sqrt{\frac{2\mathrm{M}}{\mathrm{N}-\sqrt{\mathrm{N}^2-4\mathrm{MP}}}} \tag{4.17}$$

Here τ_1 and τ_2 are *two* distinct energy relaxation times and T is the lag-time. Thus, this result immediately reveals that energy relaxation occurs on the *two* time scales τ_1 and τ_2 that are functions of the wavenumber q, internal viscosities η_b' and η_s', and hydrodynamic drag η through the quantities M, N, and P detailed in the Appendix E.. We discuss these time scales and the effects of shear deformation in detail below.

In the limit of long filaments or long wavelengths, the shear deformation is negligible and the total rotation of the cross section due to bending alone obeys the kinematic constraint $\frac{\partial u}{\partial x} = \varphi$. Upon employing this constraint, the formulation above recovers the single time scale autocorrelation function for the WLC model (based on Euler-Bernoulli beam theory) employed in [58].

$$\mathcal{R}(T) = R\, \mathrm{e}^{\frac{-T}{\tau}} \tag{4.18}$$

$$\tau = \frac{\eta + \eta_b' I q^4}{B q^4} \tag{4.19}$$

For further reference, (4.19) becomes

$$\tau = \frac{\eta}{B q^{*4}} L^4 + \frac{\eta_b' I}{B} \tag{4.20}$$

in which $q^* = qL$ is a non-dimensional wavenumber with L being the filament length.

While the above analysis (4.16)-(4.17) reveals the effects of shear on internal friction, one can perform a parallel analysis to expose the effects of shear on external friction due to hydrodynamic drag alone. In this case ($\eta_s' = \eta_b' = 0$), Equations (4.12) and (4.13) simplify to

$$B \frac{\partial^2 \varphi}{\partial x^2} + \kappa S \left(\frac{\partial u}{\partial x} - \varphi \right) = 0 \tag{4.21}$$

$$\kappa S \left(\frac{\partial \varphi}{\partial x} - \frac{\partial^2 u}{\partial x^2} \right) + \eta \frac{\partial u}{\partial t} = n(x,t) \tag{4.22}$$

The associated autocorrelation $\mathcal{R}(T)$ for u and its relaxation time τ_d become

$$\mathcal{R}(T) = R_d \exp\left(\frac{-T}{\tau_d} \right) \tag{4.23}$$

$$\tau_d = \frac{\kappa S \eta + B \eta q^2}{\kappa S B q^4} \tag{4.24}$$

Details of this analysis are provided in the Appendix E.. For further reference, (4.24) is expanded as

$$\tau_d = \frac{\eta}{Bq^{*4}} L^4 + \frac{\eta}{\kappa S q^{*2}} L^2 \tag{4.25}$$

to reveal the explicit dependence of this relaxation time on *two* length scales. By contrast, for long filaments or long wavelengths, the WLC model ((4.20) with $\eta_b' = 0$) predicts that the relaxation time τ due to external friction depends on a single length scale per

$$\tau = \frac{\eta}{Bq^{*4}} L^4. \tag{4.26}$$

4.4.1.2 Results and discussion

Internal friction in large and small wavenumber limits

Equation (4.16), based on Timoshenko beam theory, explicitly accounts for the direct shear of filaments which is ignored in the prior formulations based on Euler-Bernoulli beam theory. Importantly, (4.16) reveals that the energy relaxation arises on *two time scales* τ_1 and τ_2. Thus, the physics of internal friction when shear is included is qualitatively different from that when shear is ignored for which single time scale relaxation (4.18) occurs. Figure 4.6 illustrates the dependence of the two relaxation times τ_1 and τ_2 (4.17) with wavenumber q over a wide range of values for $\eta_s' = \eta_b' = \eta'$ as examples. The parameters selected pertain to a thermally fluctuating chromosomal filament [58] having $E = 500$ Pa, $r = 1\mu$m, $\eta = 0.001$, and $G = 227$Pa (Poisson's

ratio $\upsilon = 0.1$) [74]. Inspection of Figure 4.6 reveals that τ_1 and τ_2 become independent of wavenumber in the large wavenumber ($q \to \infty$) limit for which (4.17) yields

$$\tau_1 \approx \frac{\eta_b' I}{B}, \quad \tau_2 \approx \frac{\eta_s' A}{\kappa S} \tag{4.27}$$

For comparison, the relaxation time (4.19) from Euler-Bernoulli theory reduces to

$$\tau \approx \frac{\eta_b' I}{B} \tag{4.28}$$

From (4.27) and (4.28), the relaxation time τ_1 from Timoshenko theory recovers the relaxation time τ from Euler-Bernoulli theory, in the large wavenumber limit. However, the relaxation time τ_2 defines a sec cted limiting behaviors at small wavenumbers. In the small wavenumber ($q \to 0$) limit, (4.17) yields

$$\tau_1 \approx \frac{\eta_s' A}{\kappa S}, \quad \tau_2 \approx \frac{\eta}{Bq^4} \to \infty \tag{4.29}$$

Thus, τ_2 reproduces the same limit from Euler-Bernoulli theory (4.19) at the small wavenumber limit which confirms the overwhelming influence of hydrodynamic drag over bending-induced internal friction [58]. As further illustrated in Figure 4.6(b) in this limit, the relaxation time τ_2 becomes independent of internal dissipation (η'), and scales with hydrodynamic drag (η); see Figure 4.6(b) (inset). However, τ_1 depends on the shear internal dissipation coefficient η_s' in this limit. In particular, for $q \to 0$, the wavelength approaches infinity, and the filament fluctuations reduce to essentially rigid body motions without significant internal friction but with significant external friction due to hydrodynamic drag.

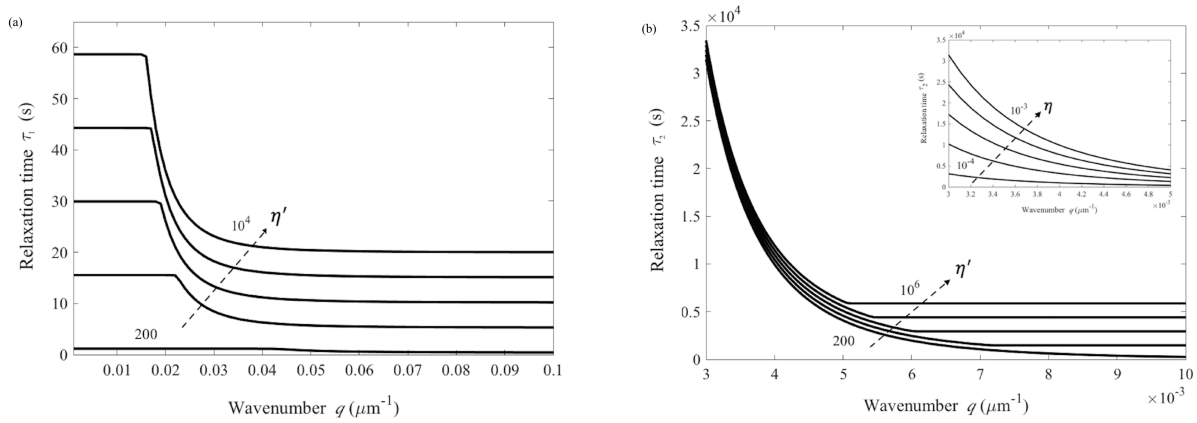

Figure 4.6: Main figure: Relaxation times (a) τ_1 and (b) τ_2 for the autocorrelation of transverse displacement of a thermally fluctuating chromosome. Properties: $E = 500$ Pa, $r = 1\mu$m, $\eta = 0.001$kg/(m.s) [58], $G = 227$Pa, and $\eta_s' = \eta_b' = \eta'$ ranging from 200 to 10^4kg/(m.s) for (a) and from 200 to 10^6 kg/(m.s) for (b). Inset: In the small wavenumber limit, the relaxation time τ_2 is independent of η', however, it scales with the hydrodynamic drag coefficient, η, ranging from 0.0001 to 0.001kg/(m.s).

Experimental evidence of shear effect on internal friction

We employ the new model, based on Timoshenko theory, to evaluate results of prior experiments on the internal friction for thermally fluctuating chromosomes of varying length [58]. The chromosomal segments considered formed cantilevers of lengths 7, 16.5, and 18.5μm having estimated properties: $E = 500$ Pa, $G = 227$Pa, $r = 1\mu$m, and $\eta = 0.001$kg/(m.s). The measured autocorrelation of the transverse fluctuations of all three chromosome lengths are illustrated in Figure 4.7(a) as well as the best-fit curves employing Timoshenko (4.16) and Euler-Bernoulli (4.18) theory. Notice that the experimental data deviate from the single time scale behavior (4.18), a feature most evident for the shortest chromosome (7μm); see Figure 4.7(b) and note log scale. For all lengths, the data clearly exhibit the two time scale behavior consistent with (4.16). Consequently, Timoshenko theory yields superior fits to the experimental data for all chromosome

lengths (Figure 4.7(b-d)) or averaged across all lengths (Figure 4.7(a)). To quantify the degree of fit, we report the root mean squared error (RMSE) between the model fit to the experimental autocorrelation in Table 4.1; refer to column 4. The root mean squared error using Timoshenko theory remains less than that for the Euler-Bernoulli theory by a factor of 4 for the shortest length (Figure 4.7(b)) to a factor of 2 (Figure 4.7(d)) for the longest length. This trend confirms the expectation that shear deformation becomes increasingly important with the shorter filament lengths commonly found in the cell.

The thermal fluctuations of the chromosomes are dominated by the smallest wavenumber bending mode, $q \approx \pi/2L$ for cantilevered chromosomes. We also report in Table 4.1 the dominant wavenumber for each of the three chromosome lengths and the associated relaxation times and internal dissipation coefficients as predicted by Timoshenko (4.16) and Euler-Bernoulli (4.18) theory. From (4.27) (and as illustrated in Figure 4.6), the relaxation times in the large wavenumber limit are approximately $\tau_1 \approx \frac{\eta_b' I}{B}$ for $q > 0.06\mu\text{m}^{-1}$ and $\tau_2 \approx \frac{\eta_s' A}{\kappa S}$ for $q > 0.007\mu\text{m}^{-1}$, respectively. Since the dominant wavenumbers of the three chromosomes ($q_{dom} = 0.22,\ 0.09,\ 0.08\ \mu\text{m}^{-1}$) are all within the range of this limiting behavior ($q > 0.06,\ 0.007\ \mu\text{m}^{-1}$), we expect the relaxation times τ_1 and τ_2 from (4.17) to be consistent with the large wavenumber limits (4.27). The process of fitting two exponentials (4.16) to the autocorrelations at the dominant wavenumbers yields two solutions for τ_1 and τ_2, one of which is readily rejected as it does not replicate the large wavenumber limit. The remaining (correct) solution yields the relaxation times τ_1 and τ_2 and internal dissipation coefficients for bending and shear reported in Table 4.1. The effective internal dissipation coefficient of mitotic chromosomes measured by dynamic force relaxation has been reported [75] as $\eta' \approx 100\text{kg}/(\text{m.s})$. Consequently, Poirier and Marko [58] expected the bending relaxation time to be 0.3s. However, the estimated relaxation time based on Euler-Bernoulli theory

(4.18) for the three chromosomes yields $\tau \approx 0.7\text{s}$ [58] and $\eta_b' \approx 350\text{kg}/(\text{m.s})$; refer to Table 4.1 and Figure 4.7(a). By contrast, the relaxation time τ_1 based on Timoshenko theory (4.16) yields $\tau_1 \approx 0.22\text{s}$, which is significantly closer to the expected value. Consequently, the bending internal dissipation coefficient $\eta_b' \approx 110\text{kg}/(\text{m.s})$ from Timoshenko theory (4.27) is also consistent with the experimental value $\eta' \approx 100\text{kg}/(\text{m.s})$ [75].

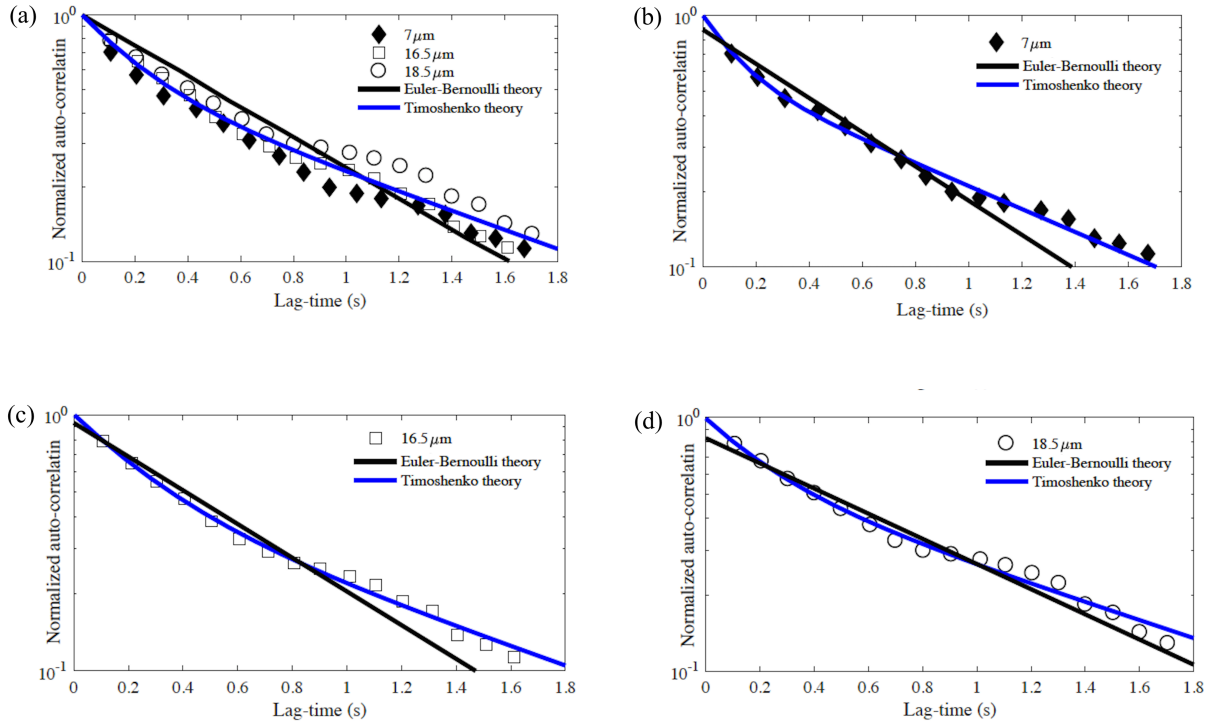

Figure 4.7: (a) Experimental autocorrelations of transverse displacement of thermally fluctuating chromosomes reported in [58] for all three chromosome lengths and with model fits determined by Timoshenko theory (4.16) and Euler-Bernoulli theory (4.18). Autocorrelations for (b) 7μm-chromosome, (c) 16.5 μm-chromosome, and (d) 18.5μm-chromosome.

Further, note that while the relaxation time calculated by Euler-Bernoulli theory (4.18) is close to the average of two relaxation times calculated by Timoshenko theory (4.16), the latter captures the two-stage (two-exponential) relaxation behavior evident in the experimental results of Figure 4.7 for all chromosome lengths. Finally note that, as mentioned before, the effect of shear increases in the large wavenumber limit, specifically when $\lambda/r < 10$ [68], and this limit naturally arises in the spectrum of the thermal fluctuations of biofilaments.

Table 4.1: The relaxation times and internal dissipation coefficients of three chromosomes modeled by Euler-Bernoulli (EB) theory and Timoshenko (T) theory. The root mean squared error (RMSE) represents the square root of the integral of the square of the difference between the experimentally measured autocorrelation and the associated theoretical fit.

Chromosome length, L (μm)	Dominant wavenumber, $q_{dom} \approx \pi/2L$ (μm^{-1})	Theory	RMSE	Relaxation time (s) from fitting (4.16) and (4.18) to experimental data	Internal dissipation coefficients (kg/(m.s)) at dominant wavenumber using (4.17) and (4.19)	Internal dissipation coefficients (kg/(m.s)) at large wavenumber limit using (4.27) and (4.28)
7	0.22	EB	0.052	$\tau = 0.64$	$\eta_b' = 319$	$\eta_b' = 320$
		T	0.013	$\tau_1 = 0.13$ $\tau_2 = 0.95$	$\eta_b' = 66$ $\eta_s' = 162$	$\eta_b' = 65$ $\eta_s' = 162$
16.5	0.09	EB	0.039	τ =0.66	η_b' =315	η_b' =330
		T	0.012	$\tau_1 = 0.27$ $\tau_2 = 1.16$	$\eta_b' = 119$ $\eta_s' = 198$	$\eta_b' = 135$ $\eta_s' = 198$
18.5	0.08	EB	0.030	$\tau = 0.87$	$\eta_b' = 410$	$\eta_b' = 435$
		T	0.015	$\tau_1 = 0.23$ $\tau_2 = 1.23$	$\eta_b' = 93$ $\eta_s' = 210$	$\eta_b' = 116$ $\eta_s' = 210$
All three-lengths combined	-	EB	0.050	$\tau = 0.70$	-	$\eta_b' = 350$
		T	0.031	$\tau_1 = 0.22$ $\tau_2 = 1.13$	-	$\eta_b' = 110$ $\eta_s' = 192$

Effect of shear on external friction due to hydrodynamic drag

Figure 4.8 illustrates the predicted dependence of τ_d with wavenumber q over a wide range of η for (chromosomal) filaments. In the large wavenumber limit ($q \to \infty$) in (4.24), $\tau_d \to \frac{\eta}{\kappa S q^2} \to 0$; see Figure 4.8. In the small wavenumber limit $(q \to 0)$ in (4.24), $\tau_d \to \frac{\eta}{Bq^4}$ which recovers the limiting behavior of Euler-Bernoulli theory (4.26). Thus, shear deformation can be ignored in the small wavenumber limit for fluctuating filaments having no internal friction. Also, in this limit, the wavelength approaches infinity and the filament fluctuations reduce to rigid body motions.

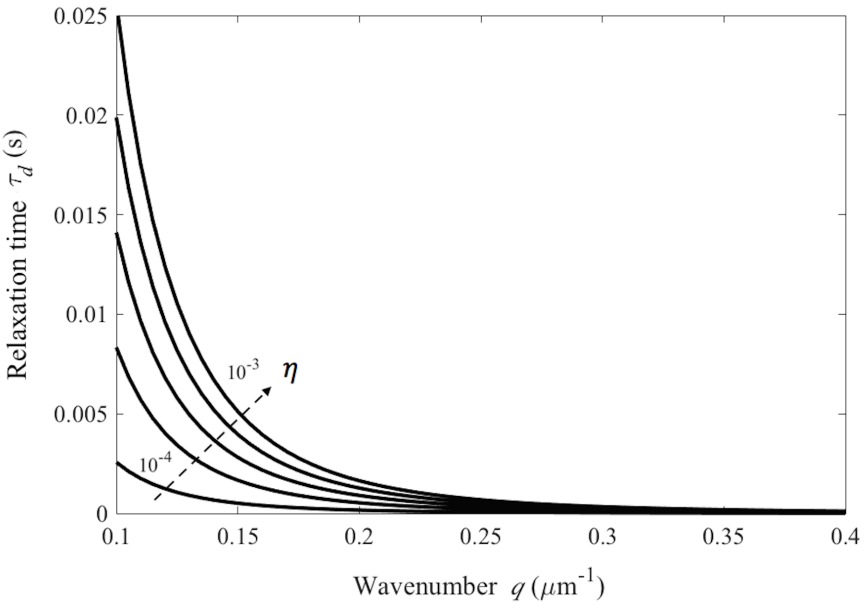

Figure 4.8: Relaxation time τ_d for the autocorrelation of transverse displacement of thermally fluctuating chromosomes with $E = 500$ Pa, $r = 1\mu$m [58], $G = 227$Pa, $\eta_s' = \eta_b' = 0$, and $\eta = 0.0001 - 0.001$kg/(m.s).

Experimental evidence for shear effect on hydrodynamic drag

In this second example, we consider the experiments of Taute et al. [67] on thermal fluctuations of microtubules spanning lengths 2-30μm. Figure 4.9 illustrates the experimentally determined relaxation time (for mean squared transverse displacement) as a function of microtubule length L for the fluctuations of the cantilevered microtubules. As described in [67], Figure 4.9 reveals that the relaxation time scales as L^4 for microtubules longer than 10 μm. However, for microtubules shorter than 10 μm, the relaxation time scales as L^2 instead, which deviates from Euler-Bernoulli theory (4.26) in which $\eta' = 0$. Suspecting the influence of internal friction, Taute et al. employed (4.20) based on Euler-Bernoulli theory, however, the relaxation time (4.20) scales as L^4 and L^0 for large and small lengths, respectively. This mismatch between the experimental data and the theoretical models ((4.20) and (4.26)) for short-length filaments arises from neglecting the shear effect in the WLC model based on Euler-Bernoulli beam theory. The experimentally-observed scaling (L^4 and L^2 for large and small lengths, respectively) is instead revealed by (4.25) which captures the influence of shear deformation. We provide in Figure 4.9 the best-fit curve to the experimental data using Timoshenko theory (4.25). Inspection reveals that the prediction based on Timoshenko theory remains a good fit at all lengths and, importantly, that it conforms to the asymptotic behaviors noted in the experiments at short lengths (L^2 –dependence) and long lengths (L^4–dependence). While this result confirms the importance of shear deformation for short microtubules, it also predicts that the dominant source of dissipation in this experiment derives from hydrodynamic effects rather than the internal friction effects as originally suspected in [67].

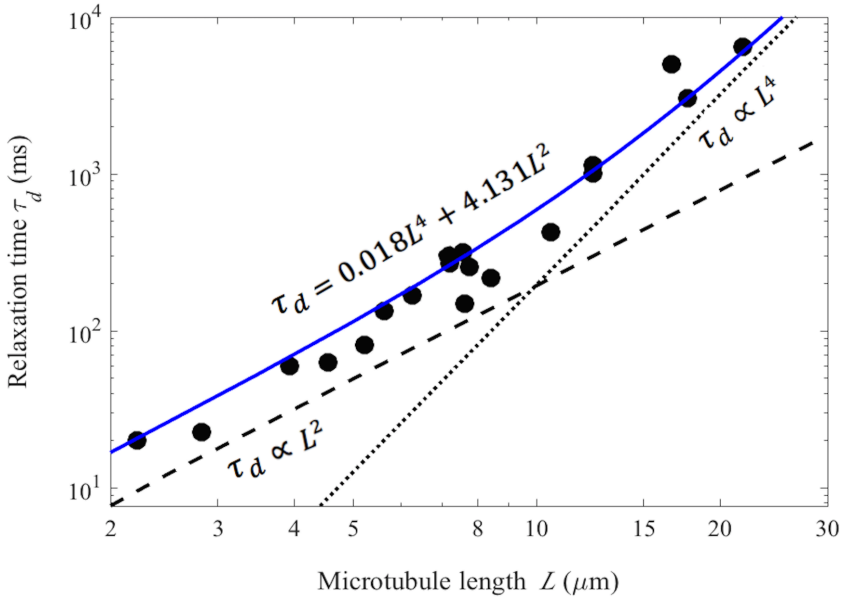

Figure 4.9: Relaxation time extracted from mean squared displacement of microtubules vs. microtubule length as measured by Taute et al. [67] from thermal fluctuations of filaments. The fitted dotted-line with slope 4 and the dashed-line with slope 2 offered in [67] reproduce the asymptotes of the Timoshenko theory (4.25) (blue curve) which remains a good approximation for all lengths.

4.4.2 Internal friction of sheath strands during contraction

We employ the theory above to estimate the internal viscosity and internal energy dissipation of the sheath strands during contraction of T4. Recall that the sheath structure of phage T4 consists of 23 'rings' of gp18 hexamers. The short-wavelength wave propagation in one ring of the tail sheath, having relatively large radius, resembles wave propagation in a straight filament [76] where the radial displacement resembles the transverse displacement of the filament; see Figure 4.10.

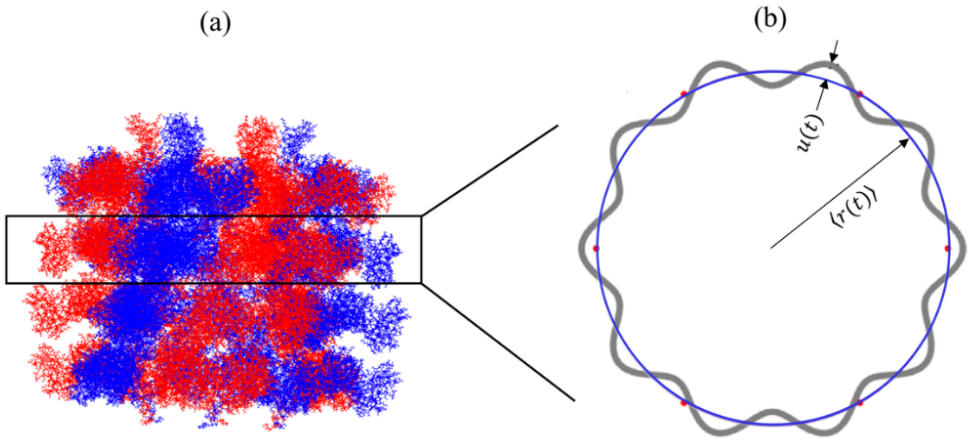

Figure 4.10: (a) Atomistic structure of the four-disc section of the T4 tail sheath with the middle ring surrounded by the superimposed rectangle. (b) The best-fit circle through the centers of masses (red dots) of the ring subunits of the middle ring has mean radius $\langle r(t) \rangle$. The radial fluctuations of the filament from the circle are denoted by $u(t)$. Figure provided by Andricioaei Laboratory (U. C. Irvine).

MD simulation was employed by the Andricioaei group at the University of California at Irvine to calculate the transverse fluctuations $u(t)$ for one ring of the sheath. To this end, the crystal structures (3.5 Å resolution) of a single ring in both the extended and contracted states are obtained from the protein data bank (PDB ids 3FOH and 3FOI, respectively) [18]. A section of the full sheath consisting of five rings is created from the single rings (Figure 4.10(a)) using published sheath helical parameters [17]. The five-ring sheaths are then used as input for Langevin dynamics applied on the non-hydrogen atoms with a friction coefficient of 5 ps^{-1}. NAMD package [43] using the CHARMM 36 all-atom force field [44] is used to generate the dynamical trajectories. A generalized Born solvent model (GMBV) is employed to implicitly represent the solvent. After minimization, the system is heated to a temperature of 298 K, followed by an unconstrained equilibration run of 5 ns. A 20 ns production run is used to generate the trajectories. During the production run, the centers of mass of the bottom and top ring monomers are

harmonically constrained with a force constant of 10 kcal mol^{-1} $Å^{-2}$ to avoid any overall rotation or surface rupture of the sheath.

One of the middle rings of the four-ring sheath is considered as a representative (circular) filament for the T4 sheath structure (Figure 4.10(a)). The middle ring is chosen to minimize solvent surface effects to radial fluctuations. Transverse fluctuations $u(t)$ are defined as the radial fluctuations of the best-fit circle passing through the center of masses of the six subunits of the ring (Figure 4.10(a))). For each frame of the trajectory, the center and radius $r(t)$ of the best-fit circle was calculated, and the radial deflection $u(t)$ is defined as $u(t) = r(t) - \langle r(t) \rangle$. The autocorrelation function $\mathcal{R}(T) = \langle u(t), u(t+T) \rangle$ is then calculated from the trajectories for both the extended and the contracted states.

Fitting a one-exponential function (4.23) for $\mathcal{R}(T)$ for the extended and contracted rings yields the relaxation time τ_d and then the equivalent dissipation coefficient η for each conformation per (4.24). Therefrom, the equivalent dissipation coefficient is estimated as η = 0.003 Pa.s in the extended state and η = 0.008 in the contracted state. As a further illustration of this procedure, Figure 4.11 shows the autocorrelation of the transverse displacement of a middle ring of the sheath fragment in both the extended and contracted conformations using MD simulation. Superimposed on this data are the best-fit curves employing (4.23) from which we compute the relaxation time τ_d.

Finally, the (Stoke's) drag model is again employed to model the net internal dissipation as an equivalent (but now significantly increased) external hydrodynamic drag using the friction coefficient $\bar{\eta} \cong 0.005$ Pa.s which is the average across the extended and contracted conformations. These equivalent external hydrodynamic drag force and moment on sheath strands are added to

(1) and (2), respectively. The details of this simulation and the effect of this and all other sources of dissipation are discussed in Chapter 5.

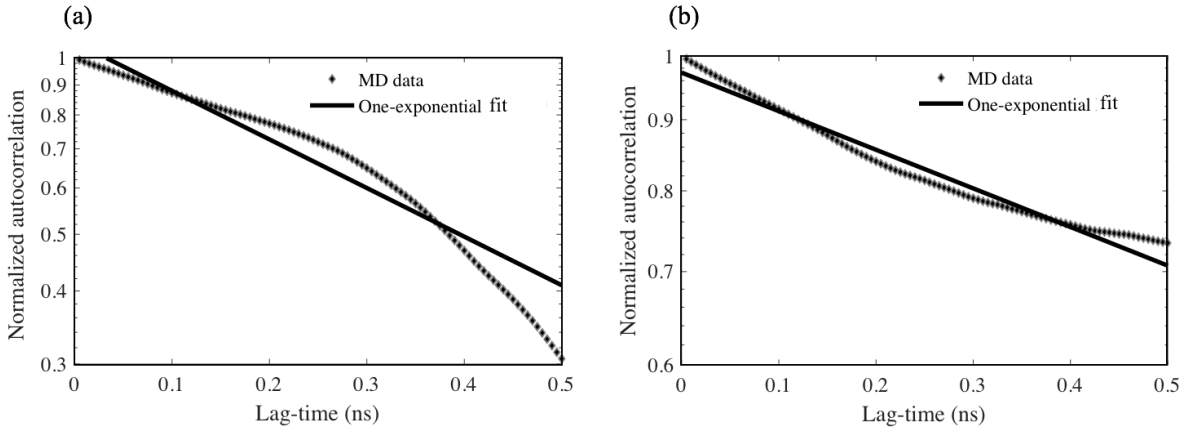

Figure 4.11: Autocorrelation of the transverse displacement of a middle ring of the sheath fragment from MD simulation for (a) the extended conformation and (b) the contracted conformation. The discrete data points indicate the MD-derived autocorrelation and the solid line represents the best fit per (4.23). Note log scale on vertical axis. MD data provided by Andricioaei Laboratory (U. C. Irvine).

Chapter 5

Complete system-level dynamic model of phage T4 interacting with host cell

In Chapter 3, we proposed a coarse-grained dynamic model to simulate the entire injection machinery of phage T4. In that model, all sources of energy dissipation, excluding hydrodynamic drag on sheath and capsid, were ignored. The resulting model estimated that (1) the driving energy of sheath contraction is about 5500kT which is on the order of experimentally measured driving energy 5800kT (3400kcal/mol) in urea-induced sheath contraction [25], (2) the extended sheath provides the maximum cell rupture force of 860pN which is consistent with the lower-bound estimate of 103pN calculated theoretically in [31], and (3) the timescale of sheath contraction is about 6μs. In this chapter, we extend that model to a complete system-level model by simulating the other important sources of energy dissipation including 1) the tail tube-cell interaction both prior to and following the rupture of the host cell membrane, 2) the sheath-tube friction during sheath contraction, and 3) internal (material) dissipation of sheath strands during large conformational changes during contraction. We also extend the model to simulate the wave propagation mechanism of sheath contraction, predicted by Moody [28] and Guerrero-Ferreira [30], by defining the non-homogenous elastic stiffness constants for the sheath strands

(rods). The approximate models of all sources of energy dissipation (proposed in Chapter 4) and non-homogenous elastic stiffness constants of sheath strands are employed in the continuum model of sheath (proposed in Chapter 3) yielding a comprehensive system-level model of the injection machinery for predicting the dynamics, energetics, and the time scale of the injection process.

5.1 Methods

The dynamics of the injection process is governed by the competition between two energetic processes: 1) the internal (elastic) energy released from the sheath that powers the injection, and 2) the dissipation of energy during injection from multiple sources. We provide below brief summaries of the models for each of these energetic processes.

5.1.1 Internal energy that powers the injection machinery

As proposed in Chapter 3, the injection machinery of phage T4 is modeled as the six interacting helical rods. (Equations (3.3)-(3.6)) representing the sheath which connects to the baseplate at the lower end (Equations (3.13)-(3.14)) and to the capsid/neck/tail tube assembly at the upper end (Equations (3.14)-(3.17)). The energy required for the tip of the tail tube to pierce the host cell derives from the sudden release of the internal energy stored in the extended sheath during contraction. In our model, the internal energy of the sheath is represented by the strain (elastic) energy of the six interacting strands (rods). The internal energy of the sheath (in any state during contraction) is given by the strain energy of the six interacting helical protein strands (rods) per (3.11). In the following, we calculate the elastic stiffness constants required in (3.11).

5.1.1.1 Estimating the elastic properties of the sheath strands

The bending and torsional elastic stiffness constants of each strand (rod) are derived from MD simulations carried out by our collaborators in the Andricioaei group at the University of California at Irvine. The elastic stiffness constants reported in Table 3.1 is based on the fact that the structure of inner domain C of the sheath subunit gp18 is still unknown. Our collaborators conducted new MD simulations to approximately model the inner domain C using the known structure of the R2-pyocin monomer. We provide a brief summary of their steps for reference.

Our collaborators employed MODELLER [77] to generate a homology model of the missing residues using the structure of the R2-pyocin monomer. The structure of the full gp18 monomer was then reconstructed by superposing the atomic structure of the homology models on a superposition of the R2-pyocin and partial gp18 monomers using the CLICK algorithm [78]. Finally, the resultant full gp18 model was oriented in the same orientation as the original hexamer, and then the hexamer was fitted into the cryo-EM maps of the extended and contracted sheath [7] using the program UCSF Chimera [54]. A fraction of the full sheath consisting of four rings was created from the single ring using published sheath helical parameters [7]. The four-ring sheaths were then used as input for Langevin dynamics applied on the non-hydrogen atoms with a friction coefficient of 5 ps^{-1}. NAMD package [43] using the CHARMM 36 all-atom force field [44] was used to generate the dynamical trajectories. A generalized Born solvent model was employed to implicitly represent the solvent. After minimization, the system was heated to a temperature of 298 K, followed by an unconstrained equilibration run of 15 ns. The bending and torsional stiffness for each strand were computed from (3.1) and (3.2) and listed in Table 5.1. Comparing results from Table 3.1 (without the domain C) with Table 5.1 (with the approximate domain C), we observe

that the elastic stiffness constants in the presence of inner domain C are greater than those for subunits with the missing domain C as expected.

Table 5.1: Elastic bending and torsional stiffness constants of the sheath strands for phage T4 in both the extended and contracted conformations including the homology model for inner domain C. Results provided by Andricioaei Laboratory (U. C. Irvine).

Strand type	Bending stiffness ($10^{-27}\mathrm{N.m^2}$)	Torsional stiffness ($10^{-27}\mathrm{N.m^2}$)
Extended sheath, gp18	67.7	18.9
Contracted sheath, gp18	81	263

5.1.1.2 Non-homogeneous sheath stiffness and dynamic contraction wave

From the micrographs of partially contracted sheaths [28], Moody hypothesized that the sheath contraction is displacive whereby the subunits forming a single ring displace identically and in unison to produce a contraction wave that propagates upwards from the baseplate (adjacent to first ring) to the neck (adjacent to last ring); see Figure 5.1(a) . Thereafter, Caspar [29] created a mechanical model to simulate the wave propagation mechanism of phage T4; Figure 5.1(b). Caspar's mechanical model [29] utilized removable connections (links) between the mechanical elements (i.e., sheath subunits) and a central column (i.e., tail tube) to release each (elastically strained) ring of mechanical elements in upward succession. In addition, a recent experimental study on bacteriophage A511 (a contractile injection machinery that is very similar to phage T4) by Guerrero-Ferreira et al [30] confirms the wave propagation mechanism of sheath contraction

proposed by Moody [28]; Figure 5.1(c). The experiment, conducted under near-native conditions, shows that sheath contraction in phage A511 starts from the baseplate and propagates toward the neck [30] as also predicted for phage T4.

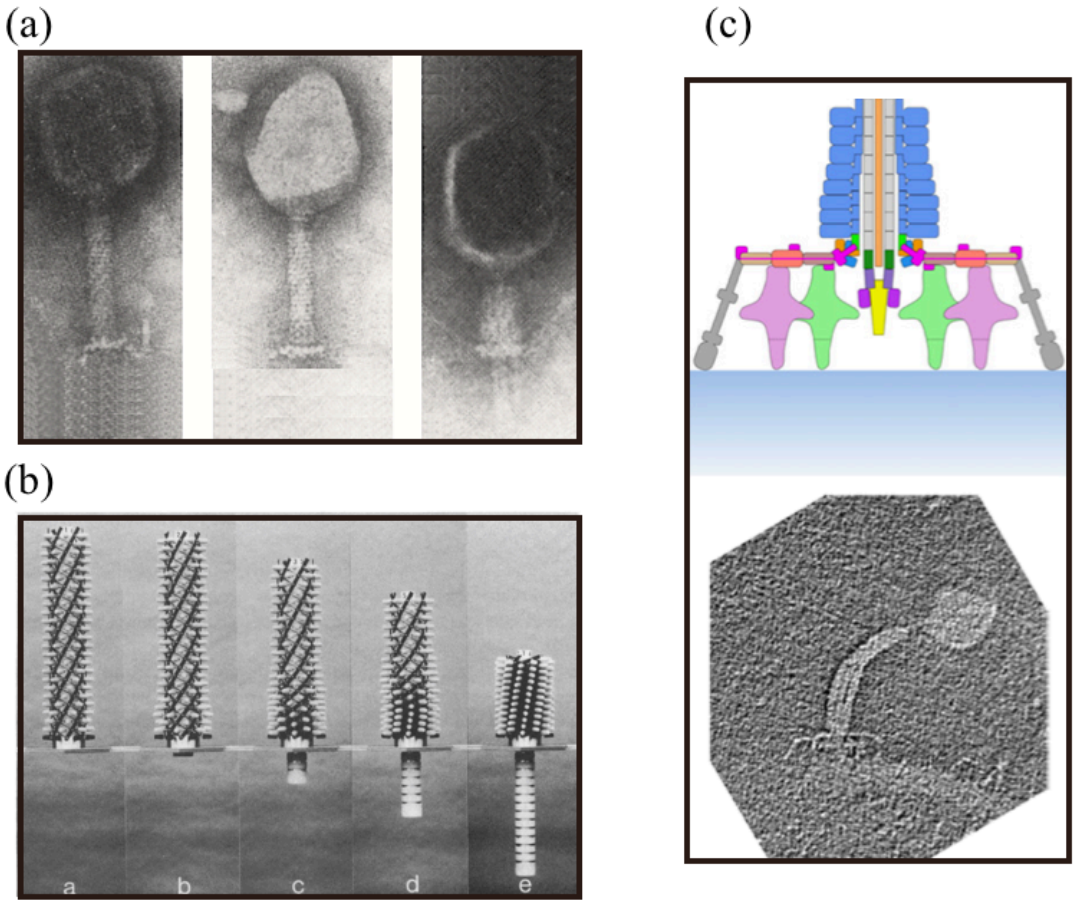

Figure 5.1: The intermediate structure of sheath during contraction reveals that the sheath contraction has a wave propagation mechanism starting from the baseplate toward neck. (a) Micrographs of sheath in extended (I) , partially contracted (II), and fully contracted (III) conformations reported by Moody [28], (b) Steps of phage T4 contraction modeled by Caspar's mechanical model, and (c) the partially contracted intermediate structure of phage A511 [30].

Our MD simulations also reveal that, due to changes in the sheath subunit contacts, the elastic stiffness constants of the sheath strands in the contracted state are larger than those in the extended state; see Table 5.1. Consistent with contraction wave mechanism observed in experiments [28,30] and our MD-derived stiffness constants, we propose the following sheath contraction model. Prior to injection, the sheath remains in the extended conformation wherein interactions between the sheath and tail tube subunits retain the sheath in the high energy state. Sheath contraction is triggered by a large conformational change of the baseplate that breaks the interactions between the local sheath-tail tube subunits enabling displacive contraction starting at the first ring of sheath subunits. The sheath-tube subunit interactions are then broken sequentially upwards in each ring from the baseplate towards the neck enabling the sheath subunits to rotate and translate in forming new contacts and thus new local stiffness properties. As a consequence, an intermediate conformation of the sheath would consist of a partially contracted region extending upwards from the baseplate possessing larger elastic stiffness constants (similar to the fully contracted sheath) and a partially extended sheath (extending downwards from the neck) possessing smaller elastic stiffness constants. Hence, the resulting intermediate would possess *non-homogenous* stiffness constants with the region closest to the baseplate possessing stiffness parameters close to those of the contracted conformation and the region closest to the neck possessing stiffness parameters close to those of the extended conformation. The non-homogenous stiffness constants and the resulting wave-like sheath contraction mechanism predicted by Moody [28] are modeled as described next.

The contraction process is initiated in the model by prescribing the radial velocity v_r appearing in the boundary condition (3.13) to rapidly expand the baseplate. As a result, the capsid/neck/tail tube assembly begins to translate towards the baseplate. We denote this translation

by the parameter $0 \leq h_c \leq H$, which measures the state of contraction between the limits of the fully extended conformation ($h_c = 0$) and the fully contracted conformation ($h_c = H \cong 500$ Å). The non-homogenous stiffness tensor of the strands forming the sheath is modeled per

$$\boldsymbol{B}(s, h_c) = \boldsymbol{B_e} + (\boldsymbol{B_c} - \boldsymbol{B_e})\left(1 - e^{\frac{-\alpha h_c}{H - h_c}}\right), \quad \alpha(s) = \frac{(\alpha_L - \alpha_0)s}{L} + \alpha_0 \tag{5.1}$$

where $\boldsymbol{B_e}$ and $\boldsymbol{B_c}$ denote the limiting stiffness tensors for the extended and contracted sheaths, respectively, and as composed by the values reported in Table 5.1. The linear function $\alpha(s)$ controls an exponential increase in the stiffness tensor from that of the extended state to that of the contracted state as determined by the two rate parameters (α_0, α_L). The rate parameter α_L controls the (initially slower) growth in stiffness at the neck $(s = L)$ whereas the rate parameter α_0 controls the (initially rapid) growth in stiffness at the baseplate $(s = 0)$. In the simulation results reported herein, we select $\alpha_0 = 5$ and $\alpha_L = 1$. Figure 5.2 illustrates the variation of bending and torsional stiffness coefficients along the sheath strands as a function of contraction h_c. Note that the dynamics of the simulated injection process is actually quite insensitive to the choice of the rate parameters (e.g., the ratio α_0/α_L influences the injection time only on the microsecond time scale).

During sheath contraction, the arc length *L* of the sheath strands increases by approximately 400 Å and this increase is also captured in the model. We employ an interpolation function for *L* that is analogous to that used in (5.1) for the stiffness tensor, as both the stiffness and length of the strands are controlled by the same (displacive) process. In particular,

$$L(h_c) = L_e + (L_c - L_e)\left(1 - e^{\frac{-\beta h_c}{H - h_c}}\right), \tag{5.2}$$

where L_e and L_c denote the limiting strand arc lengths for the extended and contracted conformations, respectively. The parameter β controls the exponential increase in the strand arc length and the value $\beta = 0.2$ was selected for the simulations reported herein. Again, the time scale of the injection dynamics is largely insensitive to this choice.

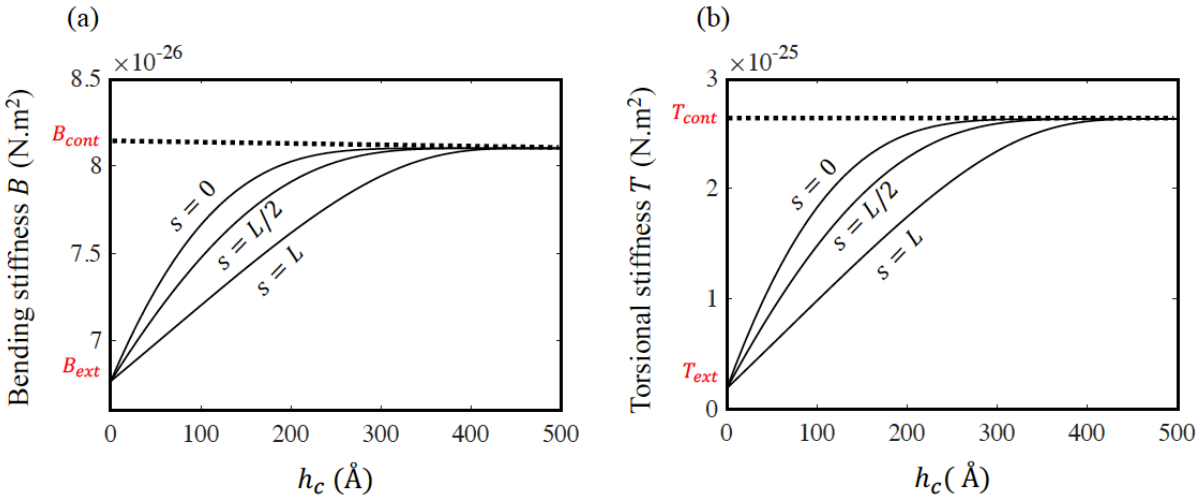

Figure 5.2: The non-homogenous bending (a) and torsional (b) stiffness coefficients along sheath strands employing (5.1), in which $\alpha_0 = 5$ (rapid growth) at the baseplate ($s = 0$) and $\alpha_L = 1$ (slower growth) at the neck ($s = L$). The stiffness coefficients of all points on the sheath increase from the values for extended sheath to those for the contracted sheath, as reported in Table 5.1.

5.1.2 Mechanisms that dissipate energy during injection

Four mechanisms that dissipate energy for the phage T4 injection machinery are captured in the model. These include: 1) the hydrodynamic dissipation on the capsid and sheath from the surrounding environment, 2) the internal (material) dissipation of the sheath strands during the large conformational change, 3) the dissipation from the host cell membrane interacting with the tip of the tail tube, and 4) the hydrodynamic interactions between the flexible sheath and the tail

tube during contraction. To predict the time scale and dynamics of the phage T4 injection machinery, one must quantify and model each dissipation mechanism. The details of modeling for each mechanism have been provided in Chapter 4, and we only provide a brief summary of each mechanism below.

5.1.2.1 Hydrodynamic dissipation on capsid and sheath

During sheath contraction, the sheath and capsid are subject to nanoscale hydrodynamic drag forces and moments from the surrounding fluid environment (water). which are modeled using classical (Stoke's regime) drag given by Equations (3.11)-(3.12) for the sheath and (3.18) for the capsid employing the viscosity of bulk water; namely ~ 0.001 Pa. s at room temperature.

5.1.2.2 Internal dissipation of sheath strands

During sheath contraction, the helical protein strands undergo a nonlinear conformational change from the extended state to the contracted state. Cryo-EM maps reveal that, during this change, the gp18 subunits within each strand rotate and translate in forming new contacts without significant change to their atomic structure [18]. The resulting motion produces internal dissipation (due to forming new contacts). At the continuum (rod) level, this is captured by coupled bending and shear deformations. The internal dissipation coefficients for shear and bending are estimated from MD-derived thermal fluctuations. To simplify the numerical procedure, the internal dissipation is modeled by an equivalent external (fluid) dissipation by selecting a fluid viscosity that yields the same net energy dissipation as the internal dissipation; for further details refer to Section 4.4. As

illustrated in Figure 4.11, the equivalent dissipation coefficient is estimated as η = 0.003 Pa.s in the extended state and η = 0.008 in the contracted state. The (Stoke's) drag model ((4.2)-(4.3))is again employed to model the net internal dissipation as an equivalent (but now significantly increased) external hydrodynamic drag using the friction coefficient $\bar{\eta}_{int} \cong 0.005$ Pa.s which is the average across the extended and contracted conformations. These equivalent external hydrodynamic drag force and moment on sheath strands are added to Equations (3.17) respectively, through the terms $\boldsymbol{F}_{drag}$ and $\boldsymbol{Q}_{drag}$.

5.1.2.3 Cell-tail tube dissipation

The gram-negative bacterial cell envelope is a complex structure consisting of the outer membrane, the periplasmic space, and the inner membrane (plasma membrane). During sheath contraction, the tail tube simultaneously rotates (one turn counter-clockwise) and translates downward (about 500Å) to pierce and enter this envelope. Before sheath contraction, the baseplate with the dome-shaped structure is about 100Å from the cell surface [20]; see Figure 1.5(b). When the extended sheath contracts about 100Å, the tail tube touches the outer membrane (Figure 1.5(c)). Further contraction leads to cell indentation (Figure 1.5(c-d)). There is lack of information on the maximum indentation $z(t_2)$ for *E.coli* infected by phage T4, however, an upper limit of indentation $z(t_2)$ is 400Å. The cell membrane applies an upward indentation force to the tail tube which consequently decelerates the sheath contraction. As described in Chapter 4 and illustrated in Figure 4.2, the viscoelastic behavior of the outer cell membrane is modeled by an elastic spring with stiffness k_1 for instantaneous deformation in series with the parallel spring and dashpot with stiffness k_2 and damping coefficient D_c, respectively, for time-delayed deformation of the

membrane [52]. The dynamic viscoelastic behavior of *E.coli* K12 membrane under a constant force applied by an AFM tip reveals that $k_1 = 0.056$ N/m, $k_2 = 0.54$ N/m, and D_c= 0.36 N.s/m [52]. To simulate the effects of cell indentation force on the injection process during a time period $t = [t_1, t_2]$, the time-variant indentation force F_{ind} in Equation (4.7) is applied to the upper boundary conditions of the sheath (3.17).

After rupturing the outer membrane, the tip of the tail tube is immediately subject to the hydrodynamic drag of the periplasmic space during a time period $t = [t_2, t_3]$; see Figure 1.5(d-e). The resulting hydrodynamic drag and moment on the tail tube is modeled by Stoke's regime drag given by Equations (4.8)-(4.9). Different layers of cell membrane likely have different viscosities. The viscosity of the plasma membrane of *E.coli* at room temperature was measured to be 1.160 Pa.s using a molecular rotor [79]. For lack of further data, we assume that all layers of *E.coli* cell membrane have viscosity $\eta_c = 1.160$ Pa. s.

5.1.2.4 Sheath-tail tube friction

Despite the wealth of information on the atomic structure of the sheath and the tail tube, possible interactions between them remain largely unknown. Potential sheath-tube interactions may arise from electrostatic and non-bounded forces and from viscosity in the nano-scale gap (interstitial water) between the tail tube and the surrounding sheath. Importantly, these interactions likely retard the injection process thereby affecting the injection time-scale. From cryo-EM data [17,18,24], the charge distributions along the inner sheath surface and the outer tail tube surface of phage T4 are relatively uniform (see Figure 4.3). This implies that the net electrostatic and nonbonded forces will be largely perpendicular to the tail tube axis and thus contribute

insignificant work as the tail tube translocates through the sheath. By contrast, a significant interaction may arise during translocation from the large viscosity of the interstitial nano-scale gap. To simulate this friction between the sheath and the tail tube, we employ a classic model of fluid motion between two parallel surfaces having linear velocity profiles; see Figure 4.4. These friction force and moment are given by Equations (4.10) and (4.11) and added to Equations (3.17) respectively, through the terms $\boldsymbol{F}_{drag}$ and $\boldsymbol{Q}_{drag}$.

5.2 Results and discussion

The energetic mechanisms above that supply and dissipate energy during the injection process are incorporated into the system level model of the assembled phage T4 interacting with a host cell. Numerical solutions of this system level model yield the first ever predictions of the energetics, the virus-cell interaction forces, the dynamic pathway including the contraction wave, and the overall timescale of the injection process.

5.2.1 Energetics of the injection machinery and virus-cell interaction forces

The dynamic model of the phage T4 injection machinery estimates the energetics of the entire injection process, including the initial energy stored by the sheath and how that energy is dissipated, and the interaction forces with the host cell. Figure 5.3 illustrates the computed internal (elastic) energy of the six sheath strands and how that energy is released as a function of time during the entire injection process. Before contraction (Figure 5.3(a)) the sheath is in the high-energy extended state. The elastic sheath model estimates that the contraction process is driven by

approximately 14500 kT of stored energy which is reasonably consistent with the experimentally reported enthalpy of sheath contraction in [25]; namely, 5800 kT for urea-induced contraction and 10,000 kT for heat-induced contraction. Following the conformational change of the baseplate, the tail tube (and the attached sheath) are released from the grip of the baseplate which initiates the rapid energetic release depicted in Figure 5.3. As the sheath contracts, the tail tube first touches the outer cell membrane (Figure 5.3(b)) and further contraction leads to increasing cell indentation (Figure 5.3(c)) and ultimately cell rupture. Following that event, the tip of the tail tube enters the periplasmic space subject to additional drag (Figure 5.3(d)). The injection concludes when the tip has translated the total distance ∼500 Å from its starting position. Overall, the injection process is highly overdamped (evident from Figure 5.3) and thus the kinetic energy of the injection machinery remains quite small relative to the initial energy stored in the sheath.

While the rupture force (or stress) for *E. coli* remains largely unknown, experimental studies on lipid bilayers [80] (which mimic the outer cell membrane) yield an estimate for our model. Those experiments employ an AFM with a pyramidal tip to rupture the lipid bilayer with a force of 10 nN and at an indentation of 6 nm. Assuming that *E.coli* has approximately the same rupture stress as the lipid bilayer, we predict that the required force to rupture the cell membrane by the 9Å-diameter tip of the tail tube [81] is ∼330 pN and that occurs at an indentation of ∼ 60 Å. Figure 5.4 illustrate the indentation force on the outer membrane from the tail tube as a function of time during the injection process. The indentation force increases linearly upon tip-membrane contact and until rupture of the outer membrane at the estimated indentation/membrane rupture stress. After the rupture event, the indentation force vanishes, and the tail tube is subject to the added hydrodynamic drag from the inner layers of the periplasmic space (Figure 5.3(c-d)).

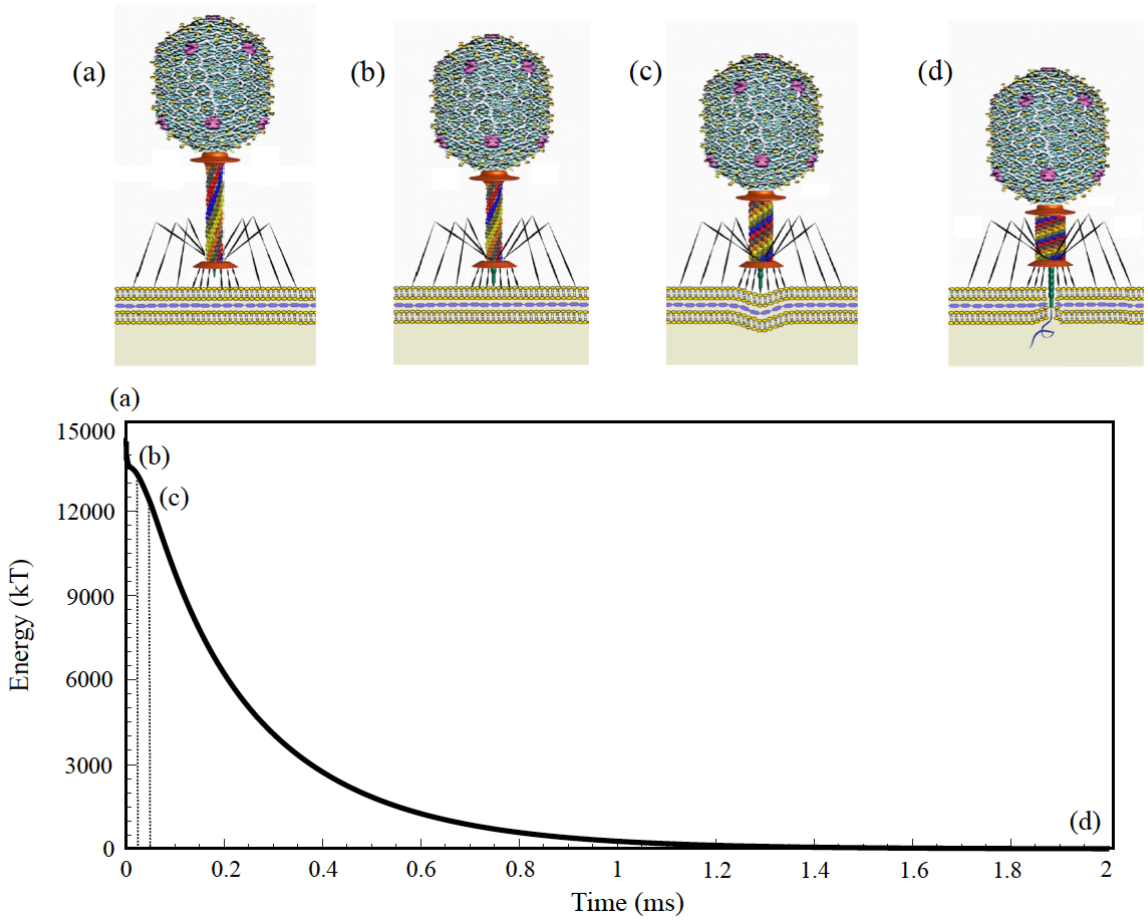

Figure 5.3: Complete model of the T4 injection machinery predicts the internal (elastic) energy of the contractile sheath that drives the injection process. (a) The sheath begins in the (high-energy) extended state where the tip of the tail tube remains 100 Å from the cell membrane. (b) The sheath contracts 100 Å so that the tip of the tail tube touches the outer cell membrane. (c) Further contraction of the sheath produces, in sequence, cell indentation, rupture of the outer cell membrane (after 60 Å indentation), and penetration into the (viscous) periplasmic space. (d) The fully contracted sheath with zero elastic energy. Note, in this simulation, $\eta_w = 30$ Pa.s and $\bar{\eta}_{int} = 0.005$ Pa.s.

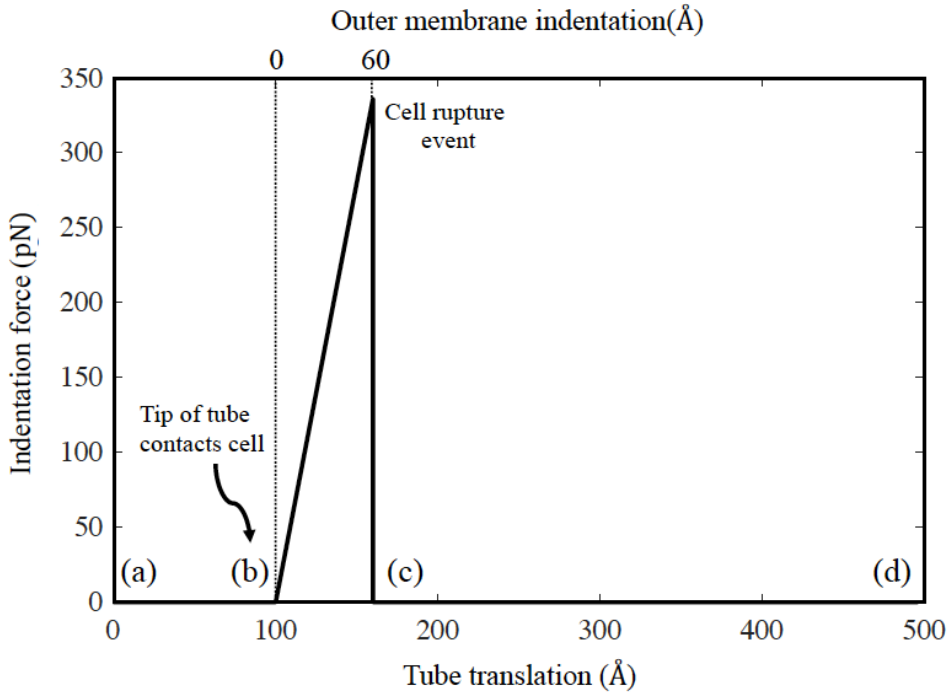

Figure 5.4: Indentation force from the outer membrane of the cell on the tip of the tail tube. The injection machinery in states (a), (b), (c) and (d) are illustrated in for Figure 5.3(a-d), respectively.

During injection, the elastic energy stored in the extended sheath is dissipated through the four energy dissipation mechanisms discussed above. Of these mechanisms, the parameters describing the hydrodynamic dissipation on the capsid/sheath and the cell-tail tube dissipation are reasonably well understood. However, we must consider a wider range of model parameters for the remaining mechanisms that are lesser understood; namely, the internal dissipation of the sheath strands and the dissipation due to sheath-tail tube friction.

The friction coefficient $\bar{\eta}_{int}$ governing the internal dissipation of the sheath strands is estimated to be 0.005 Pa.s from MD-derived thermal fluctuations, which is on the order of the

viscosity of bulk water. However, the amplitude of the fluctuations in the MD simulations are on atomistic length scales, whereas the sheath undergoes a conformational change that is several orders of magnitude larger. Consequently, the friction coefficient $\bar{\eta}_{int}$ may actually be far greater and perhaps similar to that of thermally fluctuating actin filaments (1 Pa.s) which is about three orders of magnitude greater than the viscosity of bulk water [58]. Consequently, in the following, we explore behaviors over a wide range of values $0.005 < \bar{\eta}_{int} < 5$ Pa.s. Similarly, the sheath-tail tube friction coefficient may vary considerably with the properties of the interstitial nano-scale gap between the sheath and tail tube. The water confined to this gap exhibits distinct viscosity characteristics compared to bulk water and these characteristics strongly depend on the gap thickness and the degree of surface hydrophilicity/hydrophobicity. Experimental studies [56,57] reveal that the greater the affinity between the water molecules and the surfaces forming the nano-scale gap, the greater the effective viscosity. For example, the viscosity of water confined to a 1.3 nm gap between an oxide-terminated tip of an interfacial force microscope and a silica surface is about six orders of magnitude greater than the viscosity of bulk water [56]. From experimental data, the nanochannel between the tube and sheath is largely hydrophilic (see Figure 4.3(b)) resulting in an effective viscosity that may be significantly greater than that of bulk water. Accordingly, we explore behaviors over a wide range of values $0.001 < \eta_w < 1000$ Pa.s encompassing values for bulk water to nano-scale layers with highly hydrophilic surfaces [56].

Figure 5.5 illustrates the relative (%) energy dissipation due to all four dissipation mechanisms for select values of $\bar{\eta}_{int}$ and η_w within the above ranges. Doing so reveals the possible regimes where each dissipation source may dominate. For instance, at the lower limits ($\eta_w = 0.001$ Pa.s and $\bar{\eta}_{int} = 0.005$ Pa.s), the dominant dissipation mechanism derives from cell-tail tube dissipation; refer to CTTD in Figure 5.5(a). However, for $\eta_w = 0.001$ Pa.s and $\bar{\eta}_{int} > 0.1$ Pa.s,

the dominant dissipation mechanism becomes the internal dissipation of the sheath strands; refer to IDSS in Figure 5.5(b). Finally, sheath-tail tube friction becomes the dominant dissipation mechanism for $\eta_w > 0.5$ Pa.s, regardless of $\bar{\eta}_{int}$; refer to STTF in Figure 5.5(c). Interestingly, the hydrodynamic dissipation on the capsid/sheath always remains of secondary or lower importance; refer to HDCS in Figure 5.5. Overall, these results demonstrate that several mechanisms are likely responsible for dissipating the initial energy stored in the sheath. The analysis of energy dissipation remains an intriguing avenue for future experimental and theoretical research, particularly given that energy dissipation plays a governing role in establishing the time scale of the injection process as discussed below.

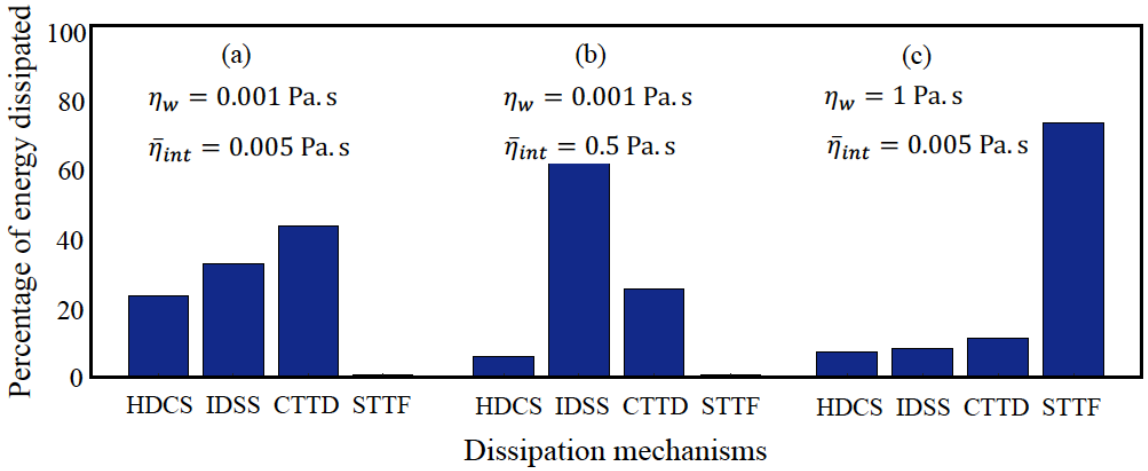

Figure 5.5: Model of T4 interacting with host cell predicts the relative (%) contribution of all four dissipation mechanisms during injection. Here, HDCS defines the percent energy dissipation due to hydrodynamic dissipation on the capsid/sheath; IDSS that due to internal dissipation of the sheath strands; CTTD that due to cell-tail tube dissipation, and STTF that due to sheath-tail tube friction. (a) For $\eta_w = 0.001$ Pa. s and $\bar{\eta}_{int} = 0.005$ Pa. s, CTTD emerges as the dominant source of energy dissipation. (b) For $\eta_w = 0.001$ Pa. s and $\bar{\eta}_{int} = 0.5$ Pa. s, IDSS emerges as the dominant source of energy dissipation. (c) For $\eta_w = 1$ Pa. s and $\bar{\eta}_{int} = 0.005$ Pa. s, STTF emerges as the dominant source of energy dissipation.

5.2.2 Dynamic pathway of the injection process

The dynamic model of the phage T4 injection machinery reveals the conformational change of the sheath as a nonlinear contraction wave and the companion dynamics of the attached capsid/neck/tail tube assembly. During sheath contraction, the sheath subunits translate and rotate during the large conformational change from the extended state to the contracted state.

The model simulation captures the dynamic contraction wave starting from the computed dynamic conformations of the six interacting helical gp18 protein strands that form the sheath. In particular, the continuum (rod) model for each strand yields the strand centerline that passes through the mass centers of the constituent gp18 subunits. From the known centerlines of each strand, we then reconstruct atomistic representations of the entire sheath using MATLAB and VMD; see Appendix F. Figure 5.6 compares selected snapshots of the simulated injection dynamics with the experimental micrographs images provided by Moody [28]. In particular, Figure 5.6(a) illustrates the fully extended (IV), a partially contracted (V), and the fully contracted (VI) sheath as selected from the movie frames. These images, representing the computed output from the system model, are consistent with the experimental micrograph images for the fully extended (I), a partially contracted (II), and fully contracted (III) sheath reported by Moody [28].

As the contraction wave passes, the helical strand angle θ decreases and the helical strand radius increases. The resulting "wave front" of the propagating contraction wave is best visualized in Figure 5.6(b) that shows the helical strand angle as a function of location along the strand for the fully extended, a partially contracted, and the fully contracted sheath strands. Note that the helical strand angle is reduced by approximately 45 degrees during contraction and that this rotation begins at the baseplate and propagates upwards along each strand to the neck. This finding

is consistent with the cryo-EM data that reveals that the sheath subunits rotate ~45 degrees about the radial axis passing through the subunits [18] following contraction.

Figure 5.7 reports the dynamics of sheath contraction by illustrating the simultaneous translation and rotation of the capsid/neck/tail tube assembly along/about the tail tube axis as functions of time. Note that, over the entire injection process, the capsid/neck/tail tube assembly translates downward by about 500 Å and rotates approximately one turn counter-clockwise (when viewed from above the capsid) about tube axis which is consistent with cryo-EM data for the extended and contracted sheath [16]. Moreover, this figure reveals that the dynamic contraction grows rapidly at the start of injection and decays exponentially at the end. The initial rapid translation with rotation provides a two-punch mechanism for mechanically rupturing the outer cell membrane (see Figure 5.7(a-c)).

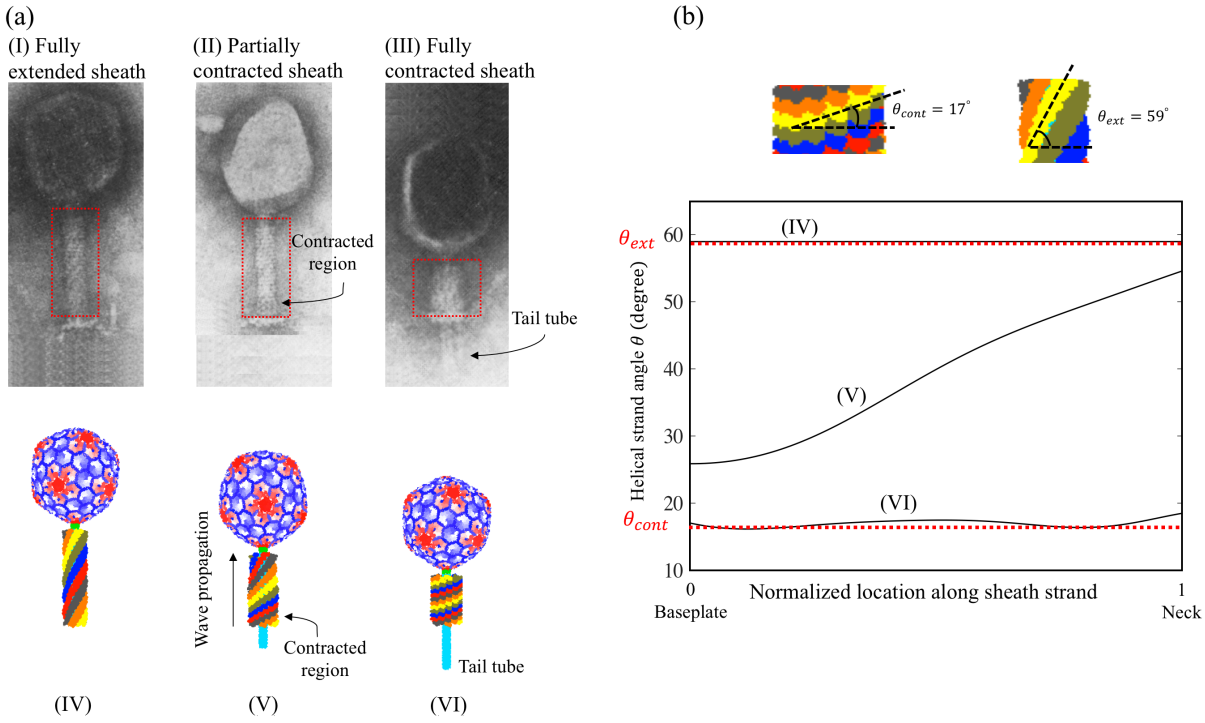

Figure 5.6: Simulation reveals contraction dynamics of the sheath from the fully extended conformation to the fully contracted conformation, consistent with the experimental micrographs reported by Moody [28]. (a) Micrographs of sheath in extended (I) , partially contracted (II), and fully contracted (III) conformations [28]. The snapshots illustrate model simulated extended (IV), partially contracted (V), and fully contracted (VI) conformations. Individual black and blue helices denote (the centerlines of) the six interacting helical gp18 protein strands that form the sheath. Intermediate conformation (V) captures contraction wave propagation from the (lower) baseplate towards the (upper) neck. (b) The helical strand angle θ as a function of location along the strand. As the contraction wave passes, the helical strand angle θ decreases from that of the extended conformation (IV) with $\theta_{ext} = 59$ degrees to that of the contracted conformation (VI) with $\theta_{cont} = 17$ degrees.

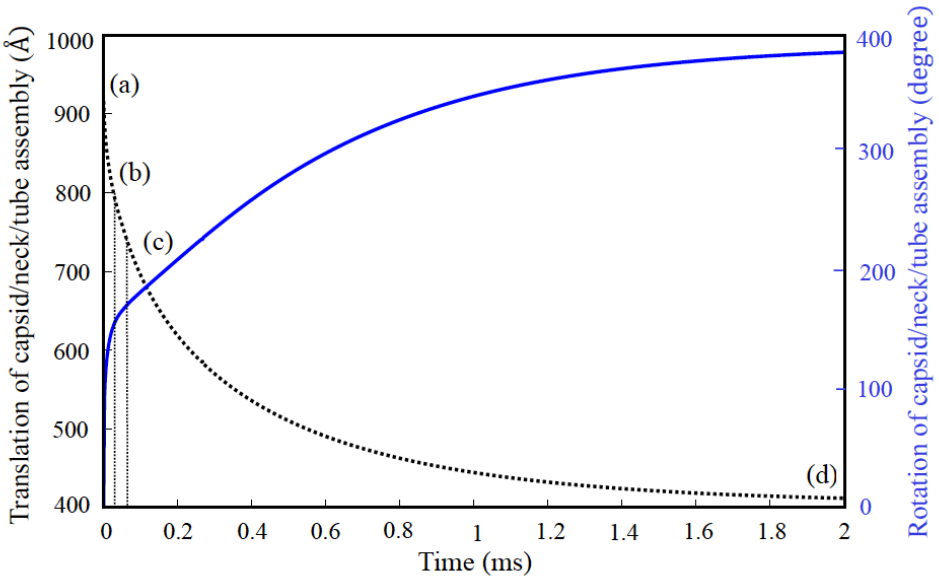

Figure 5.7: The dynamic rotation and translation of the capsid/neck/tail tube assembly during the injection process. Solid curve illustrates the rotation and dashed curve illustrates the translation. The injection machinery at states (a), (b), (c) and (d) are illustrated in Fig. 4a-d, respectively. Note, in this simulation, $\eta_w = 30$ Pa. s and $\bar{\eta}_{int} = 0.005$ Pa. s.

5.2.3 Dissipation controls the timescale of the injection process

We also employ the model to explore the overall timescale of sheath contraction from the extended state to the contracted state; another important characteristic of the injection process that has so far eluded experimental determination. This timescale is highly dependent on the dominant energy dissipation mechanism. At one extreme, the model predicts an injection timescale of only several microseconds if the only source of dissipation is the hydrodynamic drag on the capsid and sheath; refer to [42]. However, such a short time scale is highly unlikely given the overriding influence of the other dissipation mechanisms considered herein and, as emphasized above, the hydrodynamic drag on the capsid/sheath remains only of secondary or lesser importance.

For instance, upon adding cell-tail tube interaction to the dynamic model, the timescale of the injection process increases to 40 μs as this dissipation mechanism is significantly greater than the hydrodynamic drag on the capsid and sheath. However, this increased time scale is still likely far too short. The main question is what is the likely range of the time scale given the acknowledged uncertainties in the parameters η_w and $\bar{\eta}_{int}$ for the two dominant dissipation mechanisms described above? To address this, we first explore how the injection time scale varies over the broad ranges $0.001 < \eta_w < 1000$ Pa.s and $0.005 < \bar{\eta}_{int} < 5$ Pa.s. Over these ranges, the computed injection time varies from the microsecond scale to a hundred milliseconds. In particular, for $\eta_w < 10$ Pa. s, the injection time remains approximately on the order of microseconds for all values of $\bar{\eta}_{int}$. By contrast, for η_w > 10 Pa.s, the injection time rapidly grows to the millisecond time scale; refer to Figure 5.8. In this range ($\eta_w > 10$ Pa. s), the dominant energy dissipation mechanism derives from sheath-tail tube friction (STTF) as discussed above.

Next, we focus on the parameter range that yields likely injection times by taking a cue from experimental results. While there are presently no experimental results that resolve the injection time for T4, there are data for the Type VI secretion system (T6SS), which is a headless, contractile tail system used to inject toxic effectors into competing bacterial cells [82], and which has a similar molecular architecture with the T4 contractile tail. Recent experiments on T6SS report that the timescale of sheath contraction is ~5 ms [83]. Despite obvious morphological differences between phage T4 and T6SS (head versus headless) and the injected material (DNA versus toxic effectors), their actual injection machineries possess remarkable similarities. Both injection machineries possess a long rigid tail tube surrounded by an elastic sheath that is formed by six interacting helical protein strands. Furthermore, both sheaths power the injection process by contracting from high-energy extended states to low-energy contracted states [82]. Given these

significant structural similarities of the injection machineries, one might also anticipate similar injection times. Proceeding under that assumption, we identify the region within Figure 5.8 that yields similar injection times; refer to region in red (defined by an injection time of 5 ms).

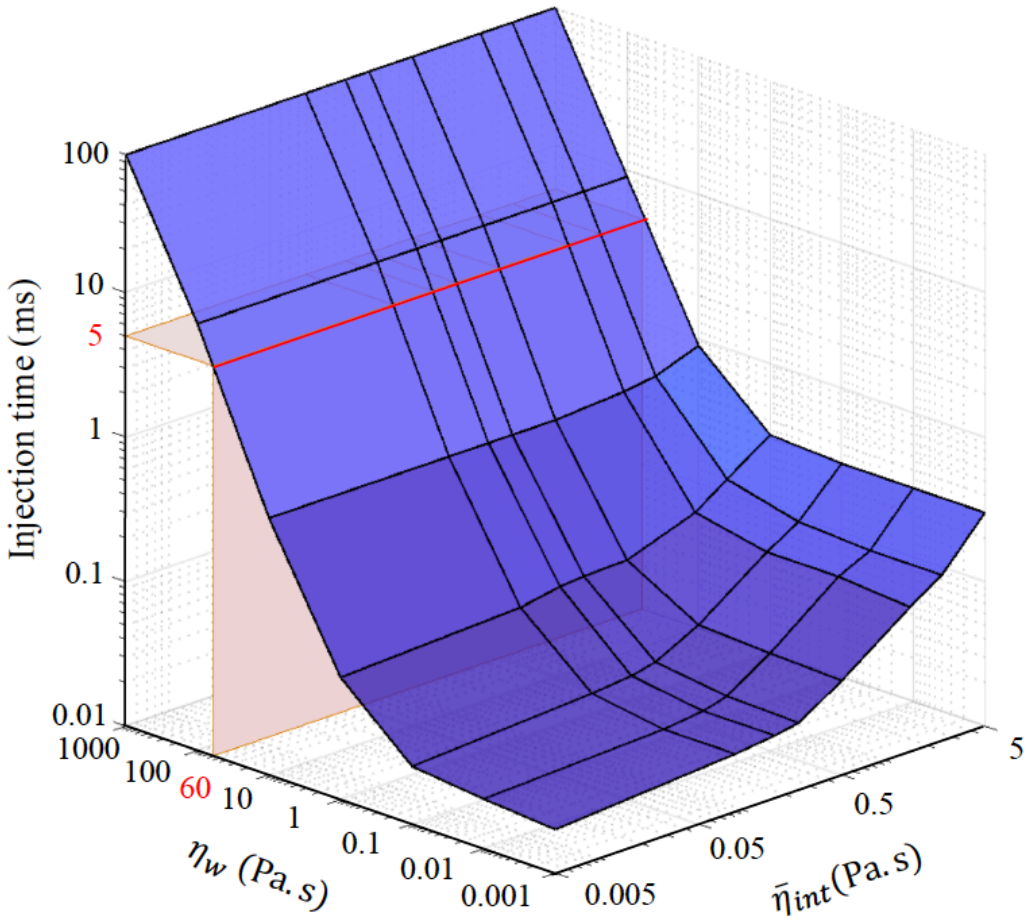

Figure 5.8: The timescale of the injection process as a function of the sheath-tube gap viscosity coefficient η_w over the range $0.001 < \eta_w < 1000$ Pa. s and the internal friction coefficient $\bar{\eta}_{int}$ over the range $0.005 < \bar{\eta}_{int} < 5$Pa. s. Note log scales. Red region defines a likely injection time scale for T4 (approximately 5 ms) by drawing a comparison with that of the Type VI secretion system (T6SS) [83].

If we assume that the timescales of sheath contraction for phage T4 and T6SS are approximately the same, then the corresponding value for η_w would be ~ 60 Pa. s (see Figure 5.8) which is approximately four orders of magnitude greater than the viscosity of bulk water (0.001 Pa.s), yet substantially below the extreme value (1000 Pa.s) for nano-scale layers with highly hydrophilic surfaces [56]. In this region, the internal energy dissipation exerts only weak influence on the injection time (see the red line in Figure 5.8 which remains largely insensitive across the range $0.005 < \bar{\eta}_{int} < 5$ Pa.s). Thus, the energy dissipation from the sheath-tail tube friction (STTF) emerges as the likely dominant dissipation mechanism controlling the injection time scale.

5.3 Reflections on system-level model

In the system-level model of phage T4, we simulate each strand of the sheath as an elastic rod with the remainder of virus captured by the upper and lower boundary conditions of the rods (strands). In doing so, we sacrifice atomistic details of the sheath to arrive at a continuum-level model that simulates, for the first time, the dynamics of the entire phage T4 injection machinery interacting with a host cell. We employ nonlinear rod theory (Kirchhoff rod theory) to describe the large conformational changes of the sheath strands during contraction.

Two competing sources of energy control the dynamics of the injection machinery; namely, 1) the strain energy stored in the extended sheath that drives injection process, and 2) the mechanisms that dissipate energy during sheath contraction. We identify and model four mechanisms that contribute to energy dissipation; namely, 1) the hydrodynamic drag on the capsid and sheath from the surrounding fluid, 2) the interaction between the tail tube and the host cell, 3) the friction between the tube and the sheath within the separating nanoscale water gap, and 4) the

internal dissipation of the sheath strands due to sliding of the gp18 subunits over each other during contraction. This system-level model of phage T4 interacting with a host requires many geometrical and material parameters that describe the major structures of phage T4 and the host cell membrane. In the following we review these major parameters and their limitations.

As mentioned above, the six interacting strands of sheath are modeled as six helical rods. The strain energy in the extended sheath that drives injection process can be calculated from the elastic energy stored in the six elastic rods; see Eq. (3.11). This elastic energy depends on the intrinsic curvature/twist of the rods and the bending and torsional elastic stiffness constants. We assumed that the contracted sheath defines the intrinsic curvature/twist of the rods and these are readily computed from the known structure of the contracted sheath. The unknown elastic stiffness constants of the sheath strands are estimated from MD simulations of a portion of the sheath and in only two conformations; namely, the extended and contracted conformations. The resulting elastic constants represent the limiting elastic constants expected during sheath contraction. Following the wave propagation mechanism proposed by Moody [28], we similarly propose a non-homogenous model for the elastic stiffness constants for intermediate sheath conformations. In particular, the non-homogenous model recognizes that the elastic constants near the baseplate will quickly transition from those of the extended to the contracted conformation while those near the neck will transition far more slowly. Future experiments using optical tweezers or magnetic tweezers may provide experimental estimates for the stiffness properties of the sheath, and thus improved estimates of the sheath strain energy that drives the injection process as well as models that capture the wave propagation mechanism.

We also reflect on the four energy dissipation mechanisms enumerated above. The first two mechanisms (cases #1 and #2) are reasonably well-established whereas the latter two (cases

#3 and #4) are not. The most uncertain parameters for the latter two include the viscosity of water in the nano-scale gap between the sheath and the tail tube (η_w) and the internal friction coefficient for the sheath strands ($\bar{\eta}_{int}$). To explore the dynamics of the injection machinery, we select the broad ranges of values for η_w and $\bar{\eta}_{int}$ drawing from similar case studied in literature. The results reveal that the time scale of the injection process depends on η_w and $\bar{\eta}_{int}$ and that it can range from a few microseconds to a hundred milliseconds. Future experiments on the internal friction of sheath strands during the large conformational changes from the extended state to the contracted state as well as measuring the viscosity of water in the gap between highly hydrophilic surfaces of sheath and tail tube are clearly warranted and would guide the selection of these two parameters.

5.4 Conclusions

In this chapter, we assemble and solve a complete system-level dynamic model to simulate the phage T4 injection machinery from the high-energy extended state to the low-energy contracted state. To our knowledge, this is the first model that is capable of estimating the energetics, pathway and time-scale of the injection process for this and similar contractile systems.

This unique model derives from constituent parts that span atomistic- to continuum-level representations. The bending and torsional stiffness constants for the helical strands of gp18 that form the elastic sheath are derived from equilibrium MD simulations by the Andricioaei group at the University of California at Irvine. We employ those stiffness constants in a continuum model of the elastic sheath composed of six interacting helical strands of gp18 by representing each strand as a non-homogenous elastic rod with configuration-dependent elastic constants. The rigid body motion of the attached capsid/neck/tail tube assembly is captured through a boundary condition

for the helical strands and it models the assembly as it translates along and rotates about the tail tube axis. The model also incorporates four potential sources of energy dissipation including; 1) hydrodynamic drag on the sheath strands and the capsid from the surrounding water, 2) internal (material) dissipation of the sheath strands due to their large conformational change during sheath contraction, 3) tail tube-cell interaction both prior to and following the rupture of the host cell membrane, and 4) the sheath-tube friction during sheath contraction. Simulations reveal the nonlinear dynamics of the sheath from its extended conformation before injection to its contracted conformation after injection, the companion rigid body translation and rotation of the attached capsid/neck/tail tube assembly, and the indentation and rupture of the host cell membrane.

The model estimates that the injection process is driven by approximately 14500 kT of elastic energy stored in the extended sheath. This estimate is consistent with the experimentally reported enthalpy of sheath contraction [25]. The dynamical pathway underlying the injection process takes the form of a contraction wave that propagates from the baseplate to the neck as revealed in Figure 5.6 and as previously hypothesized [28,29]. The simulated conformations of T4 during contraction are consistent with the experimental micrographs of extended, partially contracted, and fully contracted particles observed in *in vitro* experiments [28] and they also provide further potential starting points for future, detailed free energy calculations at the atomic level. Dynamic sheath contraction induces initial rapid translation and rotation of the tail tube (and capsid) to rapidly generate the forces needed to rupture the outer membrane of the host cell. Indeed, the model estimates that rupture arises when the tip of the tail tube exerts a force of approximately 330 pN and at a membrane indentation of approximately 60 Å. The model enables broad exploration of the four energy dissipation mechanisms and doing so reveals the mechanisms (and parameter ranges) that control the overall time scale of the injection process. In particular, injection

times on the millisecond time scale (and as observed for the analogous T6SS [83]) are controlled by sheath-tail tube friction.

The modeling approach can be leveraged in the future to describe the dynamics of other nanoscale injection machines that are powered by contractile sheath structures. Prime examples include the R2 pyocin and phage Phi812 described briefly in Chapter 6. Rather remarkably, all of these share the same feature with phage T4 in possessing a contractile sheath structure formed by six interacting helical protein strands.

Chapter 6

Summary, major contributions, and future work

6.1 Summary and major contributions

Bacteriophage T4 from the family *Myoviridae* is one of the most complex tailed viruses that infects *E. coil* (*Escherichia coli*) by injecting its genome into the host cell using a highly efficient contractile injection machinery. Since bacteriophages are highly efficient genome delivery machines, understanding their structure and function continues to attract considerable research attention because of implications for future nanotechnology devices for DNA transfection and for experimental phage therapies. Indeed, emerging bio-nanotechnologies exploit phage injection machinery for the detection and control of pathogens, for peptide display and for phage therapy as an alternative to antibiotics. A large number of studies have contributed to our understanding of bacteriophage T4 structure including the components of the injection mechanism. Despite the wealth of data available on the structure of T4 using cryo-EM and x-ray crystallography, we lack a fundamental understanding of how this intricate machinery works in real-time including the dynamics, energetics, and time scale of the injection process. Our lack of knowledge is partly attributed to the paucity of experiments that aim to measure the dynamics and/or energetics of the injection process

This dissertation contributes the first system-level model of bacteriophage T4 interacting with a host cell that predicts the global dynamics of the intriguing and complex injection machinery by simulating all aspects that control its behavior. In particular, the system model predicts the dynamical pathway of sheath contraction in the form of a contraction wave, the energy that powers the injection machinery, the forces responsible for piercing the host cell membrane, and the energy dissipation that controls the time scale of the injection process.

The dynamic model of the phage T4 injection machinery interacting with a host cell was achieved through a four-step modeling process. We first proposed the dynamic model of a single strand contractile injection machinery (Chapter 2) where the strand was modeled as a continuum rod connecting to a rigid body representing the capsid/DNA/tail tube. The single strand model is then employed as a building block to create the six strand contractile injection machinery of phage T4 (Chapter 3). The resulting continuum model for the elastic sheath employed elastic constants determined from molecular dynamics simulations conducted by Andricioaei group at the University of California-Irvine. The dynamics of the injection process is governed by the competition between two energetic processes; namely, the stored energy of the flexible sheath that powers the injection and the dissipation mechanisms that retard the injection dynamics. We followed by proposing model for four potential dissipation mechanisms during the injection process including; the hydrodynamic dissipation on the capsid and sheath from the surrounding environment, the internal dissipation of the sheath strands, the dissipation from the host cell membrane interacting with the tip of the tail tube, and the hydrodynamic interaction between the sheath and the tail tube (Chapter 4). The complete dynamic model of phage T4 is fully developed (Chapter 5) by incorporating the four dissipation mechanisms (Chapter 4) into the dynamic model of the six strand injection machinery (Chapter 3). The new findings and major conclusions drawn

from this system model are as follows.

The model estimates that the injection process is driven by approximately 14500 kT of elastic energy stored in the extended sheath. This estimate is consistent with the experimentally reported enthalpy of sheath contraction [25]. The dynamical pathway underlying the injection process takes the form of a contraction wave that propagates from the baseplate to the neck as previously hypothesized [28,29]; refer to Chapter 5. The simulated conformations of T4 during contraction are consistent with the experimental micrographs of extended, partially contracted, and fully contracted particles observed in *in vitro* experiments [28] and, as noted by our collaborators, they also provide further potential starting points for future, detailed free energy calculations at the atomic level. The model estimates that rupture arises when the tip of the tail tube exerts a force of approximately 330 pN and at a membrane indentation of approximately 60 Å. The model enables broad exploration of the four energy dissipation mechanisms and doing so reveals the mechanisms (and parameter ranges) that control the overall time scale of the injection process. In particular, injection times on the millisecond time scale (and as observed for the analogous T6SS [26]) are controlled by sheath-tail tube friction.

Another important contribution of this dissertation is a new theory for describing the internal friction of general biofilaments (Chapter 4), including the protein strands composing the sheath. This theory broadly applies to other biofilament structures including chromosomal fragments, actin filaments, and microtubules as promising examples. A novel feature of this new theory is the incorporation of the shear deformation of filaments which was ignored in prior theories and its inclusion resolves previous paradoxes in the experimental results on thermally fluctuating chromosomal fragments and microtubules.

Finally, the system model resulting from this dissertation may be further expanded to explore how other contractile tail-driven injection machineries work, such as R-pyocins and bacteriophage phi812 as described next.

6.2 Future work

As described in detail in the previous chapters, bacteriophage T4 from the family *Myoviridae* infects *E. coli* by injecting its genomic DNA into the bacterial host using a long, contractile injection machine; see, for example, Figure 1.3. Besides phage T4, there are other biological systems which possess similar contractile nano-injection machineries that evolved to pierce the membrane of a host cell and to deliver DNA, protein, or ions through a needle-like conduit. Two intriguing classes of such systems, whose atomic-level structures are also known, are phi812 and R2-pyocins.

Bacteriophage phi812, also from the family *Myoviridae*, infects the *Staphylococcus aureus* cell by injecting its genomic DNA from the capsid into the host. Similar to phage T4, phi812 consists of a long contractile tail assembly which connects to a multi-protein capsid containing the genomic DNA; see Figure 6.1(a). The tail assembly, which is responsible for transferring DNA from capsid to the host, again consists of a long rigid tube surrounded by a contractile sheath. The tail sheath attaches to the capsid by a neck (collar) at the upper end and to the baseplate at the lower end (Figure 6.1(a)).

Unlike T4 and phi814, R2-pyocin, produced by *P. aeruginosa*, attacks competing bacteria by channeling protons through their tail structure inside the competing bacteria and thereby

dissipating their membrane potential. R2-pyocin is a headless and DNA-free injection machine [84,85], but its long contractile tail assembly remains quite similar to that of phage T4 and Phi812. As illustrated in Figure 6.1(b), it consists of a tail tube surrounded by a sheath, a collar at the upper end, and a baseplate at the lower end of the tail.

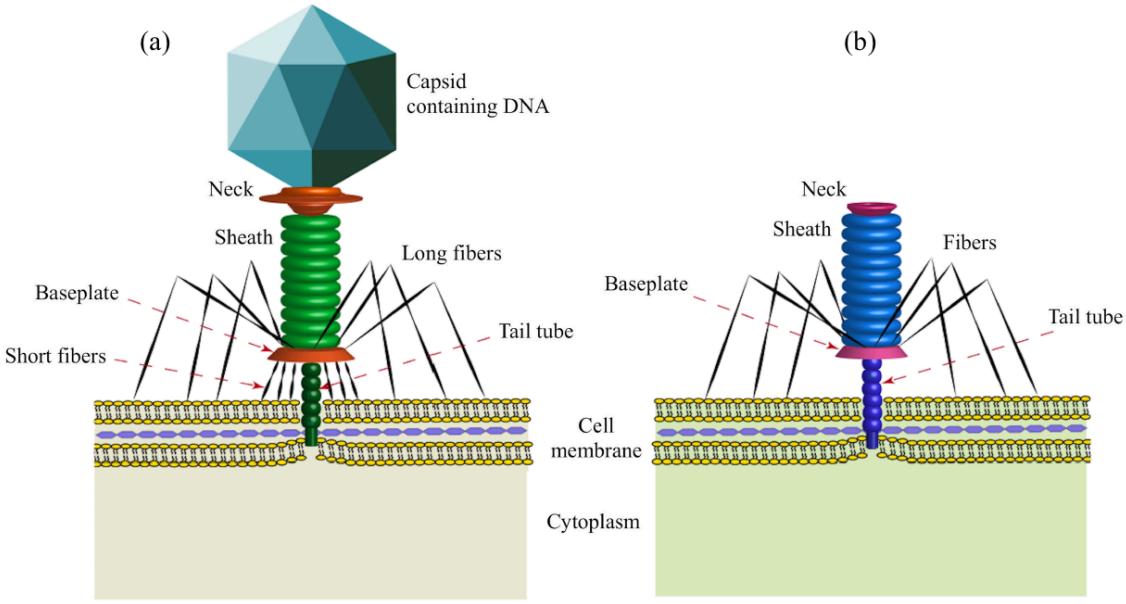

Figure 6.1: Schematic of (a) bacteriophage Phi812 and (b) R2-pyocin piercing a host cell membrane (not to scale). Major components of the contractile tail assembly are illustrated.

Despite many differences in biology, protein composition and targets among these injection machineries (phage T4, phage Phi812, and R2-pyocin), their distinct evolutionary pathways, and the distinctly different injected material (DNA vs. protons), these machineries share the same essential structure: a contractile (energy storing) sheath composed of six helical strands that drives the injection process. During contraction, the sheaths undergo a large conformational

change from an extended (high-energy) state to a contracted (low-energy) state, reducing to about half of their initial length and significantly increasing their diameter. The sheath monomer subunits largely translate and rotate as rigid bodies without significant changes in monomer structure from the extended to contracted conformations [84].

Significant research interest has been devoted over the past decades towards understanding the function of contractile nanomachines, and with potential bio-nanotechnological applications ranging from the detection and control of pathogens and peptide display, to experimental phage therapy, and to generating novel bactericidal protein complexes. And while there exists extensive structural data for both Phi812 and R2-pyocin (and in both the extended and contracted states), little is known about their intermediate states or the dynamics that underlie their injection processes. Ge et al. estimate the free energy of R2-pyocin contraction using PISA [86], but experimental corroboration of predicted energies are lacking for both Phi812 and R2-pyocin.

In future work, we aim to extend the modeling approach developed for phage T4 to simulate the dynamics and energetics of phage Phi812 and R2-pyocin. To this end, we will derive bending and torsional elastic stiffness constants of a helical sheath strand of phage Phi812 and R2-pyocin, in both the pre- (extended) and post-contraction (contracted) states, from MD simulations of about one-fifth of the complete sheaths. These estimated stiffness constants will again be incorporated into a continuum model of the sheath to ultimately simulate the injection process.

To simulate the dynamics of Phi812 and R2-pyocin, we will employ the modeling approach proposed in this dissertation for phage T4. In doing so, we simulate the six strands of the sheath as six elastic rods, and then model the remaining structures as the upper boundary conditions and lower boundary conditions of the sheath strands. For Phi812, the baseplate is modeled as the lower boundary conditions and the capsid/DNA/neck/tail tube assembly is modeled as the upper

boundary conditions. Similarly, for R2-pyocin, the baseplate defines the lower boundary conditions and the neck/tail tube assembly is modeled as the upper boundary conditions of the sheath strands.

Similar to phage T4, the strain energy stored in the sheaths of Phi812 and R2-pyocin drives these injection machineries. Similarly, the four mechanisms discussed in Chapter 4 dissipate energy during the injection process. In addition to differing geometrical and material properties of the injection machineries and their hosts, the main differences in the dynamic models of Phi812 and R2-pyocin is the first energy dissipation mechanism discussed in Chapter 4; namely, the hydrodynamic drag on the injection machinery from surrounding fluid. R2-pyocin is headless (no capsid) and so only the sheath is subject to hydrodynamic drag. However, Phi812 has a massive capsid, and similar to phage T4, there is hydrodynamic drag on both the capsid and the sheath strands. Accordingly, the energy dissipation due to hydrodynamic drag for R2-pyocin will be smaller than that for Phi812 and phage T4. However, the results for phage T4 also reveal that this hydrodynamic drag remains of lesser importance than the three other sources of energy dissipation and it does not have a significant effect on the time scale of the injection process.

Future dynamic model of Phi812 and R2-pyocin enable us to compare the energetics, dynamic pathways, and timescales of the injection process for all three systems (phage T4, phage Phi812, and R2-pyocin) to reveal significant differences and similarities in their function and structures.

Appendices

Appendix A: Non-dimensional parameters

Nondimensional parameters defined in Chapter 2 are

$$\boldsymbol{f} = \left(\frac{m_s L^2}{p_0^2}\right)\bar{\boldsymbol{f}}, \qquad \boldsymbol{F} = \left(\frac{m_s L}{p_0^2}\right)\bar{\boldsymbol{F}}, \qquad \boldsymbol{q} = \left(\frac{m_s L^3}{p_0^2}\right)\bar{\boldsymbol{q}}, \qquad \boldsymbol{Q} = \left(\frac{m_s L^2}{p_0^2}\right)\bar{\boldsymbol{Q}},$$

$$\boldsymbol{\nu} = \left(\frac{L}{p_0}\right)\bar{\boldsymbol{\nu}}, \qquad \boldsymbol{\omega} = \left(\frac{1}{p_0}\right)\bar{\boldsymbol{\omega}}, \qquad \boldsymbol{\kappa} = \left(\frac{1}{L}\right)\bar{\boldsymbol{\kappa}}\,, \qquad \boldsymbol{I}_s = (m_s L^2)\bar{\boldsymbol{I}}_s\,, \tag{A1}$$

$$I_c = \left(\frac{m_s L^4}{p_0^2}\right)\bar{I}_c, \qquad \boldsymbol{B} = \left(\frac{m_s L^4}{p_0^2}\right)\bar{\boldsymbol{B}}, \quad U_e = \left(\frac{m_s L^3}{p_0^2}\right)\bar{U}_e, \qquad C_r = \left(\frac{m_s L^3}{p_0}\right)\bar{C}_r,$$

$$C_t = \left(\frac{m_s L}{p_0}\right)\bar{C}_t$$

Appendix B: Homogeneous and isotropic rod assumptions

In this study, each of the six strands of gp18 is modeled as a homogeneous and isotropic elastic rod but with configuration-dependent elastic constants; refer to Table 3.1. The assumption of homogeneity is quite reasonable based on the uniform contraction theory of the sheath in which all gp18 subunits rotate and translate simultaneously by the same amount. (However, we also recognize a competing theory that assumes that the sheath contraction evolves as a propagating wave. [26,27]) The assumption of isotropy is considered in reference to Fig. A1, which illustrates the MD time-averaged mass density plot of a complete ring of the T4 sheath composed of (a portion of) all six strands. Inspection of Fig. A1 suggests some degree of bending stiffness anisotropy within each strand cross section. However, these differences at the strand level become unimportant when considering the bending of the assembled sheath that is the aggregate of the six coupled strands. Note that the assembled sheath (Figure 3.1) is a near-axisymmetric structure (six-fold symmetry) and thus possesses minimal bending anisotropy. In other words, any anisotropy at the strand level averages to isotropic behavior at the sheath level. This isotropic behavior of the sheath can just as well be captured using an isotropic strand model, provided the strand model employs an average bending stiffness constant (for the strand cross section). We estimate this average bending stiffness constant from Equation (3.1) for both the extended and the contracted

conformations as reported in Table 3.1.

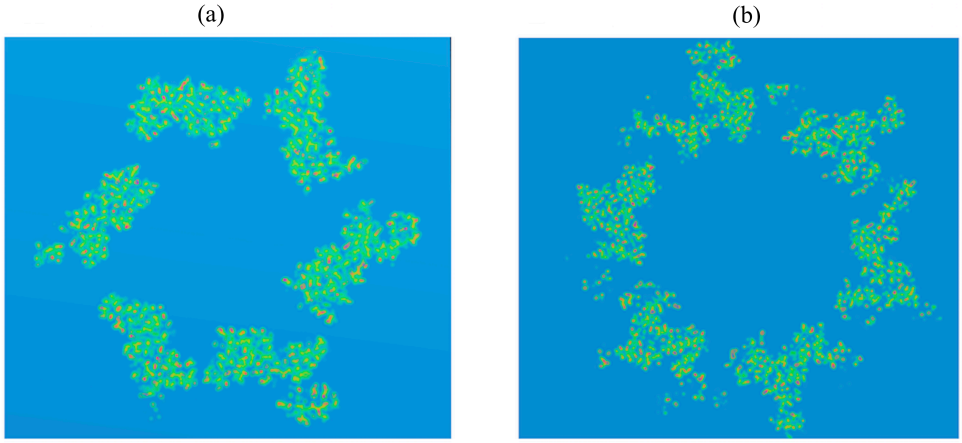

Figure A 1: Given here is a schematic of the time-averaged mass density for the cross section of a single ring of the T4 sheath in (a) the extended state and (b) the contracted state. Figure provided by Andricioaei group, UC-Irvine.

Appendix C: RMSD individual sheath strands

Fig. A2 provides the atomistic RMSD for each of the six helical strands in both extended and contracted states.

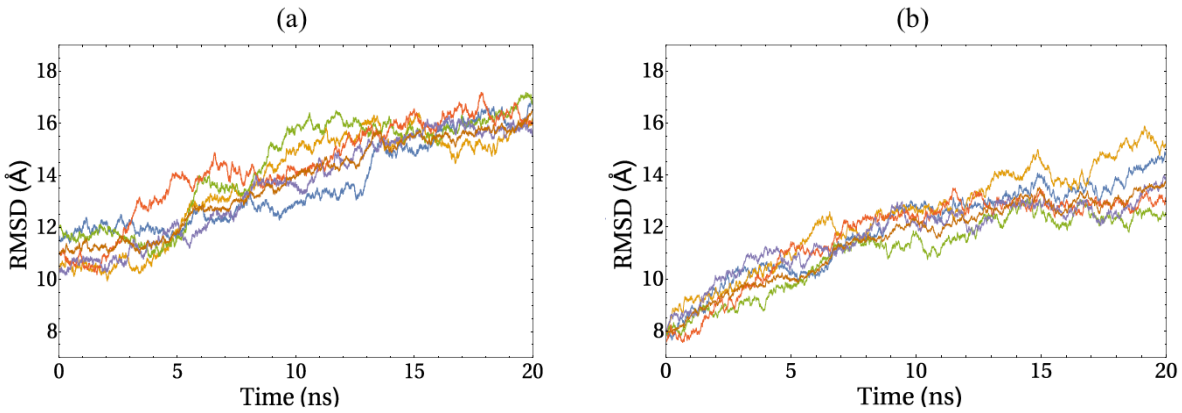

Figure A 2: Shown here are the atomistic RMSDs from the initial unequilibrated structure for each of the six individual helical strands for the (a) extended and (b) contracted states during the 20 ns production run. Different colors denote different strands. Figure provided by Andricioaei group, UC-Irvine.

Appendix D: Geometrical and material properties of bacteriophage T4 for Chapter 3

Table A1 provides a summary of the geometrical and material parameters for the dynamical model of T4.

Table A 1: Geometrical and material properties of bacteriophage T4 used in the dynamic model of sheath contraction.

Geometrical/Material properties	Contracted state	Extended state
Bending stiffness of sheath strand, A (10^{-27}N.m2)	35.5	26
Torsional stiffness of sheath strand, C (10^{-27}N.m2)	222	6.56
Mass density of subunit gp18, ρ (kg/m3)	1130	1130
Mass of each subunit gp18 (kDa)	71.2[2]	71.2
Mass of capsid/DNA/neck/tail tube, m_c (MDa)	1.971	1.971
Arc length of sheath strand, L (Å)	1483.5	1079.8

Radius of neck/baseplate, r (Å)	112.66	84.45
Height of sheath, H(Å)	420	925
Radius of rod (sheath strand), R_s (Å)	22.72	26.64
Number of sheath strand turns, n	2.01	1.05
Height of capsid, l(Å)	1195	1195
Radius of capsid, R_c(Å)	430	430

Appendix E: Internal friction for thermally fluctuating biofilaments

Background on Timoshenko beam model for thermally fluctuating biofilaments:

We propose a theory for thermally fluctuating that captures both shear and bending deformation effects per Timoshenko beam theory. The governing Equations (4.12) and (4.13) are deduced from Hamilton's Principle

$$\int_{t_1}^{t_2} \delta(-V + W_{th} - W_{ex} - W_{in})\mathrm{d}t = 0 \tag{A2}$$

in which the elastic energy V and work by random thermal noise n are

$$V = \int_0^L \frac{1}{2} B \left(\frac{\partial \varphi}{\partial x}\right)^2 \mathrm{d}x + \int_0^L \frac{1}{2} \kappa S \left(\frac{\partial u}{\partial x} - \varphi\right)^2 \mathrm{d}x \tag{A3}$$

$$W_{th} = \int_0^L n(x,t) u \mathrm{d}x \tag{A4}$$

Here, $\frac{\partial u}{\partial x}$ is the total rotation of the cross section of the biofilament due to bending and shear deformations and φ is the component due to bending alone. The quantities W_{ex} and W_{in} denote energy dissipated by external friction (hydrodynamic drag) and internal friction, respectively

which are introduced in (A2) using Rayleigh dissipation functions. The rate of energy dissipation due to hydrodynamic drag is

$$\dot{E}_{ex} = \int_0^L \frac{1}{2}\eta \left(\frac{\partial u}{\partial t}\right)^2 \mathrm{d}x \tag{A5}$$

which, employing the Rayleigh dissipation function, results in

$$\int_{t_1}^{t_2} \delta W_{ex}\, dt = \int_{t_1}^{t_2} \frac{\partial \dot{E}_{ex}}{\partial \dot{u}}\, \delta u dt \tag{A6}$$

Similarly, the rate of energy dissipation due to internal friction is

$$\dot{E}_{in} = \int_0^L \frac{1}{2}\eta_b' I \left(\frac{\partial \dot{\varphi}}{\partial x}\right)^2 dx + \int_0^L \frac{1}{2}\eta_s' A \left(\frac{\partial \dot{u}}{\partial x} - \dot{\varphi}\right)^2 dx \tag{A7}$$

in which the first and second terms capture the rates of energy dissipation due to bending deformation and shear deformation, respectively. Note the structure of (A7) that is analogous to that of the elastic energy (A3). Employing the associated Rayleigh dissipation function results in

$$\int_{t_1}^{t_2} \delta W_{in}\, \mathrm{d}t = \int_{t_1}^{t_2} \left\{ \frac{\partial \dot{E}_{in}}{\partial\left(\frac{\partial \dot{\varphi}}{\partial x}\right)}\, \delta\left(\frac{\partial \varphi}{\partial x}\right) + \frac{\partial \dot{E}_{in}}{\partial\left(\frac{\partial \dot{u}}{\partial x} - \dot{\varphi}\right)}\, \delta\left(\frac{\partial u}{\partial x} - \varphi\right) \right\} \mathrm{d}t \tag{A8}$$

Substituting (A3)-(A8) into Hamilton's Principle (A2) and integrating by parts results in the following Langevin formulation ((4.12) and (4.13) in the paper)

$$B\frac{\partial^2\varphi}{\partial x^2}+\kappa S\left(\frac{\partial u}{\partial x}-\varphi\right)+\eta_b' I\frac{\partial^3\varphi}{\partial x^2\partial t}+\eta_s' A\left(\frac{\partial^2 u}{\partial x\partial t}-\frac{\partial\varphi}{\partial t}\right)=0 \tag{A9}$$

$$\kappa S\left(\frac{\partial\varphi}{\partial x}-\frac{\partial^2 u}{\partial x^2}\right)+\eta_s' A\left(\frac{\partial^2\varphi}{\partial x\partial t}-\frac{\partial^3 u}{\partial x^2\partial t}\right)+\eta\frac{\partial u}{\partial t}=n(x,t) \tag{A10}$$

Note that if the shear deformation effect is neglected, the total rotation of cross section is due to bending alone is described by the constraint $\frac{\partial u}{\partial x}=\varphi$. Upon employing this constraint, the Eqns. (A3) and (A7)-(A8) reduce, respectively, to

$$V=\int_0^L\frac{1}{2}B\left(\frac{\partial^2 u}{\partial x^2}\right)^2\mathrm{d}x \tag{A11}$$

$$\dot{E}_{in}=\int_0^L\frac{1}{2}\eta_b' I\left(\frac{\partial^2\dot{u}}{\partial x^2}\right)^2 dx \tag{A12}$$

$$\int_{t_1}^{t_2}\delta W_{in}\,\mathrm{d}t=\int_{t_1}^{t_2}\left\{\frac{\partial\dot{E}_{in}}{\partial\left(\frac{\partial^2\dot{u}}{\partial x^2}\right)}\,\delta\left(\frac{\partial^2 u}{\partial x^2}\right)\right\}\mathrm{d}t \tag{A13}$$

In this limit, Timoshenko theory reduces to the Euler-Bernoulli theory employed in WLC model. Substitution of (A4)-(A6)and (A11)-(A12) into (A2) yields

$$B\frac{\partial^4 u}{\partial s^4}+\eta\frac{\partial u}{\partial t}+\eta_b' I\frac{\partial}{\partial t}\frac{\partial^4 u}{\partial x^4}=n(s,t) \tag{A14}$$

as expected.

If the internal friction is neglected ($\eta_s'=\eta_b'=0$), equations (A9)-(A10) reduce to ((4.21) and (4.22) in the paper)

$$B\frac{\partial^2\varphi}{\partial x^2} + \kappa S\left(\frac{\partial u}{\partial x} - \varphi\right) = 0 \tag{A15}$$

$$\kappa S\left(\frac{\partial \varphi}{\partial x} - \frac{\partial^2 u}{\partial x^2}\right) + \eta\frac{\partial u}{\partial t} = n(x,t) \tag{A16}$$

Derivation of relaxation time constants:

The Fourier transform of (A9) and (A10) with respect to space and time yields

$$\Phi_{q\omega}\left((-Bq^2 - \kappa S) + i(\eta_b' I\omega q^2 + \eta_s' A\omega)\right) + U_{q\omega}(\eta_s' A\omega q + i\kappa S q) = 0 \tag{A17}$$

$$\Phi_{q\omega}(\eta_s' A\omega q + i\kappa S q) + U_{q\omega}\left(\kappa S q^2 + i(-\eta_s' A\omega q^2 - \eta\omega)\right) = N_{q\omega} \tag{A18}$$

in which ω and q denote the frequency and wavenumber of propagating waves, respectively and $U_{q\omega}$, $\Phi_{q\omega}$, and $N_{q\omega}$ denote the (double) Fourier transforms of the transverse displacement u, the rotation φ, and the random thermal noise n, respectively.

Solution of $U_{q\omega}$ yields

$$U_{q\omega} = \frac{\mathrm{A}+i\mathrm{B}}{\mathrm{C}+i\mathrm{D}} N_{q\omega} \tag{A19}$$

with

$$\mathrm{A} = Bq^2 + \kappa S \tag{A20}$$

$$\mathrm{B} = -\omega(\eta_b' I q^2 + \eta_s' A)$$

$$\mathrm{C} = (\eta_s' A\omega q)^2 - (\kappa S q)^2 + \kappa S q^2(Bq^2 + \kappa S) - (\eta_s' A\omega q^2 + \eta\omega)(\eta_b' I\omega q^2 + \eta_s' A\omega)$$

$$\mathrm{D} = 2(\eta_s' A\omega q)(\kappa S q) - \kappa S q^2(\eta_b' I\omega q^2 + \eta_s' A\omega) - (\eta_s' A\omega q^2 + \eta\omega)(Bq^2 + \kappa S)$$

The power spectral density for u follows from

$$\langle {U_{q\omega}}^2 \rangle = \frac{\mathrm{A}^2 + B^2}{\mathrm{M}\omega^4 + \mathrm{N}\omega^2 + \mathrm{P}} \langle {N_{q\omega}}^2 \rangle \tag{A21}$$

with

$$\mathrm{M} = (\eta_s' \eta_b' A I q^4 + \eta_b' \eta I q^2 + \eta_s' \eta A)^2$$

$$\mathrm{N} = q^8((\eta_s' AB)^2 + (\eta_b' I\kappa S)^2) + q^6(2\eta_s' \eta AB^2) + q^4(2\eta\eta_b' I(\kappa S)^2 + (B\eta)^2) + q^2(2\kappa SB\eta^2) + (\kappa S\eta)^2 \tag{A22}$$

$$\mathrm{P} = q^8(\kappa SB)^2$$

The time autocorrelation function $\mathcal{R}(T)$ for u follows from the inverse Fourier transform of (A21) with respect to ω in which one assumes ideal (white) random thermal noise which yields ((4.16) and (4.17))

$$\mathcal{R}(T) = R_1 \exp\left(\frac{-T}{\tau_1}\right) + R_2 \exp\left(\frac{-T}{\tau_2}\right) \tag{A23}$$

$$\tau_1 = \sqrt{\frac{2\mathrm{M}}{\mathrm{N} + \sqrt{\mathrm{N}^2 - 4\mathrm{MP}}}}, \quad \tau_2 = \sqrt{\frac{2\mathrm{M}}{\mathrm{N} - \sqrt{\mathrm{N}^2 - 4\mathrm{MP}}}} \tag{A24}$$

with

$$R_1 = \frac{2k_B TL(Bq^2 + \kappa S)}{\kappa SBq^4} \frac{R_3}{R_3 + R_4} \tag{A25}$$

$$R_2 = \frac{2k_B TL(Bq^2 + \kappa S)}{\kappa SBq^4} \frac{R_4}{R_3 + R_4} \tag{A26}$$

$$R_3 = \frac{(\eta_b' Iq^2 + \eta_s' A)^2 - {\tau_1}^2 (Bq^2 + \kappa S)^2}{2L({\tau_2}^2 - {\tau_1}^2)} \tau_1 {\tau_2}^2 \tag{A27}$$

$$R_4 = \frac{{\tau_2}^2 (Bq^2 + \kappa S)^2 - (\eta_b' Iq^2 + \eta_s' A)^2}{2L({\tau_2}^2 - {\tau_1}^2)} \tau_2 {\tau_1}^2 \tag{A28}$$

If the internal friction is neglected, i.e., $\eta_s' = \eta_b' = 0$, the Fourier transforms of (A15) and (A16) with respect to space and time yield

$$\Phi_{q\omega}(-Bq^2 - \kappa S) + U_{q\omega}(i\kappa Sq) = 0 \tag{A29}$$

$$\Phi_{q\omega}(i\kappa Sq) + U_{q\omega}\left(\kappa Sq^2 + i(-\eta\omega)\right) = N_{q\omega} \tag{A30}$$

Then, the power spectral density for u follows from

$$\langle {U_{q\omega}}^2 \rangle = \frac{(Bq^2 + \kappa S)^2}{(\kappa S\eta + B\eta q^2)^2 \omega^2 + (\kappa SBq^4)^2} \langle {N_{q\omega}}^2 \rangle \tag{A31}$$

The inverse Fourier transform of (A31) with respect to ω yields the associated autocorrelation $\mathcal{R}(T)$ and relaxation time τ_d become ((4.23) and (4.24))

$$\mathcal{R}(T) = R_d \exp\left(\frac{-T}{\tau_d}\right) \tag{A32}$$

$$\tau_d = \frac{\kappa S\eta + B\eta q^2}{\kappa SBq^4} \tag{A33}$$

$$R_d = \frac{2k_B TL(Bq^2 + \kappa S)}{\kappa SBq^4} \tag{A34}$$

Appendix F: Atomistic representation of dynamic pathway of injection process

To illustrate the dynamic pathway of the injection process, we create an atomistic-level representation of the entire T4 system (see Fig. 5.6) employing the simulation results for the dynamic continuum model presented herein. The continuum model provides the dynamically changing shape of each of the six interacting strands of the sheath as well as the dynamic translation and rotation of the capsid/neck/tail tube assembly during the injection process. We superimpose atomistic representations of these elements using reported atomic structures of the T4 sheath, capsid, tail tube, and neck as described below.

The dynamic continuum model of the six interacting helical strands of the sheath yields the trajectories of the mass centers of the gp18 subunits as functions of time during the injection process. From these continuum-level trajectories, we select the sheath in three conformations; fully extended sheath, intermediate sheath, and fully contracted sheath. To start, for each conformation, the cylindrical coordinates (i.e., radius, height and polar angle) are calculated for 23 equally-spaced points along the arc length of a single helical sheath strand using the dynamic strand conformation from the continuum model. Each point corresponds approximately to the mass center a gp18 subunit within each of the 23 hexameric rings forming the sheath.

During sheath contraction, each subunit rotates by 45 degree about its radial axis and translates outward in radial direction. The structure of each ring for intermediate sheath is obtained in MATLAB by linear interpolations of the known ring structures for the fully extended (pdb id 3foh) and fully contracted (pdb id 3foi) conformations given by

$$V(j) = \frac{V_{cont} - V_{ext}}{r_{cont} - r_{ext}}(r(j) - r_{ext}) + V_{ext} \quad , \quad j = 1, 2, \dots, 23. \tag{A35}$$

In which V_{ext} and V_{cont} are the spatial coordinates of atoms for the extended and contracted rings, respectively, and r_{ext} and r_{cont} are the radiuses of the extended and contracted rings, respectively. Finally, r and V are the radius and spatial coordinates of atoms of the ring j. The rings are aligned and assembled using the height and polar angle of the points along the helical strands predicted by the continuum model. The result is an atomistic representation of the full intermediate structure of the sheath. The sheath structure is then attached to the neck, tail tube and neck to represent the structure of virus during injection process.

The atomic structure of a single ring hexamer of the tail tube is extracted from the cryo-EM structure of the entire T4 baseplate (pdb id 5iv5). The 23-ring full structure of the tail tube [21] is then constructed in MATLAB by repeatedly applying the tail tube helical parameters (helical rise and twist 40.2 Å and 17.9 degrees [24]). A fraction of neck, gp15 hexamer, is extracted from the gp15-gp18 hexamer complex (pdb id 3j2m) [46], and the atomic structure of the full icosahedral T4 capsid is obtained from the protein data bank (pdb id 5fv3) [87]. The atomic structures of the tail tube, capsid and a section of the neck (gp15 hexamer) are attached to the sheath structure to create contraction intermediates of the entire phage (minus the baseplate, tail fibers and missing sections of the neck). Within known cryo-EM resolutions, no rearrangement of

subunits of the capsid, tail tube and the neck (gp15) has been observed during contraction, and the orientation of the gp15 hexamer relative to the top of the sheath remains preserved [46]. Therefore, in the contraction intermediates, the translation and rotation of the capsid-tail tube-gp15 hexamer complex is identical to the top ring of the sheath during contraction.

The resulting intermediate structures (sheath, tail tube, capsid and fraction of neck) of phage T4 created by MATLAB are then imported in VMD to create the three snapshots provide in Fig. 5.6.

Bibliography

[1] J. M. Inal, Arch. Immunol. Ther. Exp. (Warsz). **51**, 237 (2003).

[2] S. Matsuzaki, M. Rashel, J. Uchiyama, S. Sakurai, T. Ujihara, M. Kuroda, M. Ikeuchi, T. Tani, M. Fujieda, H. Wakiguchi, and S. Imai, J. Infect. Chemother. **11**, 211 (2005).

[3] A. Fokine and M. G. Rossmann, Bacteriophage **4**, e28281 (2014).

[4] N. Chanishvili, *Phage Therapy-History from Twort and d'Herelle Through Soviet Experience to Current Approaches*, 1st ed. (Elsevier Inc., 2012).

[5] E. V. Orlova, Bacteriophages (2012).

[6] D. M. Lin, B. Koskella, and H. C. Lin, World J. Gastrointest. Pharmacol. Ther. **8**, 162 (2017).

[7] A. Sulakvelidze, Ind. Pharm. **45**, 14 (2011).

[8] S. Hagens and M. J. Loessner, Appl. Microbiol. Biotechnol. **76**, 513 (2007).

[9] V. A. Petrenko and V. J. Vodyanoy, J. Microbiol. Methods **53**, 253 (2003).

[10] H. M. E. Azzazy and W. E. Highsmith, Clin. Biochem. **35**, 425 (2002).

[11] A. Fokine, P. R. Chipman, P. G. Leiman, V. V. Mesyanzhinov, V. B. Rao, and M. G. Rossmann, Proc. Natl. Acad. Sci. **101**, 6003 (2004).

[12] P. G. Leiman, S. Kanamaru, V. V. Mesyanzhinov, F. Arisaka, and M. G. Rossmann, Cell. Mol. Life Sci. **60**, 2356 (2003).

[13] W. Baschong, C. Baschong-Prescianotto, A. Engel, E. Kellenberger, A. Lustig, R. Reichelt, M. Zulauf, and U. Aebi, J. Struct. Biol. **106**, 93 (1991).

[14] M. G. Rossmann, V. V. Mesyanzhinov, F. Arisaka, and P. G. Leiman, Curr. Opin. Struct. Biol. **14**, 171 (2004).

[15] V. A. Kostyuchenko, P. G. Leiman, P. R. Chipman, S. Kanamaru, M. J. Van Raaij, F. Arisaka, V. V. Mesyanzhinov, and M. G. Rossmann, Nat. Struct. Biol. **10**, 688 (2003).

[16] V. A. Kostyuchenko, P. R. Chipman, P. G. Leiman, F. Arisaka, V. V. Mesyanzhinov, and M. G. Rossmann, Nat. Struct. Mol. Biol. **12**, 810 (2005).

[17] P. G. Leiman, P. R. Chipman, V. A. Kostyuchenko, V. V. Mesyanzhinov, and M. G. Rossmann, Cell **118**, 419 (2004).

[18] A. A. Aksyuk, P. G. Leiman, L. P. Kurochkina, M. M. Shneider, V. A. Kostyuchenko, V. V. Mesyanzhinov, and M. G. Rossmann, EMBO J. **28**, 821 (2009).
[19] P. Prehm, B. Jann, K. Jann, G. Schmidt, and S. Stirm, J. Mol. Biol. **101**, 277 (1976).
[20] B. Hu, W. Margolin, I.J. Molineux, and J. Liu. Proc. Natl. Acad. Sci., (2015), **112** (35).
[21] M. L. Yap, T. Klose, F. Arisaka, J. A. Speir, D. Veesler, A. Fokine, and M. G. Rossmann, Proc. Natl. Acad. Sci. **113**, 2654 (2016).
[22] K. A. Kaphingst, S. Persky, and C. Lachance, **14**, 384 (2010).
[23] B. Hu, W. Margolin, I. J. Molineux, and J. Liu, Proc. Natl. Acad. Sci. **112**, E4919 (2015).
[24] N. M. I. Taylor, N. S. Prokhorov, R. C. Guerrero-Ferreira, M. M. Shneider, C. Browning, K. N. Goldie, H. Stahlberg, and P. G. Leiman, Nature **533**, 346 (2016).
[25] F. Arisaka, J. Engel, and H. Klump. Prog. Clin. Biol. Res. **64**, 365 (1981).
[26] M. F. Moody, J. Mol. Biol. **25**, 201 (1967).
[27] M. F. Moody, Virology **26**, 567 (1965).
[28] M. F. Moody, J. Mol. Biol. **80**, 613 (1973).
[29] D. L. Caspar, Biophys. J. **32**, 103 (1980).
[30] R. C. Guerrero-Ferreira, M. Hupfeld, S. Nazarov, N. M. Taylor, M. M. Shneider, J. M. Obbineni, M. J. Loessner, T. Ishikawa, J. Klumpp, and P. G. Leiman, EMBO J. **38**, e99455 (2019).
[31] W. Falk and R. D. James, Phys. Rev. E - Stat. Nonlinear, Soft Matter Phys. **73**, (2006).
[32] M. Karplus and J. A. McCammon, Nat. Struct. Biol. **9**, 646 (2002).
[33] N. M. Taylor, N. S. Prokhorov, R. C. Guerrero-Ferreira, M. M. Shneider, C. Browning, K. N. Goldie, H. Stahlberg, and P. G. Leiman (2016), Nature, **533**.7603.
[34] I. Klapper. J. Comput. Phys. (1996), **125**(2).
[35] S. Goyal, N. C. Perkins, and C. L. Lee, J. Comput. Phys., **209**, 371 (2005).
[36] I. Tobias, D. Swigon, and B. D. Coleman, **61**, 747 (2000).
[37] A. D. Hirsh, T. D. Lillian, T. A. Lionberger, M. Taranova, I. Andricioaei, and N. C. Perkins, J. Comput. Nonlinear Dyn., **8**, (2013).
[38] A. Maghsoodi, A. Chatterjee, I. Andricioaei, and N. C. Perkins, J. Comput. Nonlinear Dyn. **11**, 041026 (2016).
[39] C. Gatti-Bono, and N.C. Perkins, JSV, **255**, 555 (2002).
[40] J. E. Shigley, *Shigley's Mechanical Engineering Design* (McGraw-Hill, New York, 2011).
[41] J. Howard, *Mechanics of Motor Proteins and the Cytoskeleton* (Sinauer

Associates, Sunderland, MA., 2001).
[42] A. Maghsoodi, A. Chatterjee, I. Andricioaei, and N. C. Perkins, Biophys. J. **113**, 195 (2017).
[43] J. C. Phillips, R. Braun, W. Wang, J. Gumbart, E. Tajkhorshid, E. Villa, C. Chipot, R. D. Skeel, L. Kalé, and K. Schulten, J. Comput. Chem. **26**, 1781 (2005).
[44] B. R. Brooks, R. E. Bruccoleri, B. D. Olafson, D. J. States, S. Swaminathan, and M. Karplus, J. Comput. Chem. **4**, 187 (1983).
[45] Rossmann, M. G., and V. B. Rao. *Viral Molecular Machines* (Springer Science & Business Media, Berlin, Germany., 2011).
[46] A. Fokine, Z. Zhang, S. Kanamaru, V. D. Bowman, A. A. Aksyuk, F. Arisaka, V. B. Rao, and M. G. Rossmann, J. Mol. Biol. **425**, 1731 (2013).
[47] Y. Tsuda, H. Yasutake, A. Ishijima, and T. Yanagida, Proc. Natl. Acad. Sci. U. S. A. **93**, 12937 (1996).
[48] F. Gittes, B. Mickey, J. Nettleton, and J. Howard, J. Cell Biol. **120**, 923 (1993).
[49] L. Letellier, P. Boulanger, M. De Frutos, and P. Jacquot, Res. Microbiol. **154**, 283 (2003).
[50] T. J. Silhavy, D. Kahne, and S. Walker, Cold Spring Harbor perspectives in biology (2010), **2**(5).
[51] J. D. Faraldo-Gómez and M. S. P. Sansom, Nat. Rev. Mol. Cell Biol. **4**, 105 (2003).
[52] V. Vadillo-rodriguez and J. R. Dutcher, Soft Matter **5**, 5012 (2009).
[53] V. Vadillo-rodriguez, S. R. Schooling, and J. R. Dutcher, **191**, 5518 (2009).
[54] E. F. Pettersen, T. D. Goddard, C. C. Huang, G. S. Couch, D. M. Greenblatt, E. C. Meng, and T. E. Ferrin, J. Comput. Chem. **25**, 1605 (2004).
[55] J. Kyte and R. F. Doolittle, J. Mol. Biol. **157**, 105 (1982).
[56] M. P. Goertz, J. E. Houston, and X. Zhu, 5491 (2007).
[57] Z. Pawlak, W. Urbaniak, and A. Oloyede, **271**, 1745 (2011).
[58] M. G. Poirier and J. F. Marko, Phys. Rev. Lett. **88**, 228103 (2002).
[59] A. Maghsoodi and N. Perkins, Sci. Rep. **8**, 1 (2018).
[60] M. G. Poirier, A. Nemani, P. Gupta, S. Eroglu, and J. F. Marko, 1 (2001).
[61] K. Soda, J. Phys. Soc. Japan **35**, 866 (1973).
[62] S. R. Aragón S and R. Pecora, Macromolecules **18**, 1868 (1985).
[63] C. P. Broedersz and F. C. Mackintosh, Rev. Mod. Phys. **86**, 995 (2014).
[64] L. Harnau, R. G. Winkler, and P. Reineker, J. Chem. Phys. **6355**, (1996).
[65] C. P. Brangwynne, G. H. Koenderink, E. Barry, Z. Dogic, F. C. MacKintosh, and D. A. Weitz, Biophys. J. **93**, 346 (2007).
[66] M. E. Janson and M. Dogterom, Biophys. J. **87**, 2723 (2004).
[67] K. M. Taute, F. Pampaloni, E. Frey, and E. L. Florin, Phys. Rev. Lett. **100**, 1 (2008).

[68] K. F. Graff, *Wave Motion in Elastic Solids* (Courier Corporation, 2012).
[69] J. Brugués, V. Nuzzo, E. Mazur, and D. J. Needleman, Cell **149**, 554 (2012).
[70] S. Burlacu, P. a Janmey, and J. Borejdo, Am. J. Physiol. **262**, C569 (1992).
[71] A. S. J. Swamidas, X. Yang, and R. Seshadri, J. Eng. Mech. **130**, 1297 (2004).
[72] A. Kis, S. Kasas, B. Babić, A. J. Kulik, W. Benoît, G. A. D. Briggs, C. Schönenberger, S. Catsicas, and L. Forró, Phys. Rev. Lett. **89**, 248101 (2002).
[73] F. Pampaloni, G. Lattanzi, A. Jonás, T. Surrey, E. Frey, and E.-L. Florin, Proc. Natl. Acad. Sci. U. S. A. **103**, 10248 (2006).
[74] M. Poirier, S. Eroglu, D. Chatenay, and J. F. Marko, Mol. Biol. Cell **11**, 269 (2000).
[75] M. G. Poirier, A. Nemani, P. Gupta, S. Eroglu, and J. F. Marko, Phys. Rev. Lett. **86**, 360 (2001).
[76] K. F. Graff, *Wave motion in elastic solids*. (Courier Corporation, 2012).
[77] A. Eswar, N., Webb, B., Marti-Renom, M.A., Madhusudhan, M.S., Eramian, D., Shen, M.Y., Pieper, U. and Sali, Curr. Protoc. Bioinforma. **15**, 5 (2006).
[78] M. N. Nguyen and M. S. Madhusudhan, **39**, (2011).
[79] J. T. Mika, A. J. Thompson, M. R. Dent, N. J. Brooks, J. Michiels, J. Hofkens, and M. K. Kuimova, Biophysj **111**, 1528 (2016).
[80] B. Gumí-audenis, L. Costa, F. Carlá, F. Comin, F. Sanz, and M. I. Giannotti, membrane, **6**(4), (2016).
[81] C. Browning, M. M. Shneider, V. D. Bowman, D. Schwarzer, and P. G. Leiman, Structure **20**, 326 (2012).
[82] M. Basler, Philos. Trans. R. Soc. B Biol. Sci. **370**, (2015).
[83] M. Basler, M. Pilhofer, G. P. Henderson, G. J. Jensen, and J. J. Mekalanos, Nature **483**, 182 (2012).
[84] P. Ge, D. Scholl, P. G. Leiman, X. Yu, J. F. Miller, and Z. H. Zhou, **22**, 377 (2015).
[85] A. H. A. Parret and R. De Mot, Trends Microbiol. **10**, 107 (2002).
[86] E. Krissinel and K. Henrick, J. Mol. Biol. **372**, 774 (2007).
[87] W. Jiang, M. G. Rossmann, A. Fokine, Z. Chen, D. Hanein, V. B. Rao, L. Sun, V. Padilla-Sanchez, and Z. Zhang, Proc. Natl. Acad. Sci. **114**, E8184 (2017).